COMPTON SCATTERING WITH GAMMA-RAYS AND SYNCHROTRON RADIATION

by

David A. Cardwell

A thesis submitted for the degree of
Doctor of Philosophy of the University of Warwick

Department of Physics
University of Warwick

March 1987

ABSTRACT

Directional Compton profile measurements of aluminium and chromium have been performed with 60 keV and 412 keV γ-radiation to assess the complementarity of the ^{241}Am and ^{198}Au spectrometer systems in common use by experimentalists. Revision of the data reduction procedure has yielded symmetrical Compton profiles within experimental error for the first time. The effects of exchange and correlation on theoretical Compton profiles calculated within the local density approximation have been evaluated via the Lam-Platzman correction and applied to existing transition metal results. Novel experiments using circularly polarised synchrotron radiation to detect the magnetic Compton profiles of iron and nickel have been performed successfully.

PREFACE

Over the past decade Compton scattering has been used extensively to determine the distribution of electron momentum in solids. This is a result of the advent of high resolution solid state detectors and multi-channel analysers required to detect and record high energy spectra. Since the discovery of the Compton effect in 1923 the interim period saw very little activity in this field due to the limited detection systems then available and long time scales involved in the measurement of spectra with crystal spectrometers. Today the Compton scattering technique is acknowledged as a powerful test of the electron wavefunction and is successfully performed over a range of incident photon energies used in various spectrometer systems around the world.

Unlike the results of charge density measurements by X-ray diffraction which describe electrons in terms of their position in real space, Compton scattering measurements enable interpretation of electron behaviour in momentum space. These techniques are complementary rather than rival with the description of matter in either real or momentum space depending on the nature of the property in question.

This thesis is concerned primarily with conventional γ-ray measurements on single crystals of aluminium and chromium to assess both the confidence limits with which Compton profiles can be interpreted and the information about band structure that they contain. In addition the agreement between experiment and local density based band theories is investigated by application of the Lam-Platzman correction to existing calculations which describes the effect of exchange and correlation on the Compton profile. Novel measurements using synchrotron radiation to detect the magnetic profiles of iron and nickel are also reported and likely developments in Compton spectroscopy are outlined.

CONTENTS

CHAPTER 3. DATA REDUCTION AND ANALYSIS

CHAPTER 4. ALUMINIUM

CHAPTER 5. CHROMIUM

CHAPTER 6. EXCHANGE AND CORRELATION EFFECTS

CHAPTER 7. THE MAGNETIC COMPTON PROFILES OF IRON AND NICKEL

LIST OF FIGURES

LIST OF TABLES

MEMORANDUM

This dissertation has been submitted to the University of Warwick in support of my application for the admission to the degree of Doctor of Philosophy. It contains an account of my own independent research except where acknowledged in the text performed in the Department of Physics under the supervision of Dr. M. J. Cooper during the period from October 1983 to September 1986. Details of the research to which I have contributed appear in the following publications ;

(1) Compton Profile Anisotropy in Ni_3Ga, Phil. Mag. A 50, 703, 1984.

(2) Polarised X-Ray Study of the Spin-Dependent Compton Profile of Ferromagnetic Iron, Nucl. Inst. Meths. A 243, 608, 1986.

(3) Directional Compton Profile Measurements of Aluminium with 60 and 412 keV Radiation, Phil. Mag. B 54, 37, 1986.

(4) Gamma-Ray Source Line Broadening and Compton Line Profile Analysis, Nucl. Inst. Meths. A 245, 485, 1986.

(5) Spin Dependent Momentum Distribution Studied with Circularly Polarised Radiation, Phys. Rev. B 34, 5984, 1986.

ACKNOWLEDGEMENTS

I would particularly like to acknowledge the support and encouragement of my supervisor Dr. M. J. Cooper and colleague Dr. D. Laundy throughout this period of research. I am also indebted to the following people associated with the Department of Physics ;

Dr. R. S. Holt, Dr. S. O. Manninen, Dr. A. J. Rollason. Dr. J. B. Staunton, Prof. S. Wakoh, Mr. T. Naylor and Mrs. S. Beaufoy.

On a personal note I would like to express my gratitude to Mr. N. J. Bradley of the Midland Bank for his patience, my wife Sharon for her infinite tolerance and my parents Margaret and Bill without whose continual financial and unbounded moral support this work would not have been possible.

D. A. Cardwell, 1987

Units

The system of units adopted in this work and in general use in Compton Scattering research is that of "atomic units" where $|\hbar| = |m| = 1$ and $|e| = 137.036$ and have the following relation to SI units ;

1 a.u. momentum = 1.9929×10^{-24} kg m s^{-1}
1 a.u. energy = 4.3598×10^{-18} J
1 a.u. length = 5.2918×10^{-11} m

CHAPTER 1

PHOTON SCATTERING THEORY

1. Introduction

1.1. Interactions of Photons with Matter.

When radiation impinges on matter the photons interact with the electron distribution of the target material in a variety of ways. If the energy of the incident photons is less than the threshold for electron-positron pair production (i.e. $E_\gamma < 2m_0c^2$) then only elastic scattering, inelastic scattering and photoelectric absorption can occur. The effect of these interactions is to remove photons, and therefore energy, from the transmitted beam. For well-collimated monochromatic radiation of intensity I_0 incident on an absorber, the subsequent reduction in flux is described by ;

$$I_t = I_0 \exp(-\mu x) \tag{1.1}$$

where I_t is the transmitted photon intensity and x is the absorber thickness. μ is the linear absorption coefficient and is dependent on the total scattering cross-section (i.e. a measure of the combined probabilities that a photon will interact in some way with the scatterer).

The aim of this section is to describe these interactions and to characterise the coupling between target and probe by the incident photon energy and change in photon wavevector on scattering.

1.1.1. Elastic Scattering

Elastic scattering is the interaction between photons and electrons which results in deviation of photons from the incident beam without any transfer of energy to the

scattering electrons. Although the magnitude of the photon wavevector remains constant during this interaction, its direction is dependent on the scattering angle and the subsequent transfer of momentum is absorbed as a collective excitation of the scattering system. The intensity of an elastically scattered beam is described by the classical Thomson cross-section and in non-crystalline solids this interaction occurs at all scattering angles (see James, 1948), i.e.

$$\left(\frac{d\sigma}{d\Omega}\right)_{Th} = \left(\frac{e^2}{m_0c^2}\right)^2 (\epsilon_1.\epsilon_2)^2 \qquad (1.2)$$

which for unpolarised radiation becomes ;

$$= \frac{1}{2}\left(\frac{e^2}{m_0c^2}\right)^2 (1+\cos^2\theta) \qquad (1.3)$$

where $\left(\frac{d\sigma}{d\Omega}\right)_{Th}$ is the Thomson cross-section, $\left(\frac{e^2}{m_0c^2}\right)$ is taken to be the classical electron radius, r_0, θ is the scattering angle, m_0 is the electron rest mass and ϵ_1 and ϵ_2 are the polarisation vectors of the incident and scattered photons respectively.

For the case of bound electrons, which are distributed over a volume with diameter comparable to X-ray wavelengths, the amplitude of elastic scattering is a function of $\frac{\sin\theta/2}{\lambda}$. For long wavelengths and/or small scattering angles, therefore, photons scattered in the forward direction are in phase and all electrons contribute equally to the scattered intensity. For smaller wavelengths and/or higher scattering angles, however, the interference between scattering from different parts of the electron density is described by the atomic form factor, f(K), and the cross-section becomes :

$$\left(\frac{d\sigma}{d\Omega}\right) = \left(\frac{d\sigma}{d\Omega}\right)_{Th} |f(K)|^2 \qquad (1.4)$$

with

$$f(K) = \int \rho(r) \exp(-iK.r)\, d^3r \qquad (1.5)$$

where $\mathbf{K}$ is the change in photon wavevector on scattering, i.e. $|\mathbf{K}| = \frac{4\pi \sin\theta/2}{\lambda}$, and $\rho(\mathbf{r})$ is the charge density. The form factor is given by the inverse Fourier transform of $\rho(\mathbf{r})$ and its magnitude may be obtained from X-ray diffraction experiments (see Warren, 1969).

If the charge density is periodic (e.g. as in a single crystal) then the form factor is periodic, i.e. it only exists for values of $\mathbf{K} = \mathbf{G}$ — a reciprocal lattice vector, and Bragg reflection occurs in specific directions.

1.1.2. Inelastic Scattering

Inelastic scattering involves energy transfer from the probe to the target and is therefore necessarily incoherent in nature. This interaction is generally described by one of two mechanisms.

When the momentum transfer from photon to an individual electron is conserved the interaction is referred to as Compton scattering. For the case where the corresponding energy transfer greatly exceeds the binding energy of the scattering electron an impulse approximation is deemed to be valid and the electron is ejected into a plane wave state. The interaction then simply becomes a binary encounter between photon and electron with the cross-section for Compton scattering independent of other bound electronic states. Inelastic scattering, therefore, cannot take place if the energy transferred to a bound electron is less than its binding energy due to the absence of an unoccupied final state. Similarly, for the case of conduction electrons in metals, Compton scattering will be restricted if the momentum transfer is less than the Fermi momentum, $\hbar k_F$, of the free electron gas.

In contrast to elastic scattering, the inelastically scattered intensity from an atomic distribution is simply Z times that from a single electron in any direction since there is no constant phase relationship between incident and scattered waves and hence no interference effects between different scattering amplitudes.

When the energy transfer between photon and electron is of the order of the electron binding energy the momentum is absorbed by the whole crystal rather than an individual electron. This is the regime of Raman scattering in which the encounter results in a change in the state of the scattering atom with the matrix element describing the interaction depending on initial and final accessible atomic states. If a bound electron is excited from energy state W_m to state W_n, where W_n represents the lowest unoccupied level, the energy loss of a Raman scattered photon is described by ;

$$h(\nu_f - \nu_i) = W_n - W_m \tag{1.6}$$

where ν_i and ν_f are the incident and emitted photon frequencies respectively. Spectral lines resulting from Raman scattering, therefore, are characteristically sharp because both initial and final states are discrete and occur close to binding edges in observed spectra where this interaction dominates the photon-electron scattering process.

1.2. The Compton Effect

In 1923 Compton showed that for a photon colliding with a stationary electron conservation of momentum and energy in the direction of the incident wavevector leads to a discrete scattered photon energy for a given scattering angle. i.e. ;

$$\omega_2 = \frac{\omega_1 m_0 c^2}{m_0 c^2 + 2\omega_1 \sin^2 \frac{\theta}{2}} \tag{1.7}$$

or more familiarly in terms of photon wavelength,

$$\Delta\lambda = \lambda_2 - \lambda_1 = \frac{2h}{m_0 c} \sin^2\left(\frac{\theta}{2}\right) \tag{1.8}$$

where ω_1 and ω_2 are the incident and scattered photon energies respectively, c is the velocity of light and $\frac{h}{m_0 c}$ is the Compton wavelength, λ_c, which has the value 2.42×10^{-12} m.

Considering a beam of low energy photons (i.e. $\lambda_1 >> \lambda_c$) interacting with stationary electrons, equation 1.8 predicts a very small change in wavelength on scattering. i.e. ;

$$\lambda_2 = 2\lambda_c \sin^2\left(\frac{\theta}{2}\right) + \lambda_1 \approx \lambda_1$$

Consequently there will be little change in the photon wavevector such that $|\mathbf{k}_1| \sim |\mathbf{k}_2|$. Under this condition the momentum transfer is given by :

$$|\mathbf{K}| = |\mathbf{k}_1 - \mathbf{k}_2| \approx 2|\mathbf{k}_1| \sin\left(\frac{\theta}{2}\right) \qquad (1.2)$$

By varying the scattering angle from 0 to π radians, therefore, it is possible to scan a wide range of energy and momentum space with $|\mathbf{K}|$ varying from 0 to a maximum of $2|\mathbf{k}_1|$ (i.e. when $\theta = \pi$). Figure 1.1 shows an approximate classification of the main types of scattering process in terms of energy and momentum transfer [i.e. the region of $(\mathbf{K}, \omega)$ space being sampled by the probe] referred to characteristic energies, ω_{charac} (e.g. absorption edges), and wavelengths, λ_{charac} (interparticle spacing, screening length etc.), of the scattering system. The region of $(\mathbf{K}, \omega)$ space below $K\lambda_{charac} = 1$ describes interactions which involve very little or no energy transfer and is consequently the regime of elastic scattering or photoelectric absorption. Above $K\lambda_{charac} = 1$ the photon interaction is predominantly with one electron and is characterised by large energy and momentum transfers which is the regime of Compton and Raman scattering.

1.2.1. Compton Scattering within the Born Approximation

The theory of Compton scattering is usually developed within the weak coupling limit between photon and electron commonly referred to as the Born Approximation (see Gottfried, 1966).

If the scattering potential is sufficiently weak the electromagnetic field of the photon may be treated as a small perturbation on the electron in which case the Golden Rule may be used to calculate the transition probability between initial and final electron momentum states. This is the lowest order Born Approximation and its most significant consequence is that the inelastic scattering amplitude, or matrix element describing a given transition, depends only on the change in photon wavevector, $\mathbf{K}$, and energy transfer to

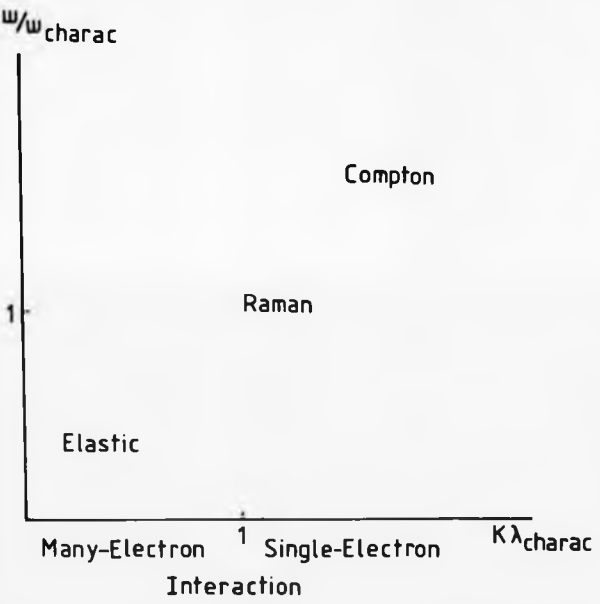

Figure 1.1 Classification of the type of scattering process according to the region of (K,ω) space being sampled referred to characteristic energies, ω_{charac}, and wavelengths, λ_{charac}, of the scattering system. The magnitude of the momentum and energy transfers are defined by the Compton shift equation.

the system, ω. Therefore the energy distribution of radiation scattered at a fixed angle θ into a solid angle $d\Omega$ with an energy bandwidth $d\omega$, i.e. the measured double differential scattering cross-section, can be written as a product of two terms, one of which characterises the nature of the interaction and the other describes the dynamics of the scattering system (i.e. the relative electron distribution), such that ;

$$\frac{d^2\sigma}{d\Omega d\omega} = \frac{\omega_2}{\omega_1}\left(\frac{d\sigma}{d\Omega}\right)_e S(K,\omega) \qquad (1.10)$$

where $\left(\frac{d\sigma}{d\Omega}\right)_e$ represents the coupling between probe and target and $S(K,\omega)$ is a generalised scattering factor. The factor $\frac{\omega_2}{\omega_1}$ reflects the energy dependence of the double differential scattering cross-section and is derived from the density of electron states.

1.2.2. Semi-Classical Treatment of Inelastic Scattering

The scattering factor is given by the Golden Rule as ;

$$S(K,\omega) = \sum_f \sum_i |\langle f|\sum_j \exp(i\,K.r_j)|i\rangle|^2\,\delta(E^f - E^i - \hbar\omega) \qquad (1.11)$$

This expression contains two physically different pieces of information. The matrix element (evaluated between initial and final electron states $\langle f|$ and $|i\rangle$) describes the scattering amplitude of the interaction and the delta function ensures conservation of energy during the scattering process. The factor $\sum_j \exp(iK.r_j)$, the Born operator, is simply the phase of the scattering amplitude from the j^{th} electron. Equation 1.10 now becomes the general scattering formula, 1.12, which describes the complete range of photon-electron scattering, i.e. ;

$$\frac{d^2\sigma}{d\Omega d\omega} = \frac{\omega_2}{\omega_1}\left(\frac{d\sigma}{d\Omega}\right)_e \sum_f \sum_i |\langle f|\sum_j \exp(iK.r_j)|i\rangle|^2\,\delta(E^f - E^i - \hbar\omega) \qquad (1.12)$$

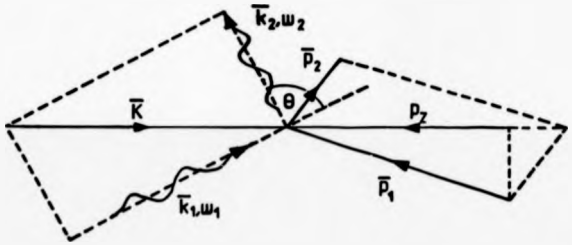

Figure 1.2 The kinematics of a photon (k_1, ω_1) interacting with a free electron (p_1, E_1). A Compton experiment yields information about the component of electron momentum, p_z, aligned with the scattering vector, K.

PAGINATION
ERROR

In order to determine the delta function in eq. 1.12 it is necessary to express the energy transfer on scattering in terms of the scattering vector and the initial electron momentum. It can be seen, again from figure 1.2, that in the single particle regime $\Delta\omega$ is given by ;

$$\Delta\omega = \frac{(\mathbf{p}_1 + \mathbf{K})^2}{2m_0} - \frac{|\mathbf{p}_1|^2}{2m_0}$$

$$= \frac{|\mathbf{K}|^2}{2m_0} + \frac{\mathbf{K}.\mathbf{p}_1}{m_0} \qquad (1.18)$$

The first term on the right-hand side describes the recoil of the electron. The second term is directly proportional to $\mathbf{K}.\mathbf{p}_1$ which represents the component of the electrons momentum parallel to the scattering vector (conventionally defined as p_z), and hence describes a Doppler shift in the energy of the scattered radiation. Since p_z is constant for a given electron, the number of initial electron states which correspond to an energy transfer $\Delta\omega$ is obtained by summation over all states in the p_x, p_y plane. Consequently within the IA and ensuring conservation of energy the general scattering formula may be written in terms of a two dimensional integral over p_x and p_y, i.e. ;

$$\frac{d^2\sigma}{d\Omega d\omega} = \left(\frac{d\sigma}{d\Omega}\right)_0 \left(\frac{\omega_2}{\omega_1}\right) \int_{p_x} \int_{p_y} n(\mathbf{p})\, \delta\left(\omega - \frac{|\mathbf{K}|^2}{2m_0} - \frac{\mathbf{K}.\mathbf{p}}{m_0}\right) dp_x\, dp_y \qquad (1.19)$$

This double integral, therefore, may be formally defined as the one-dimensional electron momentum distribution measured along the scattering vector, or the Compton profile, $J(p_z)$, i.e. ;

$$J(p_z) = \int_{p_x} \int_{p_y} n(p_x, p_y, p_z)\, dp_x dp_y \qquad (1.20)$$

where $n(p_x, p_y, p_z)$ represents the density of electrons per unit momentum having total momentum $\mathbf{p}$ ($= p_x + p_y + p_z$).

By inverting eq. 1.18 it can be seen that each energy point in the Compton cross-

section corresponds to scattering off an electron with momentum component, p_z, given by

$$p_z = \frac{(\omega_2 - \omega_1) + \omega_1\omega_2(1 - \cos\theta)}{(\omega_1^2 + \omega_2^2 - 2\omega_1\omega_2\cos\theta)^{1/2}} \qquad (1.21)$$

It should be possible, therefore, to relate the measured double differential cross-section to the Compton profile in the limit of large momentum transfers, i.e. ;

$$\frac{d^2\sigma}{d\Omega d\omega} = C(\omega_1, \omega_2, \theta)\, J(p_z) \qquad (1.22)$$

where C is a constant determined by ω_1, ω_2 and θ. The remainder of this section is concerned with the formulation of an expression within the IA describing the coupling between target and probe, $\left(\frac{d\sigma}{d\Omega}\right)_e$, from which C may be evaluated. If eq. 1.22 can be shown to hold, therefore, the Compton profile of the electron distribution can be extracted from the measured cross-section.

Platzman and Tzoar (1965) derived the semi-classical double differential cross-section for a free stationary electron from the matrix elements of the $|A|^2$ term in the Schrödinger equation (i.e. the non-relativistic limit). The Compton effect, however, is a relativistic phenomenon and consequently this formulation, which results in the Thomson cross-section, does not provide an adequate description of inelastic scattering.

To obtain the cross-section for relativistic final electron states it is necessary to quantise the photon field and to describe the electron energy, averaged over all electron spins, by the Dirac equation (see Klein and Nishina, 1929). This results in the well-known Klein-Nishina inelastic scattering cross-section. It is given by 1.23 and describes the relativistic scattering of photons by a free, stationary electron.

$$\left(\frac{d\sigma}{d\Omega}\right)_{KN} = \frac{1}{2} r_0^2 \left(\frac{\omega_2}{\omega_1}\right)^2 \left(\frac{\omega_1}{\omega_2} + \frac{\omega_2}{\omega_1} - \sin^2\theta\right) \qquad (1.23)$$

This particular formulation, however, is only applicable to unpolarised photons since it does not eliminate contributions to the cross-section from photons scattered into

polarisation states perpendicular to that of the incident radiation.

In the limit for low energy photons (i.e. $\omega_1 << m_0c^2$) $\omega_2 = \omega_1$ and eq. 1.23 necessarily reduces to the Thomson cross-section, i.e. the elastic scattering limit.

1.4. Inelastic Scattering Cross-Section for Moving Electrons

In order to formulate the inelastic scattering cross-section for high energy photons scattered from moving electrons it is necessary to extend the analysis of Klein and Nishina to include relativistic initial electron states.

Jauch and Rohrlich (1955) found the cross-section to be dependent on the initial electron momentum, p_1, rather than p_e implying that the momentum density cannot be extracted according to eq. 1.22. Equation 11.9 in Jauch and Rohrlich is the basic starting relationship and leads to ;

$$\frac{d^2\sigma}{d\Omega d\omega} = \frac{r_0^2 m_0^2 \omega_2 c^4}{2\omega_1 E_1 |K| + \frac{p_z}{E_z}\Delta\omega} \int dp_x\, dp_y\, n(p_1)\, X(p_1) \qquad (1.24)$$

$$\text{with} \quad X = \frac{p_1.k_1}{p_1.k_2} + \frac{p_1.k_2}{p_1.k_1} + 2m_0^2\left(\frac{1}{p_1.k_1} - \frac{1}{p_1.k_2}\right) + m_0^4\left(\frac{1}{p_1.k_1} - \frac{1}{p_1.k_2}\right)^2 \qquad (1.25)$$

where X is a flux factor dependent on p_1, which therefore cannot be removed from the integration, and E_1 is the initial electron energy [$= (p_1c + m_0^2c^4)^{1/2}$]. As with the Klein-Nishina cross-section, the above formalism does not observe the polarisation of either the initial or final state of the photon.

The problem of extracting $J(p_z)$ from eq. 1.24 was partially resolved by Eisenberger and Reed (1974) who assumed the initial electron motion to be only mildly relativistic, in which case E_1 may be removed from the integrand, and by Manninen, Paakkari and Kajantie (1974) who simplified the flux factor by assuming a scattering angle of 180°, i.e. close to that commonly used experimentally.

Ribberfors (1975 a, b) extended this analysis by integrating the relativistic cross-

section (eq. 1.24) by parts to yield a rapidly converging series of terms involving $J(p_z)$ and X', the flux factor modified to take account of the photon polarisation. Neglecting all but the first of these terms (i.e. those insignificant compared to $1/\omega_1^2$) leads to the zeroth order Ribberfors cross-section, i.e. ;

$$\frac{d^2\sigma}{d\Omega d\omega_2} = \frac{r_0^2 m_e^2 \omega_2 c^4}{2\omega_1 |K| E_1} X' J(p_z) \qquad (1.26)$$

where X' is defined by equations 30 - 33 in Ribberfors (1975a) and reduces to X in the back scattering limit.

Eq. 1.26 is completely general with respect to scattering angle and is accepted as the standard cross-section used by experimentalists. For cases where the electronic motion is highly relativistic, such as the rare-earth metals, higher order terms in Ribberfors series may be included in the cross-section although for most measurements the zeroth order approximation is completely adequate within the present limits of experimental accuracy.

Figure 1.3 shows the variation of $\frac{X(180^\circ)}{X'(\theta)}$ with momentum for three incident energies and 110° and 150° scattering geometries. In this figure $X(180^\circ)$ is the simplified flux factor, applicable only to 180° scattering, and $X'(\theta)$ is the generalised flux factor attributed to Ribberfors. The deviation of the curve from the p_z axis indicates the failure of the approximate cross-section to describe Compton spectra particularly at high values of momentum. Consequently for high incident energies and low scattering angles the 180° approximation is no longer valid and $J(p_z)$ should be extracted from experiment via the Ribberfors cross-section (eq. 1.26). Indeed, if the 180° approximation is used errors of up to 5% J(0) are inherent in the Compton profile at 10 a.u. which is significant compared to experimental accuracy [$\sim$ 0.5% J(0)]. Since the Ribberfors cross-section is used in the work reported here these errors do not reduce the accuracy of the processed data.

1.4.1. Spin Dependent Effects

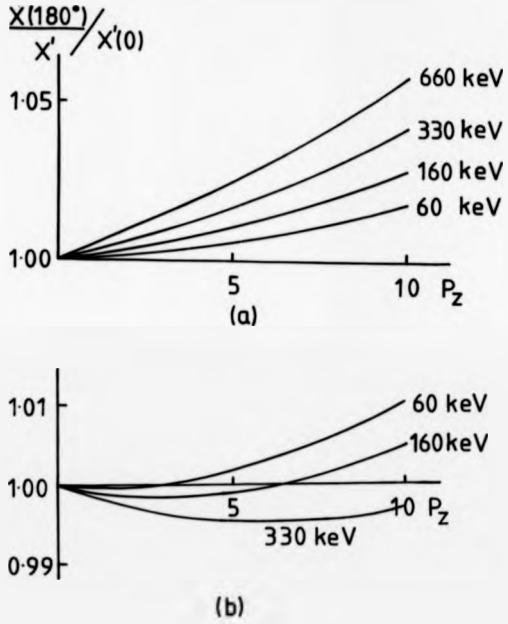

Figure 1.3 Variation of $\frac{X(180^\circ)}{X'(0)}$ relative to X'(0) with p_z for various incident photon energies for (a) 110° and (b) 150° scattering geometries. The magnitude of the ratio is equivalent to the error introduced to the Compton profile if $J(p_z)$ is extracted from measured data via the approximate cross-section of Manninen et al (1974) rather than that attributed to Ribberfors (1975).

To describe the effect of electron spin on the inelastic scattering cross-section the matrix operator A used to couple the photon to electron in the relativistic formulation was re-written by Platzman and Tzoar (1970) as a sum of spinless and spin dependent terms i.e. ;

$$M_{jk} = A_{jk} + iB.\sigma_{jk} \tag{1.27}$$

where σ_{jk} is the electron spin matrix (see Gasiorowicz, 1974) and B is given by the expression ;

$$B = -\frac{\hbar}{m_0c^2}\left\{e_2.e_0\,(k_1 \times k_2) - \frac{1}{2}\,(K.K)(e_2 \times e_0) - K \times (K \times e_2 \times e_0)\right\} \tag{1.28}$$

If the total electron spin is non-zero there is a contribution to the cross-section from the $iA(B.\sigma)$ and $B^2\sigma^2$ terms. Since the ratio of the magnetic to the electric dipole of an electron in an electromagnetic field is of the order $\sim \frac{\omega_1}{m_0c^2}$, however, then the B^2 term is small compared with the A^2 term for low incident energies and may be neglected in Compton experiments where $\omega_1 << m_0c^2$.

The cross or interference term in $|M|^2$ is imaginary and consequently vanishes for *real* photon polarizations. If, however, circularly polarized radiation is used as a probe i.e.

$$e_1 = \frac{\hat{u}_x + i\hat{u}_y}{\sqrt{2}} \tag{1.29}$$

where $\hat{u}_x$ and $\hat{u}_y$ are the components of the photon polarization in the plane perpendicular to k_1, then the product $e_1.e_0$ is complex and there is a contribution from the $A(B.\sigma)$ term to the total cross-section.

Assuming the Thomson differential scattering cross-section to describe the interaction of circularly polarised radiation with an electron and the matrix operator given by eq. 1.27, Platzman and Tzoar (1985) showed that the spin dependent double differential cross-section is given by ;

$$\frac{d^2\sigma}{d\omega d\Omega} = r_0^2 \int \left\{ |A|^2 [n_{p\uparrow} + n_{p\downarrow}] + 2 \left[\mathrm{Im}(A^* B_s) \right] [n_{p\uparrow} - n_{p\downarrow}] \right\} \times \delta\left(\omega - \frac{K^2}{2m_0} - \frac{K.p}{m_0}\right) \frac{d^3p}{(2\pi)^3} \qquad (1.30)$$

where $n_{p\uparrow}$ and $n_{p\downarrow}$ are the momentum densities of spin up and spin down electrons respectively and B_s is the projection of B along the scattering vector. By taking the difference between cross-sections for electrons of opposite spin (i.e. by replacing $n_{p\uparrow}$ with $n_{p\downarrow}$ and vice versa and subtracting) the cross-section becomes ;

$$\left(\frac{d^2\sigma}{d\omega d\Omega}\right)^{\lambda} = \left(\frac{d\sigma}{d\Omega}\right)^{\lambda}_{spin} \int (n_{p\uparrow} - n_{p\downarrow}) \times \delta\left(\omega - \frac{K^2}{2m_0} - \frac{K.p}{m_0}\right) \frac{d^3p}{(2\pi)^3} \qquad (1.31)$$

where $\left(\frac{d\sigma}{d\Omega}\right)^{\lambda}_{spin}$ describes the additional term arising from the interaction of circularly polarised photons with electrons of spin σ and is of the form (see Lipps and Tolhoek, 1954) ;

$$\left(\frac{d\sigma}{d\Omega}\right)^{\lambda}_{spin} = r_0^2 \left(\frac{\omega_1}{\omega_2}\right)^2 \left(\frac{1 - \cos\theta}{m_0 c}\right) \sigma.(k_1 \cos\theta + k_2) \qquad (1.32)$$

Since $\frac{k_1}{m_0 c} = \frac{\omega_1}{m_0 c^2}$ this term contributes $\sim f_m \frac{\omega_1}{m_0 c^2}$ to the total cross-section, where f_m is the fraction of unpaired spins, and will be most appreciable for high scattering angles (i.e. k_1 parallel to σ) and high incident energies (see Holt and Cooper, 1983). This is illustrated by figure 1.4 which shows (a) the ratio of the spin dependent cross-section (eq. 1.32), $d\sigma_s$, to the ordinary Klein-Nishina cross-section (eq. 1.23), $d\sigma_0$, and (b) the Klein-Nishina cross-section as a function of scattering angle for three incident photon energies. It can be seen that the spin dependent term in the cross-section only becomes significant compared to the Klein-Nishina cross-section at scattering angles $\sim 180^\circ$ and incident energies > 25 keV and consequently magnetic Compton scattering experiments are performed close to back scattering geometry with synchrotron radiation which facili-

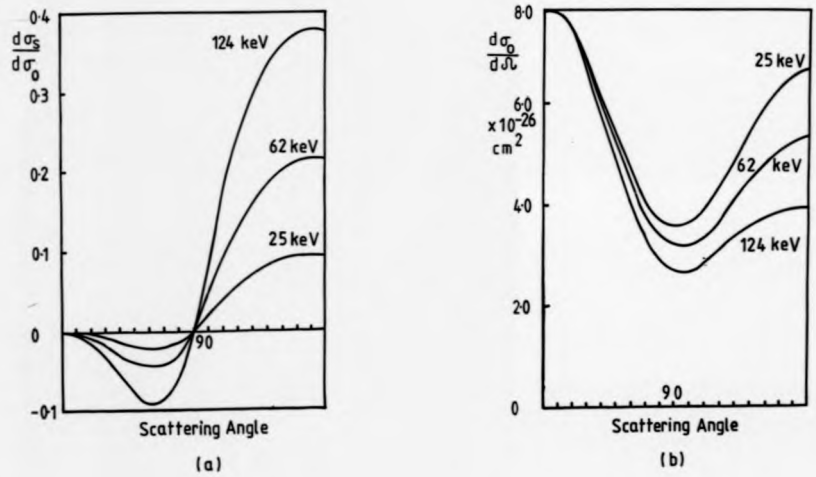

Figure 1.4 Comparison of (a) the ratio of the spin dependent cross-section, $d\sigma_s$, to the ordinary Klein-Nishina cross-section, $d\sigma_0$, and (b) the Klein-Nishina cross-section as a function of scattering angle at three incident photon energies.

tates optimisation of the incident photon energy and intensity.

1.5. Validity of the Impulse Approximation

The essential feature of the Impulse Approximation is that an electron bound to its parent atom may be regarded as a free electron but having the same momentum distribution as it would have in the target atom (see Williams, 1977). This approximation is only valid when the energy transfer greatly exceeds the electron binding energy so that the electron is ejected into a continuum. Since the time the photon spends probing the electronic distribution, $\sim \frac{\hbar}{\Delta\omega}$, is short for large momentum transfers, then the potential energy, $V(r)$, is effectively constant for the duration of the interaction and cancels out of the delta function in the general scattering formula for bound electron states. Consequently if the Impulse Approximation holds the encounter is binary and impulsive with the other electrons unable to relax before the photon and electron have escaped from the scattering system (i.e. take account of the hole created during the interaction).

Within the IA it is possible to formulate a relatively simple relationship between the second differential scattering cross-section and the Compton profile for free, stationary electrons as shown in section 1.3. For the case of bound electrons, however, where the energy transfer is of the order of the electron binding energy, this relationship becomes a complicated function of intermediate electron states and extraction of the Compton profile from the measured cross-section is impossible.

In the formulation of the cross-section so far only plane wave states of the scattered electron have been considered although clearly it is possible to chose more realistic final electron states such as orthogonal or augmented plane waves (OPW's or APW's). Additionally the electron may be assigned an initial energy incorporating the effects of binding and not merely $\frac{p^2}{2m_e}$. The effect of these changes has been calculated by various authors (see Eisenberger and Platzman, 1970 and Mendelsohn and Biggs, 1973) using exact hydrogenic (EH) final states to describe s-type orbital electron scattering. These calculations

indicate that the subsequent correction to the IA is proportional to $\frac{\text{binding energy}}{|\mathbf{K}|^2}$ and hence is negligible until the energy transfer becomes comparable to the electron binding energy. At this point the impulse hydrogenic (IH) result (i.e. that obtained for momentum transfers much greater than the 1s binding energies) exceeds the EH result and there is a slight shift in the position of the Compton peak. This observation is consistent with the results of more sophisticated theories (see Currat, DeCicco and Kaplow, 1971, Currat, DeCicco and Weiss, 1971, Mendelsohn, Bloch and Smith, 1973, Bloch and Mendelsohn, 1974 and Mendelsohn and Bloch, 1975) which have subsequently been developed to include electron correlation and exchange effects, a wider range of photon energies and higher hydrogenic electron shells (L and M).

Experimentally the validity of the Impulse Approximation has been investigated with low energy spectrometers ($\omega_1 < 60$ keV). Shifts in the position of the Compton peak relative to that predicted by eq. 1.7 of up to 20 eV have been discovered by Weiss (1975) and Weiss, Cooper and Holt (1977) using Mo $K_{\alpha_{1,2}}$ X-rays (17.8 keV) to study Al, Polyethylene and Li and by Barlas, Rueckner and Wellenstein (1977) using HEEIS (High Energy Electron Impact Spectroscopy) in a study of H_2, He and D_2. Manninen, Cooper and Cardwell (1986) used 60 keV γ-rays to measure the Compton profile of Al and graphite and observed an asymmetry around $p_z = 1$ a.u. but detected no shift in the Compton peak centre (see section 3.3.2.1)

In general the point at which the IA breaks down is well understood. It holds for loosely bound valence electrons but fails for the core if the energy transfer is not significantly greater than the binding energies of the scattering electrons. To ensure that $J(p_z)$ can be easily extracted from the measured cross-section, Compton scattering experiments usually involve high scattering angles and large momentum transfers in which case all electrons contribute to the total profile. Thus by appropriate choice of experimental conditions the breakdown of the Impulse Approximation does not pose a problem.

CHAPTER 2

ELECTRON DISTRIBUTIONS IN MOMENTUM SPACE

2.1. The Dirac Transformation

In real space the solutions of the Schrödinger equation yield the real space one-electron wavefunctions, $\phi_j(r)$, the square of which gives the probability distribution of the j^{th} electron. The charge density, $\rho(r)$, for a many electron system is then obtained by summing the one electron distributions over all electrons, i.e. ;

$$\rho(r) = \sum_j \phi_j^*(r)\,\phi_j(r) \tag{2.1}$$

Similarly if $\chi_j(p)$ are the momentum space wavefunctions then $\chi_j^*(p)\,\chi_j(p)$ is the one electron probability distribution in momentum space. Consequently the momentum distribution of many electrons, $a(p)$, is given by ;

$$a(p) = \sum_j \chi_j^*(p)\,\chi_j(p) \tag{2.2}$$

Perhaps the most obvious method, therefore, of obtaining the momentum space wavefunctions is to solve the Schrödinger equation in momentum space, i.e.

$$\left(\frac{p^2}{2m} - E\right)\chi_j(p) + V(p)\,\chi_j(p) = \epsilon_j\,\chi_j(p) \tag{2.3}$$

in exactly the same way that the $\phi_j(r)$ are obtained from the real space formulation. In practice, however, this method is not straight forward since $V(p)$ is obtained by Fourier transforming the Coulomb potential, $V(r)$. Consequently eq. 2.3 is an intractable integral equation and can only be solved for relatively simple electron distributions such as the one electron hydrogenic atom (see Fock, 1935) and the 2 electron He atom (M^{c}Weeny and

Coulson, 1949, and Henderson and Scherr, 1960) – more complicated electron densities require an alternative method.

Such an alternative is to solve the Schrödinger equation in real space and to Dirac-Fourier transform the resulting wavefunctions according to the following equation ;

$$\chi(\mathbf{p}) = \frac{1}{(2\pi)^{3N/2}} \sum_j \int \psi(\mathbf{r}_j) \exp\left(-i\,\mathbf{p}_j.\mathbf{r}_j\right) (d\mathbf{r}) \qquad (2.4)$$

then the momentum distribution is given by ;

$$n(\mathbf{p}) = \sum_j \left| \int \phi_j(\mathbf{r}) \exp(-i\mathbf{p}.\mathbf{r})\, d\mathbf{r} \right|^2 \qquad (2.5)$$

The transformation 2.4 is clearly only practicable if the total N-electron wavefunction in position space can be written as the antisymmetrical Slater determinant of the one-electron wavefunctions (i.e. the Hartree-Fock scheme). In this case the total electron momentum wavefunction, $\chi(\mathbf{p})$, is given by the determinantal product of the individually transformed electron orbitals and can readily be obtained for complex electron distributions provided the real space wavefunctions are known. Benesch and Smith (1973) developed a formulism along these lines to take account of electron-electron correlation effects, which are neglected in the Hartree-Fock approach (see section 6.1.1), and subsequently provided a method of constructing the momentum distribution from the most complicated position space wavefunctions.

Podolsky and Pauling (1929) formulated a general expression for the Dirac transformation of hydrogenic electron orbitals which when written as a product of radial and angular components do not change their form on transformation, i.e. ;

$$\phi_j(\mathbf{r}) = R_{nl}(\mathbf{r})\, Y_{lm}(\theta_r, \phi_r) \qquad (2.6)$$

transform to

$$\chi_j(\mathbf{p}) = P_{nl}(\mathbf{p})\, Y_{lm}(\theta_p, \phi_p) \qquad (2.7)$$

Hence the spherical harmonics in position space, $Y_{lm}(\theta_r, \phi_r)$, which determine the sym-

metry of the wavefunction, are independent of the transformation and may be removed from the integral in eq. 2.4. Consequently the only difference between the position and momentum representations arises from the transformation of the radial part of the wavefunction [i.e. $R_{nl}(r) - P_{nl}(p)$].

For simple Slater type orbitals (see Slater, 1930), analytic expressions for the momentum space wavefunctions and hence Compton profiles can be readily obtained, as illustrated by table 2.1, although in general calculation of the exact momentum distribution is much more difficult.

2.2. Profile Representations of Isotropic Distributions

The general description of $J(p_z)$ by eq. 1.20 in the preceding chapter defines the direction dependent Compton profile measured along the scattering vector and is applicable to all electron momentum distributions. In particular this equation may be used to exploit differences in directional profiles for crystalline scattering systems by orienting different symmetry directions (i.e. p_z) with the scattering vector. For isotropic distributions, however, such as gases, liquids or powders where the directional properties are lost, transformation of eq. 1.20 to cylindrical polar coordinates results in the isotropic Compton profile defined by ;

$$J(q) = 2\pi \int_{q}^{\infty} p\, n(p)\, dp \qquad (2.8)$$

where $n(p)$ is the scalar momentum distribution and $J(q)$ is used to denote an isotropic Compton profile. Since this equation is only applicable to spherically symmetric momentum densities it is convenient to define a radial momentum distribution, $I(p)$, in an analogous way to the radial charge density used in X-ray diffraction studies. i.e.

$$I(p) = 4\pi p^2 n(p) \qquad (2.9)$$

in which case the isotropic Compton profile becomes ;

$$J(q) = \frac{1}{2} \int_{q}^{\infty} \frac{I(p)}{p}\, dp \qquad (2.10)$$

orbital	γ_n	$\psi(r)$	$\chi(p)$	$J(q)$
1s	2.70	$\left(\frac{\gamma_1^3}{\pi}\right)^{1/2} \exp - \gamma_1 r$	$\left(\frac{8\gamma_1^5}{\pi^2}\right)^{1/2} \frac{1}{(\gamma_1^2 + p^2)^2}$	$\frac{\gamma_1^5}{2\pi} \frac{1}{(\gamma_1^2 + q^2)^2}$
2s	0.65	$\left(\frac{\gamma_2^5}{3\pi}\right)^{1/2} \exp - \gamma_2 r$	$\left(\frac{8\gamma_2^5}{3\pi^2}\right)^{1/2} \frac{3\gamma_2^2 - p^2}{(\gamma_2^2 + p^2)^3}$	$\frac{8\gamma_2^5}{9\pi} \frac{(8q^4 - 20\gamma_2^2q^2 + 23\gamma_2^4)}{8(\gamma_2^2 + q^2)^4}$
2p	0.65	$\left(\frac{\gamma_2^5}{3\pi}\right)^{1/2} r \cos\theta \exp - \gamma_2 r$	$-i\left(\frac{2\gamma_2^5}{\pi^2}\right)^{1/2} \frac{8\gamma_2 p}{(\gamma_2^2 + p^2)^3} \cos\theta$	$\frac{32\gamma_2^7}{15\pi} \frac{\gamma_2^2 + 5q^2}{(\gamma_2^2 + q^2)^4}$

Table 2.1 Momentum space wavefunctions, $\chi(p)$, and Compton profiles, $J(q)$, derived from the 1s, 2s and 2p Slater-type orbitals, $\psi(r)$, of Li (see Podolsky and Pauling, 1929). These orbitals, which take no account of electron correlation and band structure effects, are of a simple, no-nodal form and consequently enable the above momentum space expressions to be formulated analytically according to equations 2.10 and 2.4. The parameter γ_n is related to the inverse of the principle quantum number and therefore reflects the spatial extent of the wavefunction and the angle θ defines the orientation of the momentum vector relative to the p_z axis (i.e. $p_z = p\cos\theta$).

I(p), therefore, may be extracted from a measurement by inverting eq. 2.10 ;

$$I(p) = -2q\left(\frac{d}{dq}J(q)\right)_{q=p} \qquad (2.11)$$

By evaluating the principle momentum expectation values of the radial distribution function, $\langle p^n \rangle$, where

$$\langle p^n \rangle = \int_0^\infty p^n\, I(p)\, dp \quad , \qquad (2.12)$$

or equivalently, $$\langle q^n \rangle = 2(n-1)\int_0^\infty q^n\, J(q)\, dq \qquad (2.13)$$

it is possible to extract electron density properties of physical interest from the Compton profile (see Epstein, 1973). Assuming the correct asymptotic behaviour of n(p) at large p (see Williams, 1977; chapter 5), so that the integral in eq. 2.12 does not diverge, the most commonly encountered moments have the following meanings ;

$\langle p^{-1} \rangle = 2J(0)$, the peak value of the Compton profile.

$\langle p^0 \rangle = Z$, the number of electrons per atom.

$\langle p^1 \rangle =$ the mean electron momentum.

$\langle p^2 \rangle = 2 \times$ the total kinetic energy.

Higher order moments are unbounded and therefore cannot be obtained from J(q).

Perhaps the most important of these moments is the total kinetic energy since it gives a measure of the quality of the Compton profile via the virial theorem which, for Coulomb interactions, equates the average kinetic energy per bound electron to the total energy with a change of sign. In addition the second moment also provides a means for determining molecular binding energies (see Holt and Cooper, 1980). In practice, however, little significance can be placed on this quantity when derived from experiment due to the statistical inaccuracy of measured profiles at high momenta which is amplified when calculating $\langle p^2 \rangle$.

2.3. Reciprocal Relationships

The complementarity between real space and momentum space wavefunctions described in the previous section may be extended to describe other functions of physical interest in momentum density studies. In an analogous way to which charge densities are obtained by Fourier transforming the measured form factors in X-ray diffraction experiments, it is possible to define a reciprocal form factor, B(r), as the Fourier transform of the three dimensional momentum distribution in a similar way to which f(K) is defined in eq. 1.5, i.e.

$$B(r) = \int n(p) \exp(-i\, p.r)\, dp \qquad (2.14)$$

The B-function, therefore, is a real space representation of the Compton profile and may be interpreted in a complementary fashion to the atomic form factor by writing f(K) and B(r) as the autocorrelation of the momentum and position space wavefunctions respectively i.e. ;

$$f(K) = \int \chi^{*}(p)\, \chi(p + k)\, dp \qquad (2.15)$$

$$B(r) = \int \psi^{*}(r')\, \psi(r' + r)\, dr' \qquad (2.16)$$

where both functions are subject to the normalisation rule f(0) = B(0) = Z, the atomic number of the scatterer.

Since Compton scattering experiments yield only one dimensional distributions, however, it is convenient to evaluate the B-function along one direction. In this case B(z) can be written as the Fourier transform of the Compton profile and may consequently be obtained experimentally (see Pattison, Weyrich and Williams, 1977) i.e. ;

$$B(z) = \int\int\int n(p_x, p_y, p_z) \exp(-i\, p_z z)\, dp_x\, dp_y\, dp_z \qquad (2.17)$$

$$= \int J(p_z) \exp(-i\, p_z z)\, dp_z \qquad (2.18)$$

Inspection of the overlap integrals 2.15 and 2.16 reveals that for high and intermediate values of K the main contribution to f(K) comes from the high velocity core electrons

rather than the valence electrons which have comparatively small momenta. Conversely in real space the dominant contribution to $B(r)$ comes from the free, spatially extended valence electrons with the localised core electrons only contributing to the overlap integral at small spatial displacements. This reflects the sensitivity of diffraction studies to core electron states and momentum density studies to valence electron states.

Figure 2.1 illustrates the family of functions interrelated by Fourier transformation and autocorrelation from which the position/momentum space symmetry is readily apparent. It should be noted, however, that although a knowledge of the real and position space wavefunctions enable charge and momentum densities to be determined, the converse is not true since all the information about the phase of the wavefunction is lost when the product $\psi^*(r)\,\psi(r)$ (or $\chi^*(p)\,\chi(p)$) is formed. Consequently it is not possible to determine charge densities from momentum densities and vice versa which preserves the independence of X-ray diffraction and Compton spectroscopy.

2.4. Free Atoms

The formulation of the Compton profile in the preceding section was based on the assumption that the electrons in a given scatterer may be regarded as independent, in which case the momentum distribution can readily be obtained from the momentum space transforms of the individual electron wavefunctions.

As an illustration of the momentum distribution obtained from a basis set of independent wavefunctions, figure 2.2 shows the free atom Compton profile of chromium ($1s^2 2s^2 2p^6 3s^2 3p^6 4s^1 3d^5$) calculated numerically in the non-relativistic Hartree-Fock approximation (see Biggs, Mendelsohn and Mann, 1975). The contribution to the total profile of each individual shell normalised to the appropriate number of electrons is clearly shown and is a direct consequence of the separation of $\rho(r)$ into single electron wavefunctions. More generally it can be seen from this figure that the free atom profile consists of two distinct contributions - the core electrons possess a flat, extended profile whereas the valence electrons contribute a sharper, more local, feature to the total profile. On transi-

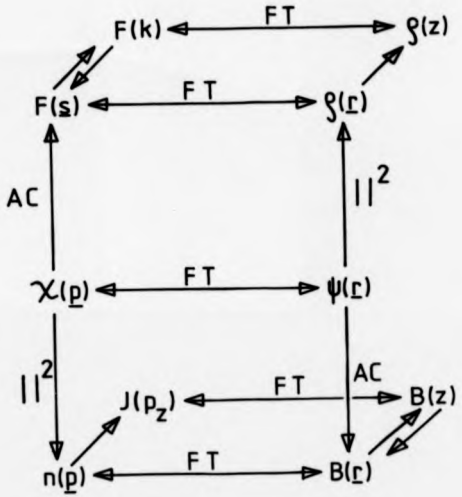

Figure 2.1 The family of functions in position and momentum space interrelated by the Dirac-Fourier transformation. From the one-electron wavefunctions it is possible to derive the above properties by autocorrelation (AC) and squaring the modulus ($|\psi|^2$) as indicated. Since these operations are irreversible, however, it is not possible to relate charge density measurements to those obtained from Compton scattering studies.

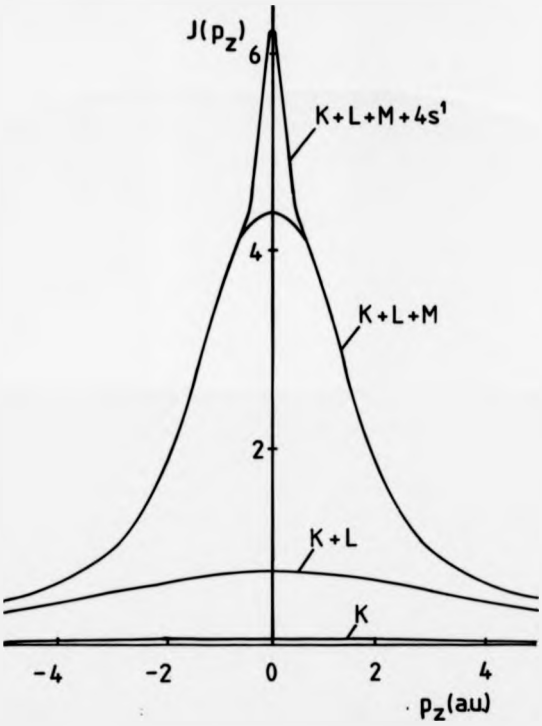

Figure 2.2 The free atom Compton profile of chromium ($1s^2 2s^1 2p^6 3s^2 3p^6 4s^1 3d^5$) calculated numerically within the non-relativistic Hartree-Fock approximation (see Biggs et al, 1975). The valence electron contribution to the total profile is localised around the origin whereas the core electrons possess a flatter more extended Compton profile.

tion of the atom to a solid or molecule it may be expected that the core contribution will remain largely unaffected whilst the valence electron profile will be significantly changed since these electrons determine the nature of the chemical bond (see Holt, 1978).

In practice the independent electron model is not generally valid since the effects of electron correlation and exchange and Coulomb screening significantly perturb the wavefunction in all but the most simplest of distributions (i.e. the inert gases). Compton profile measurements of helium (see Eisenberger and Platzman, 1970) and neon (see Eisenberger, Henneker and Cade, 1972) using $Mo_{K_{\alpha,\beta}}$ X-radiation (17.6 keV) and of N_2, Ar and Kr with ^{123}Te γ-rays (see Eisenberger and Reed, 1972) are in good agreement with the one-electron Hartree-Fock wavefunctions of Clementi (1965). This indicates that correlation effects in noble gas profiles are too small to be detected within the experimental error of existing measurements. Consequently the free atom Hartree-Fock profiles are considered to provide an adequate description of monatomic and simple diatomic gas momentum densities and are used to represent core electron distributions in metals where the effects of electron correlation are small. For electron distributions where these effects are significant, however, such as conduction electrons in metals, the independent particle model is only a first approximation to the momentum density and has to be appropriately modified.

2.5. Solids

2.5.1. Simple Metals

The simplest picture of a metal assumes that the valence electrons form a non-interacting, homogeneous gas which occupy a set of states in momentum space confined to the Fermi sphere. The momentum distribution of the tightly bound core electrons is unaffected by the formation of the solid and is well represented by a Hartree-Fock free ion in which case the composite momentum density is given by a superposition of valence and core electron distributions. In this regime there is a continuum of states above the Fermi energy, ϵ_F, and consequently the electron gas is highly polarisable and susceptible to the

effects of correlation although in the first instance these will be ignored.

At absolute zero all states within the Fermi sphere of the free electron gas are occupied, in which case n(p) is constant below the Fermi momentum, p_f, and is zero elsewhere as illustrated by the dashed line in figure 2.3 (a). From eq. 2.8 the Compton profile is then given by ;

$$J(p_z) = \begin{cases} \pi\, n(0)\,(p_f^2 - p_z^2) & \text{if } p_z \leq p_f \\ 0 & \text{if } p_z > p_f \end{cases} \qquad (2.19)$$

where $n(0) = \dfrac{n}{4/3\ \pi p_f^3}$, the number of conduction electrons per unit volume momentum space, $p_f = (3\pi^2\rho)^{1/3}$ and ρ is the charge density. For $p_z \leq p_f$ (i.e. $n(0) = 1$), therefore, the Compton profile reduces to a distinctive inverted parabola ;

$$J(p_z) = \frac{3\pi\,(p_f^2 - p_z^2)}{4p_f^3} \qquad (2.20)$$

This lineshape is illustrated in figure 2.3 (b) and is most representative of systems characterised by a low conduction electron density such as the light alkali metals Li, Be and Na and the light metals Al and Mg (see Phillips and Weiss, 1968 and Cooper, Pattison, Williams and Pandey, 1974).

A major feature of the free electron model is the discontinuity in the Compton profile at the Fermi momentum which is apparent from the comparison between the free electron profile of aluminium and the corresponding Hartree-Fock band structure calculation of Causa, Dovesi, Pisani and Roetti (1981) shown in figure 2.4. It can be seen from this figure, however, that the free electron parabola overestimates the contribution to the profile below p_f which is consistent with measurements made on the alkali metals and therefore indicates that correlation and band structure effects have to be considered for a more realistic formulation.

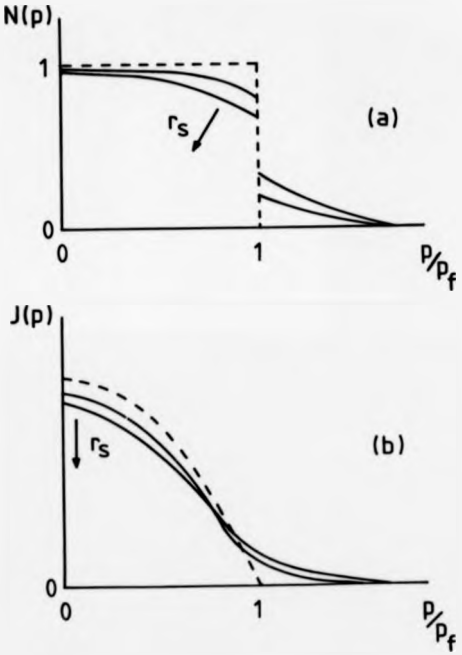

Figure 2.3 The effect of electron-electron correlation on (a) the momentum density and (b) the Compton profile in a homogeneous electron gas. The deviation from the free electron limit (dashed curves) is determined by the Wigner radius of the distribution, r_s, which is related to the inverse of the electron density, $\frac{1}{\rho}$.

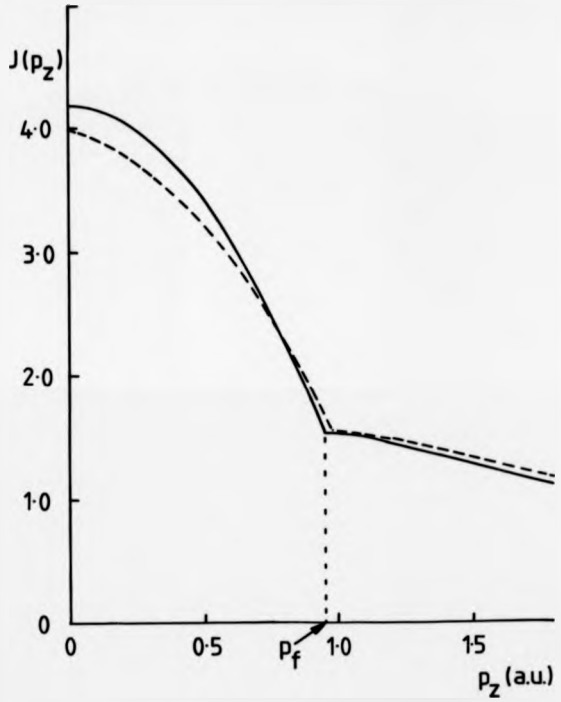

Figure 2.4 Comparison of the free electron Compton profile (+ free ion core) of aluminium —— with the Hartree-Fock band calculation of Causa et al, 1981 - - - - . The discontinuity at the Fermi momentum, p_f, is characteristic of the free electron model and becomes less obvious when the effects of electron correlation are introduced.

2.5.2. Electron-Electron Correlation Effects

Since Coulomb interactions between electrons decrease the total energy of the electronic system, the effect of correlation is, via the virial theorem, to promote electrons from low lying states in the momentum distribution to states above the Fermi surface as illustrated by the solid curves in figure 2.3 (see Daniel and Vosko, 1960). This observation is consistent with that made by considering the reciprocal relationship between $\phi(\mathbf{r})$ and $\chi(\mathbf{p})$ - the Coulomb interaction effectively reduces the spatial extent of each electron which results in a more localised wavefunction hence occupation of higher momentum states.

The degree of correlation present in a given distribution is uniquely determined by the charge density, ρ, which is assumed constant in the homogeneous electron gas model. As a consequence of screening, the extent to which the electrons are correlated is directly proportional to the effective volume per electron, $\frac{1}{\rho}$, and is measured in terms of the Wigner radius, r_s, which characterises a given distribution according to the following equation ;

$$r_s = \left(\frac{3}{4\pi\rho}\right)^{1/3} \tag{2.21}$$

Thus for spatially symmetric electron distributions r_s reflects the extent to which the momentum density deviates from the free electron limit although this shift is difficult to measure due to limitations in experimental resolution (see chapter 3).

2.5.3. Band Structure Effects

In real metals the valence electrons are regarded as nearly free since they are confined only by the periodic potential of the lattice to lie within the boundaries of the solid (see Seitz, 1935). Band theories, therefore, represent the valence electron wavefunction, $\psi_k(\mathbf{r})$, as a series expansion of Bloch functions, $U_k(\mathbf{r})$. This preserves their plane wave description but introduces high frequency Fourier coefficients, $a_G(\mathbf{k})$, to $\psi_k(\mathbf{r})$ as a

consequence of the periodicity of the lattice (see Bloch, 1928), i.e.

$$\psi_k(r) = U_k(r) \exp(ik.r) \tag{2.22}$$

where

$$U_k(r) = \sum_G a_G(k) \exp(iG_N.r) \tag{2.23}$$

The effect of band structure on the momentum distribution can be appreciated by considering the Fourier transformation of the Bloch-type orbitals, i.e.

$$\chi_k(p) = \int U_k(r) \exp(ik.r) \exp(-ip.r)\, dr \tag{2.24}$$

$$= \sum_G a_G(k)\, \delta(p - k - G) \tag{2.25}$$

Consequently the contribution to the momentum space wavefunction from an electron in state k in a particular occupied band is given by the sum over all reciprocal lattice vectors of the Fourier coefficients, $a_G(k)$, which effectively raise electrons to states of higher momentum $p = k + G$. The band momentum density, therefore, is obtained by squaring eq. 2.25 and summing over all occupied states in the band, ν, i.e.

$$n^{band}(p) = \sum_k n_\nu(k) \sum_G |a_G(k)|^2\, \delta(p - k - G) \tag{2.26}$$

where $n_\nu(k)$ is the occupancy of the k^{th} state in the ν^{th} band. Since $|a_G(k)|^2$ may be interpreted as the probability of an electron in state k contributing to the density at $p = k + G$ for a particular band, then the total momentum distribution is subsequently given by a sum over all occupied bands. In this regime, therefore, the electron distribution may be represented by an array of spheres in k space each centred at a particular reciprocal lattice point, G_N, rather than a single sphere as is the case for free electrons. This is illustrated by figure 2.5 which shows the free electron spheres repeated throughout a 2 dimensional reciprocal lattice, each weighted according to the probability of finding an electron in a high order momentum state, $|a_G(k)|^2$. The Compton profile is then obtained by integrating over the plane intersecting these regions which subsequently exhibits a series

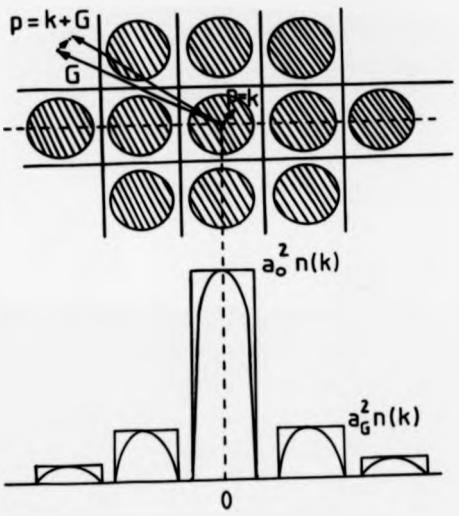

Figure 2.5 The Seitz model for Nearly Free Electrons in a square lattice. The effect of band structure is to promote electrons from a state **k** to a state **k** + **G** and consequently shift momentum density from low to higher p_x. The weight of each contribution is given by the square of the Fourier coefficients, $a_G(\mathbf{k})$, which diminish rapidly with increasing momentum.

of maxima and minima moving out from the origin due to lattice effects as shown in the bottom half of the figure.

In summary, Bloch wave representation of the wavefunction as an alternative to plane waves introduces high order components to the momentum density which broaden $J(p_z)$ in a similar way to the effects of electron-electron correlation. Furthermore, since calculation of the Compton profile involves integrating over a specific set of spheres in the plane perpendicular to p_z, then in general there is a difference between pairs of directional profiles. It is particularly informative, therefore, to interpret metallic Compton profiles in terms of this anisotropy i.e. ;

$$\Delta J(p_z)^{\text{aniso}} = J_{hkl}(p_z) - J_{h'k'l'}(p_z) \qquad (2.27)$$

where hkl denote the plane perpendicular to the scattering vector.

The absolute effect of band structure on the Compton profile has been calculated by Cooper, M. J., Williams, Borland and Cooper, J. A., (1970) for the case of lithium and generally shifts between 10% and 15% of the valence electrons to momentum states above the Fermi surface.

The agreement between the electron gas model and experiment may be further improved by orthogonalisation of the conduction electron wavefunction to that of the core. This is illustrated by figure 2.6 which shows (a) the orthogonalised 3s wavefunction of sodium compared with a simple plane wave representation and (b) the effect of orthogonalisation on the Compton profile. It can be seen that the OPW calculation is in much better agreement with experiment than an interacting electron gas model which is indicated by the dashed curve in (b) (see Eisenberger, Lam, Platzman and Schmidt, 1972 and Pandey and Lam, 1973).

2.6. B-functions of Simple Metals

To interpret the momentum density in real space the B-function representation of eq. 2.16 has to be modified to include a sum over the k states in each occupied band

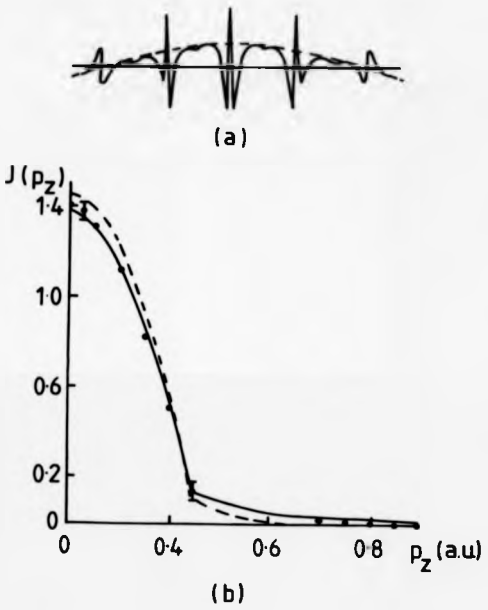

Figure 2.6 (a) The wavefunction for an electron in the 3s band of metallic sodium compared with a simple plane wave representation - - - - and (b) the effect of orthogonalisation of the plane wave to the core on the Compton profile of sodium. Compared to experiment · · · · · (see Eisenberger et al, 1972) the OPW calculation (see Pandey and Lam, 1973) is a significant improvement on the interacting electron gas model - - - - with a lattice perturbation potential.

introduced by the application of Bloch's theorem i.e. ;

$$B(r) = \sum_{k} n_k(k) \int \phi_k^*(r + r') \phi_k(r') \, dr' \qquad (2.28)$$

Expanding eq. 2.28 in terms of one electron Bloch functions and evaluating $B(r)$ for any real lattice transition vector, $r = R_L$, this expression reduces to a Brillouin zone integral (see Schülke, 1977,78) ;

$$B(R_L) = \frac{2}{V_{BZ}} \int_{BZ} n_k(k) \exp -ik.R_L \, dk \qquad (2.29)$$

where V_{BZ} is the Brillouin zone boundary. This equation is equivalent to the Lock-Crisp-West theorem (see Lock, Crisp and West, 1973) which expresses $B(R_L)$ as the Fourier transform of the k-space occupation number, $n(k)$. For insulators, where all the bands are filled, therefore, $n(k)$ is constant and $B(R_L)$ is zero for all R_L. Consequently the reciprocal form factor of an insulator should cross the real space axis at all points equivalent to lattice translations, $r = R_L$.

For metals, however, where the bands are only partially filled, $n(k)$ is not in general constant in which case the values of $B(r)$ at R_L form a Fourier series expansion of $n(k)$ and simply define the Fermi surface. In positron annihilation studies the Fermi surface of an electron distribution can be reconstructed quite accurately from the B-function (see West, 1980) although in Compton scattering studies the retrievable information is somewhat more limited. This is due to the poorer momentum resolution of the measured Compton profile which transforms to a rapidly decaying, multiplicative function in real space and severely restricts the number of $B(R_L)$ that can be resolved from the noise level, particularly at high r.

To illustrate the information contained within the reciprocal form factor, figure 2.7 shows a comparison between the experimental and theoretical B-functions along (a) the c axis of the insulator selenium (see Kramer, Krusius, Schröder and Schülke, 1977) and (b) the <110> direction of nickel (see Rollason, Schneider, Laundy, Holt and Cooper, 1987).

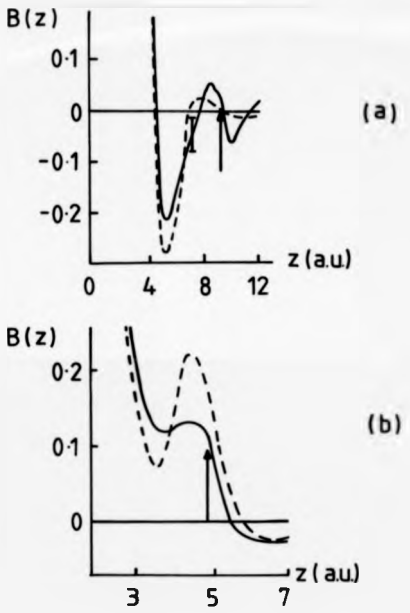

Figure 2.7 Experimental —— and theoretical - - - - (see Krusius, 1977) B-functions along (a) the c axis of the insulator selenium (see Kramer et al. 1977) and (b) the <110> direction of nickel (see Rollason et al. 1987). The arrows indicate the respective lattice constants of selenium and nickel which correspond to (a) the position of the Bloch zeros and (b) the three dimensional Fourier transform of the Fermi surface which is non-zero due to the partially filled conduction band in the metal.

In (a) the theoretical B-function is calculated from a basis set of OPW's (see Krusius, 1977) and is equal to zero at $B(R_L)$, as indicated by the arrow, which is in good agreement with experiment and is characteristic of an insulator. In (b), however, the value of $B(R_L)$ is non-zero for both theoretical (see Wang and Callaway, 1975) and experimental reciprocal form factors which indicates the presence of partially filled bands - i.e. characteristic of a metal. It should be noted that the zeros at other values of r in (a) less than those indicated represent information about the particular form of the Bloch wavefunctions.

In addition to information about the Fermi surface, the behaviour of the B-function between lattice displacements provides an indication of the type of bonding between various elements in the atomic chain. For example, a large negative area between the lattice zeros generally implies an interatomic region of anti-bonding whereas a large positive area implies a region dominated by bonding atomic orbitals (see Pattison and Weyrich, 1979, for a study of LiH).

2.7. Band Theories

The starting point for modern day band theories is to assume the one-electron model with the supposition that all other crystal effects neglected by this approximation can be represented by a non-zero effective potential energy, V(r). Consequently V(r) is very much "tailored to fit" for a given electron distribution and may vary for different electron energies.

In this regime the one-electron Schrödinger equation can be solved for individual wavefunctions which are then used to describe the effects of overlap in energy between electron states from different atoms. Band theories differ from one another essentially only in the way the effects of electron-electron correlation and exchange (i.e. the spin interaction) are represented, if at all.

The Seitz model presented in the last section was one of the earliest band theories to be applied with any success to simple metals and currently many different methods are available (see Blakemore, 1974). This model, however, takes no account of exchange and

correlation effects which were first introduced by Slater who suitably modified the Hartree-Fock equations by including an exchange term, i.e. ;

$$\left(-\frac{1}{2}\nabla^2 - \frac{Z}{r} + V_c + V_x\right)\Phi_i = \epsilon_i \Phi_i \qquad (2.30)$$

where Φ_i is the determinantal wavefunction, V_c is the Coulomb field due to the electronic charge distribution and V_x is the exchange potential which describes the interaction of electrons of like spin (see section 6.1.1.1).

To account for electron-electron correlation, which is not contained in eqns. 2.30, it is necessary to consider an interacting electron gas whose local charge density is equal to the actual charge density at a given r, i.e. the local density approximation (LDA) - see chapter 6. In this case the effective electron exchange and correlation can be represented by replacing V_x by V_{xc} where

$$V_x - V_{xc} = \alpha 2\left(\frac{3\rho(r)}{\pi}\right)^{1/3} \qquad (2.31)$$

or equivalently in terms of the Wigner radius ;

$$V_{xc} = \alpha\left(\frac{18}{\pi^2}\right)^{1/3}\frac{1}{r_s} \qquad (2.32)$$

The exchange coefficient, α, varies between band calculations but generally lies in the range $2/3 \leq \alpha \leq 1$.

Slater's formulation of the exchange and correlation term was the first application of density functional theory to the solution of the many electron problem (see Schlüter and Sham, 1982). Indeed perhaps one of the most successful modern day band theories is that based on the LDA which calculates electronic properties by solving the single particle Kohn-Sham equations (see Kohn and Sham, 1965). It has been shown by Lam and Platzman (1974), however, that calculation of the Compton profile by this method requires the addition of a correction term to $J(p_z)$ in order to fully include the effects of exchange and

correlation. The formal derivation of this correction term is deferred until chapter 6 where it is shown to take the following form ;

$$\Delta J^{LDA}_{\rho(r)}(q) = \int_{\text{unit cell}} \rho(r) \left[J^{h}_{\rho(r)}(q) - J^{f}_{\rho(r)}(q) \right] d^3r \qquad (2.33)$$

where $J^{h}_{\rho(r)}(q)$ is the Compton profile of the homogeneous interacting gas with the (local) electronic charge density $\rho(r)$, normalised to one electron and $J^{f}_{\rho(r)}(q)$ is the same quantity for the homogeneous free electron gas. The magnitude of this correction, which has been neglected in all recent density functional calculations, is small but significant compared with experimental error and its full extent on available transition metal calculations is presented in chapter 6. This is done in the hope of resolving the difference between experiment and theory which has been a considerable cause of concern over the past decade in Compton spectroscopy.

CHAPTER 3

DATA REDUCTION AND ANALYSIS

3.1. Introduction

Over the past decade a significant improvement in both the statistical quality and reliability of Compton data has been observed. Accordingly measured data require careful processing if the maximum amount of information is to be extracted from experimental momentum density studies. In general, before measured data can be interpreted, a series of energy dependent corrections have to be applied. Individually the effect of these corrections on the final lineshape is quantitatively small [typically ~ 1% J(0)]. Their application, however, facilitates resolution of small differences between directional Compton profiles (e.g. ~ 0.2% J(0) for aluminium and ~ 1.0% J(0) for chromium - see chapters 4 and 5 respectively) and hence provides a basis for identifying the limitations of available band calculations. Without accurate reduction on this scale Compton data provide little more than a qualitative description of electron momentum and the usefulness of the technique is diminished.

3.2. Outline of Processing

The extraction of the Compton profile from experimental data is based on the Ribberfors cross-section (see Ribberfors, 1975a) given by eq. 1.26 which relates $J(p_z)$ to the double differential scattering cross-section and can be written in terms of the scattered photon energy, ω, i.e.

$$D(\omega) = C(\omega)\, J(p_z) \qquad (3.1)$$

where $D(\omega)$ is the double differential cross-section and $C(\omega)$ is the Ribberfors cross-section.

The explicit dependence of momentum on ω is given by eq. 1.21. The first step in the data reduction is to relate the measured spectrum, $M(\omega)$, to $D(\omega)$. This requires the removal of energy dependent effects such as detector efficiency, background and spectrometer response, which are determined largely by characteristics of the source, and for beam absorption, geometrical broadening and multiple scattering which depend on the incident photon energy and sample characteristics. These corrections to the measured spectrum are either additive, multiplicative or convolutive and should be performed sequentially in the reverse order to which they occur experimentally (i.e. detector corrections are performed first and source corrections are performed afterwards). This strategy ensures that the distribution of intensity is reproduced at all stages of the experiment (from detector to source) and that errors introduced by asequential deconvolution are reduced. The following equation describes measured Compton data qualitatively in terms of these corrections which are defined in figure 3.1 ;

$$M(\omega) = R(\omega) * \eta(\omega)\, G(\omega) * S(\omega) * A(\omega)\, D(\omega) + B(\omega) \qquad (3.2)$$

where * represents a convolution.

The Compton profile is then effectively extracted from the measured data by a rearrangement of this equation ;

$$J(p_z) = N\, C^{-1}(\omega)\, A^{-1}(\omega)\, S^{-1}(\omega) * G^{-1}(\omega) * \eta^{-1}(\omega) \left[R^{-1}(\omega) * \left(M(\omega) - B(\omega) \right) \right] \qquad (3.3)$$

where N is a normalisation constant characterised by the sample. This simple, but approximate, deconvolution scheme is interpreted as a series of operations performed in the order illustrated schematically in figure 3.1.

The transformation from energy to momentum space is performed before the correction for multiple scattering is applied and the final profile is necessarily normalised to the number of electrons per atom. Consequently the multiple scattering correction is of the following form ;

$$J(p_z)^{single} = \alpha J(p_z)^{total} - J(p_z)^{mult.} \qquad (3.4)$$

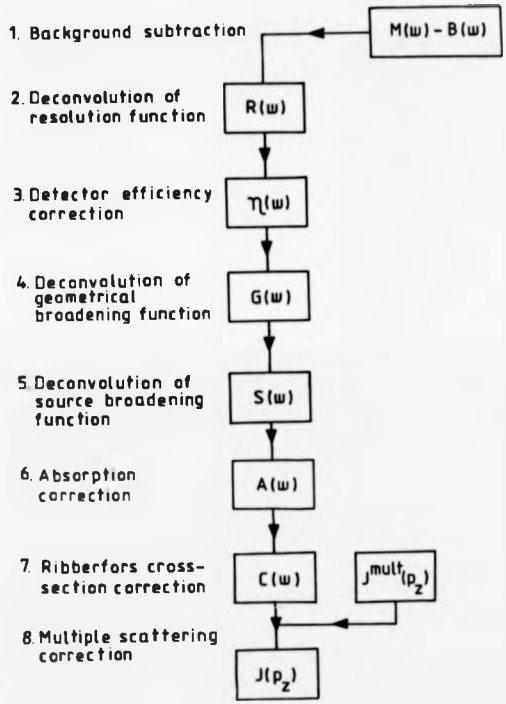

Figure 3.1 Flow chart of the data reduction procedure.

where α is the normalisation constant required to include a percentage of multiple scattering in the measured single profile (i.e. to preserve the area of the Compton profile). Since the distribution of multiply scattered photons to a first approximation is independent of sample orientation, α is determined effectively by the target geometry. When only the profile anisotropies between samples of identical dimensions are required the multiple scattering correction takes the form of a simple rescaling by the constant α in which case an accurate determination of $J(p_z)^{mult}$ is not essential. When a comparison between experiment and theory is to be made, however, the multiple profile has to be calculated by a Monte Carlo simulation and is typically a broad, asymmetrical lineshape. In general the correction for multiple scattering accounts for $\sim$ 5% to 25% of the Compton profile depending on the sample density and geometry.

Table 3.1 describes the source of each correction made in the data reduction procedure. Fortunately the preliminary system measurements (detector efficiency and resolution and source broadening) are properties of the spectrometer and only need to be repeated periodically to assess the effects of degradation of the germanium detector crystal. In practice, however, it is not always possible to measure these properties due to the difficulty in simulating the exact spectrometer conditions in an independent experiment. In this case calculations are made in support of experimental data. Subsidiary calculations such as geometrical broadening, multiple scattering and normalisation are determined by the sample and have to be performed for each measurement. Spectrum calibration, exposure timings and background calibration are derived directly from experiment.

The computational ease with which Compton data may be reduced depends on the order in which the energy dependent corrections are applied. The errors associated with asequential processing, however, must be insignificant compared with the level of experimental accuracy obtainable (currently $\sim$ 0.5% and $\sim$ 1% J(0) for the gold and americium systems respectively). As measurements become more accurate, therefore, the reduction of data for a given system has to be reviewed and it is to this end that the processing order described in figure 3.1 has been adopted for data obtained from the high energy system.

	SUBJECT	RESULT
PRELIMINARY SYSTEM MEASUREMENTS	(1) Te source spectrum	(1) Detector resolution fn., $R(\omega)$
	(2) Ba source spectrum	(2) Detector efficiency fn., $\eta(\omega)$
SUBSIDIARY CALCULATIONS	(1) Apparatus collimation	(1) Geometrical broadening, $G(\omega)$
	(2) Sample density	(2) Absorption, $A(\omega)$
	(3) γ-ray source geometry	(3) Source broadening fn., $S(\omega)$
	(4) Free atom profile	(4) Normalisation, N
	(5) Sample geometry	(5) Multiple profile, $J^{mult}(p_z)$
EXPERIMENTAL DATA MEASUREMENTS	(1) Sample spectrum	(1) Data, $M(\omega)$
	(2) Background spectrum	(2) Noise, $B(\omega)$
	(3) Exposure timings	(3) Signal : Noise correction ratio

Table 3.1 Classification of the reduction procedures and the sources of corrections for Compton data measured on the gold spectrometer.

On the other hand, a simpler but more approximate reduction suffices for measurements on the ^{241}Am spectrometer.

The following sections describe the effect of the energy dependent corrections on measurements made on the 60 keV ^{241}Am and 412 keV ^{198}Au spectrometer systems employed in the present studies which are described in chapter 4.

3.3. System Calibrations

3.3.1. Detector Efficiency Function

For a finite thickness of germanium there is a finite probability that a photon entering the detector will pass straight through the crystal without losing any of its energy. This probability, which sharply increases with increasing photon energy, is $1 - e^{-\mu t}$, where μ is the energy dependent linear attenuation coefficient and t is the thickness of the detector crystal. It defines $\eta(\omega)$, the efficiency of the detector, by :

$$\eta(\omega) = \frac{\text{Number of photons absorbed}}{\text{Number of photons entering detector}} \qquad (3.5)$$

The detector efficiency at a given energy is determined experimentally by comparison of observed γ-ray intensities with the known relative intensities of the emission lines (see Lederer, Hollander and Perlman, 1967). In practice this is not straight forward due to the lack of suitable γ-ray sources with sufficient decay lines in the region of the Compton peak (~ 140 - 180 keV for the high energy system). As a result of this scarcity of points a model dependent fitting to the limited experimental data is essential. Figure 3.2 shows a comparison between $\eta(\omega)$ measured using the isotope ^{126}Ba which contains seven prominent decay lines below 400 keV (Timms, 1986, Private communication) and a Monte Carlo simulation of the detector efficiency (Laundy, 1986, private communication). It can be seen from this figure that the simulation is in excellent agreement with experiment which vindicates the use of the calculation to correct Compton data obtained on the 412 keV spectrometer. This is preferable to using an analytic fit to the measured efficiency

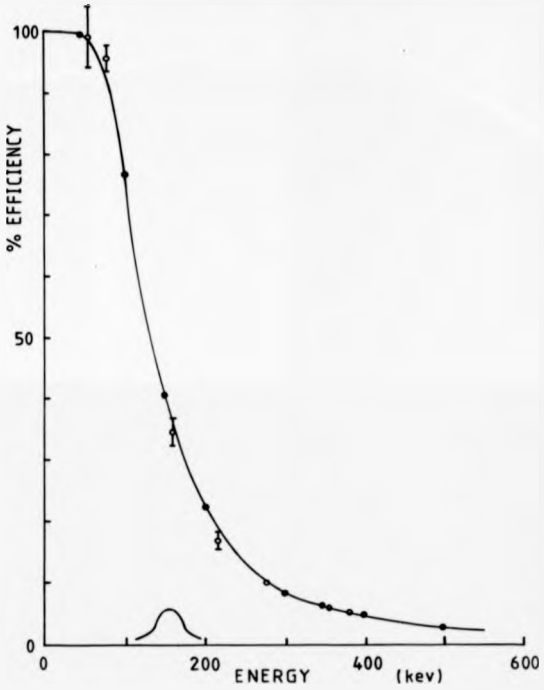

Figure 3.2 Detector efficiency predicted by a Monte Carlo simulation (solid line) compared with experimental results based upon the emission lines of ^{139}Ba (○ ○ ○). The position of the superimposed Compton peak corresponds approximately to that obtained from the high energy system.

since only one decay line occurs in the region of the Compton peak and subsequent interpolation introduces errors which may be significant due to the relatively large variation of $\eta(\omega)$ between $\sim$ 100 and 200 keV (see figure 3.2).

Measurements made on the ^{241}Am system do not need correcting for detector efficiency since they occur at energies below 70 keV up to which point the detector is 100% efficient to within a small fraction of a percent.

3.3.2. Detector Response Function

The response of the detector to a unique incident photon energy depends on the properties of the detector crystal (band gap, perfection, size, etc.) and must therefore be measured in an independent experiment. Ideally this would be done using a point source to eliminate line broadening due to inelastic scattering within the source capsule (i.e. source broadening) and with the same geometrical collimation as employed in the actual experiment. In practice, however, appropriate γ-ray sources have to be of finite size in order for the detector to record sufficient intensity (gold sources typically have a cross-sectional area of $\sim$ 15 mm^2) and consequently there is a degree of source broadening inherent in all response function measurements.

In essence the effect of source broadening is to generate a polychromatic source, i.e. an array of delta functions each of which produces a secondary Compton profile displaced from the incident photon energy according to eq. 1.7 when scattered through an angle θ. The spread in incident photon energy due to scattering within the source, therefore, results in an asymmetrical smearing of the measured Compton profile by an amount determined by the degree of overlap between the secondary Compton profiles. Because the energy transfer associated with the high energy system is relatively large compared with that of the low energy system (253 keV c.f. 11 keV respectively), subsequent measurements are subject to a lower contamination by source broadening effects since a larger proportion of the secondary profiles occur outside the region of the Compton peak. The effects of source broadening, therefore, are generally more serious for low energy measure-

ments although they can be minimised by chosing a thin source of small surface area.

The response of the detector to a delta function input is a characteristic, effectively Gaussian, photopeak at the incident photon energy, ω_i, with a low energy tail caused by the escape of photons and electrons from active areas of the crystal. The width of the peak is determined essentially by the efficiency of charge collection by the detector crystal and is given by ;

$$\Delta E_{FWHM} = (a + 5.546F\Delta\omega_i)^{\frac{1}{2}} \qquad (3.6)$$

Here a represents electronic noise and is constant, F is the Fano factor ($\sim$ 0.1 for good Ge detectors) and Δ is the energy gap of the detector crystal (0.74 eV for germanium and 1.16 eV for silicon).

The combination of source broadening and detector crystal effects makes the resolution of the spectrometer one of the most problematical corrections to deal with satisfactorily. The extent of the two contributions to the low energy tail, however, may be investigated by adjusting the source and detector collimation and by recording spectra from sources of varying strength, geometry and encapsulation. A primary objective of the data processing is to remove the effect of the composite response function tail from the measured data and to ultimately produce symmetrical Compton profiles.

3.3.2.1. The 60 keV Spectrometer Response Function

In order to accurately determine the resolution function for the ^{241}Am system it is desirable to expose the detector to a γ-ray source with an appropriate decay line at the Compton peak (48.36 keV for 171° scattering). Due to the unavailability of such a source, however, it is in common practice to determine the detector resolution function for this system at the incident photon energy (59.54 keV) ; this over-estimates the FWHM of the response by roughly 11%, an amount which is estimated to correspond to the effect of beam divergence (i.e. scattering through angles $\theta \pm \Delta\theta$ where $\Delta\theta$ is defined by the apparatus collimation). If the americium source were composed entirely of the pure metal the mean free path for inelastic scattering would be very short ($\sim$ 0.17 mm) and such a

source would generate a high spectral contamination. Since the source consists of AmO_2 in a ceramic matrix, however, its exact composition is not known and mathematical simulation of source broadening is very difficult. Currently no account of this is taken in the subsequent data processing of spectra measured on this system. The following investigation of the low energy tail of the detector response function measured at 60 keV was made to establish whether or not the approximate resolution function used in the processing of data from the low energy system is adequate or requires modification.

Experimentally the area of the resolution function tail measured at the lower photon energy increases from ~ 1% of the peak area for pin-hole collimation of the detector (~ 1mm diameter) to ~ 40% when the full surface area of the crystal is irradiated (~ 80 mm^2). In view of this sensitivity, therefore, it is desirable to measure the resolution function with similar collimation geometry to that used in the actual experiment. Traditionally this function has been measured by placing an uncollimated source a few centimetres in front of the detector. This method, however, overestimates the tail contribution to the response due to both source broadening and detector crystal effects and introduces inaccuracies to the data processing.

Figure 3.3 shows the low energy tail measured with pin hole collimation of the 60 keV response function produced by (A) a 100 mCi ^{241}Am line source in a stainless steel container with a 250 μm steel wall, (B) a thin ~ 0.3 μCi mm^{-2} foil source of active depth ~ 1 μm embedded below a 2 μm Au/Pd alloy sheet and (C) the 100 mCi source with an erbium filter placed in front of the detector pinhole. The intensity scale on this figure is expressed as a ratio to the height of the photopeak which is located at 59.54 keV. The thickness of the source used to produce tail (B) is much less than the mean free path of 60 keV radiation in the active source material and therefore little scattering occurs within it. This is reflected by the low intensity of the tail compared with measurement (A) in which the source thickness was much greater than the mean free path and therefore more representative of the actual spectrometer source. The presence of the erbium K absorption edge at 57.5 keV in tail (C) establishes that the low energy tail is due almost entirely

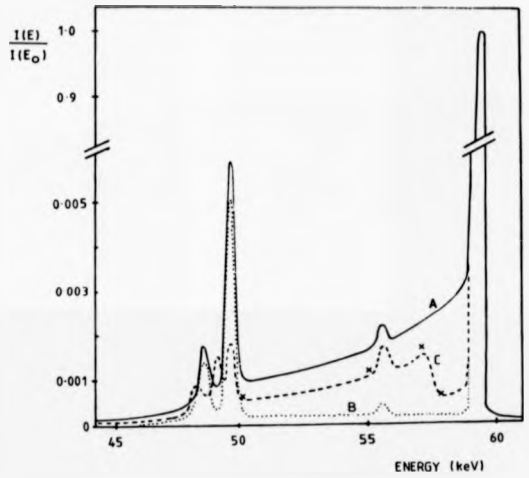

Figure 3.3 The effect of source encapsulation on the low energy tail for 60 keV radiation. The above spectra are recorded from (A) a 100 mCi ^{241}Am line source, (B) a thin ~ 0.3 μCi mm $^{-2}$ ^{241}Am foil source and (C) the source used in measurement (A) with an erbium filter between source and detector. The points × correspond to the tail of curve (A) after applying a correction for absorption in the Er filter. All measurements were made with a pinhole collimator (diameter 1 mm) in front of the detector and the vertical scale is the intensity normalised by the 59.54 keV elastic peak height.

to scattering within the source. If the tail were a detector response effect then the filter would have merely attenuated the intensity distribution uniformly. The difference between tail (C) and the points denoted by ×, which are calculated from the erbium absorption coefficients at the appropriate energy, describes the contribution to the tail from the detector and varies from ~ 18% at 58 keV to ~ 8% at 50 keV. Consequently when processing data measured on the low energy system the effect of the tail on the profile symmetry must be carefully assessed.

Figure 3.4(a) shows the portion of the tail attributed to scattering within the source (tail A) obtained by subtracting the symmetric part of the elastic line, reflected about its peak, from curve (A) in figure 3.3. It should be noted that this tail, which has an area of ~ 3.8% compared with the photopeak area, is independent of detector effects, such as the germanium escape peaks, which have been removed.

In the Compton scattering process each incident energy in the polychromatic tail scatters through an angle defined by the spectrometer (171° in this case) according to eq. 1.7, assuming the scattering electron to be stationary and the effects of beam divergence small. As a result the displaced tail consists of a superposition of Compton profiles and is distributed over a narrower energy region as illustrated by tail B figure 3.4(a). The transformed intensity at each energy point, dE, has been calculated by the Klein-Nishina scattering cross-section (eq. 1.23). To compare the asymmetry introduced in the Compton profile by this tail it is necessary to measure the profile of a thin foil sample in order to minimise sample effects such as absorption and multiple scattering. Figure 3.4 (b) shows such a measurement for graphite (see Manninen, Cooper and Cardwell, 1986). To allow for the finite momentum of the scattering electrons tail B in figure 3.4(a), transformed to momentum space via eq. 1.21, has to be convoluted with the free atom Compton profile and its area normalised to the experimental profile produced by 59.54 keV γ-rays. The resultant asymmetry, curve A, is compared with experiment in figure 3.4 (b). Since the presence of the tail offsets the Compton peak centre a further correction to the asymmetry is necessary before the applicability of this prediction can be assessed. This

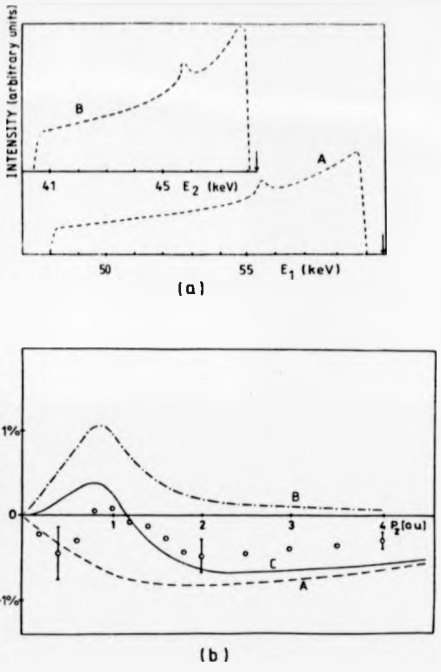

Figure 3.4 (a) The original low energy tail of the 100 mCi ^{241}Am line source after the subtraction of the primary gamma line (A) and B the distribution of the tail after Compton scattering through an angle of 170° and transformed according to the Klein-Nishina cross-section (eq. 1.23). (b) shows the profile asymmetry (A) obtained by using the tail A in (a) convoluted with the free atom Compton profile of carbon and B that induced by the peak position forced by the contribution from source scattering. Curve C is the sum of A and B and is in close agreement with the experimental asymmetry of graphite (○ ○ ○) (see Manninen et al. 1986).

correction is given by curve B which when added to curve A produces agreement to within 1/4% J(0) between experiment and theory, i.e. curve C, for graphite. The residual asymmetry is likely to be due to characteristics of the spectrometer source such as collimation, impurities, encapsulation, etc. which are difficult to assess since it is not possible to position the detector at the sample position.

In summary, isolation of the contribution to the low energy response function tail from source scattering enables a significant improvement to be made to the asymmetry of profiles measured on the ^{241}Am spectrometer system provided the resolution function is measured using the same geometry, collimation and counting rate as used in the actual experiment.

3.3.2.2. The 412 keV Spectrometer Response Function

Due to the availability of a ^{182}Ta calibration source, which has a principal decay line at 159.00 keV, the high energy system was designed so that the Compton peak coincided with this energy which facilitates measurement of the detector resolution function at the most intense part of the scattered spectra.

The need for an accurate detector response function for this system has been illustrated by Rollason (1984) who constructed a set of artificial functions and found the asymmetry of processed profiles to be extremely sensitive to the photopeak : tail height ratio. This sensitivity is indicated in figure 3.5(a) which shows the asymmetry of the |100| Compton profile of chromium measured on the high energy spectrometer (before correction for multiple scattering) processed with the four different response functions shown in figure 3.5(b). These functions, normalised to 500.000 counts in the elastic peak channel, were obtained from three experimental measurements and two calculations of source broadening using a Monte Carlo simulation (the simple 5 mm × 3 mm × 2 mm geometry of the ^{198}Au source facilitates such a simulation). The name of the respective response function is indicative of its composition. RRF1 was measured by recording the intensity emitted by a 10 μCi ^{182}Ta grid source over a period of a week and contains very little

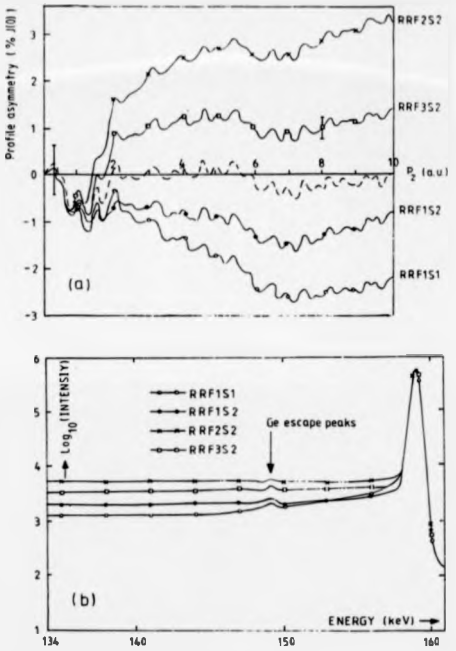

Figure 3.5 (a) The asymmetry of the [110] Compton profile of chromium processed with each of the response functions in part (b) of this figure before correction for multiple scattering. The dashed curve is the asymmetry after application of the multiple scattering correction obtained from RRF1S2 and coincides with the p_z axis within experimental error. (b) the ^{198}Au spectrometer response function measured with a grid source. RRF1. a powder source encapsulated in a glass file with a 1.5 cm diameter detector collimator. RRF2. and the same source with no collimation. RRF3. convoluted with the results of a Monte Carlo simulation of source broadening. S1 or S2. The resultant photopeak intensities are normalised to 500,000.

source broadening. RRF2 was measured by placing a 1.5 cm diameter collimator between a powder 10 μCi ^{133}Te source encapsulated in a glass file and the detector in order to reproduce experimental conditions and intensity was recorded over a period of a few days. RRF3 was measured with the same source and exposure time as for RRF2 but with no source-detector collimation. The following table characterises each measurement in terms of photopeak intensity and peak : tail ratio.

Response Function	Peak : Tail	Peak
RRF1	297	500,000
RRF2	96	25,000
RRF3	209	15,000

Table 3.2 Peak : tail ratio of the response functions RRF1, RRF2 and RRF3 illustrated in figure 3.5(b).

It is readily apparent from this data that there is a high degree of source broadening present in measurements made with the powder source due to scattering within the isotope material and encapsulation. Compton scattering from the collimator in measurement RRF2 effectively lowers the peak : tail ratio as a consequence of the small distances involved between source and detector required to record reasonable intensities. This response, therefore, is not an accurate representation of the actual detector resolution function.

Of the two source broadening simulations, which were performed by Rollason (1985, private communication), S2 contains the higher statistics by an order of magnitude and was calculated for the collimation geometry of the ^{198}Au spectrometer. S1, however, is a

characteristic only of the source geometry and merely provides a first approximation to the source broadening function. The composite response functions shown in figure 3.5(b) were obtained by convoluting the measured detector resolution function with the appropriate source broadening function although each correction is performed independently in the actual data processing. This figure shows that the response functions measured with the powder source (RRF2S2 and RRF3S2) overestimate the intensity of the low energy tail as anticipated and are therefore inadequate for data reduction purposes. It is also apparent from figure 3.5(a) that the profile asymmetry of measurements made on the ^{198}Au spectrometer is sensitive to the effects of source broadening - the data processed with the more representative simulation is $\sim$ 1.3% J(0) less asymmetric at 10 a.u. than that processed with S1. The dashed curve in this figure denotes the profile asymmetry after the correction for multiple scattering has been applied to data processed using RRF1 and S2 and coincides with the p_z axis at all points $\pm$ 0.5% J(0). Since this level of accuracy is of the order of experimental error, then highly symmetric Compton profiles can now be obtained from the high energy system which enables comparison between experiment and theory for both high and low momentum side of the processed line shape. This is a significant improvement on other recent measurements of aluminium (see Cardwell and Cooper, 1986), iron (see Rollason, Holt and Cooper, 1983a) and vanadium (see Rollason, Holt and Cooper, 1983b) which used the composite response function, RRF1S1, in the data processing.

3.3.2.3. Variation of Detector Resolution with Energy.

The discussion so far regarding the response of the detector to a given spectral input has been confined to that either measured, in the case of the ^{198}Au spectrometer, or estimated, in the case of the low energy spectrometer, at the energy coincident with the centre of the Compton peak (i.e. at 159 keV and 48.36 keV respectively). It is apparent from eq. 3.6, however, that the FWHM of the detector response function varies approximately as the square root of the incident photon energy and consequently the distribution

of photons recorded by the detector will vary over the energy range of the Compton peak (-10.0 a.u. to 10.0 a.u. corresponds to a variation of ~ 13 keV for the americium system and of ~ 32 keV for the gold system). Since determination of the detector response as a function of energy is not possible in the absence of a tunable monochromatic source such as synchrotron radiation, particularly for the high energy system, then the assumption of a constant resolution FWHM for processing Compton data requires justification.

In view of the errors associated with deconvolution (see Williams, 1977), current data reduction procedures yield a Compton profile convoluted with a Gaussian of FWHM equivalent to that of the spectrometer response function (i.e. 0.4 a.u. for the ^{198}Au system and 0.57 for the ^{241}Am system). The simplest method of assessing the effect of deconvoluting a variable width response function, therefore, is to consider the asymmetry introduced when a symmetrical profile is convoluted with a variable width Gaussian and the result compared with profiles deduced from the data processing.

The transposition of an energy space response, $\Delta\omega_z$, to a momentum space response, Δp, is obtained from eq. 1.21 by ;

$$\Delta p = \left(\frac{\partial p_z}{\partial \omega_z}\right) \Delta\omega_z \qquad (3.7)$$

In addition the contribution of geometrical broadening to the detector response function, which arises as a consequence of the finite size of the source, detector crystal and collimation has to be considered. This effect essentially describes the smearing of the recorded intensity by the superposition of many individual profiles each based on a different scattering angle. Assuming both resolution and beam divergence effects to be Gaussian, therefore, the total energy space response can be written as a sum of the squares of each contribution i.e. ;

$$\Delta\omega_{tot}^2 = \Delta\omega_{det}^2 + \gamma^2 \qquad (3.8)$$

where $\Delta\omega_{det}$ is the resolution function FWHM and γ is a similar parameter characterising the effect of geometrical broadening. Substituting in eq. 3.7 gives ;

$$\Delta p = \left[\frac{\partial p_z}{\partial \omega_2}\right] (\Delta\omega_{det}^2 - \gamma^2)^{\frac{1}{2}} \qquad (3.9)$$

$$= \left[\frac{\partial p_z}{\partial \omega_2}\right] (\alpha + \beta\omega_1 + \gamma^2)^{\frac{1}{2}} \qquad (3.10)$$

where $\beta = 5.548F\Delta$ from eq. 3.6. The values of α, β, γ, $\Delta\omega_{det}$ and $\Delta\omega_{tot}$ obtained by Rollason (1984) for both experimental systems are given in table 3.3.

Spectrometer	α (keV^2)	β (keV)	γ (keV)	$\Delta\omega_{det}$ (keV)	$\Delta\omega_{tot}$ (keV)
^{198}Au	0.1646	0.00120	0.230	0.5960	0.6388
^{241}Am	0.0836	0.00109	0.067	0.3692	0.3855

Table 3.3 Detector resolution variation parameters. $\Delta\omega_{det}$ is evaluated at the Compton peak position for each experimental system respectively.

By differentiating eq. 1.21, therefore, the momentum space resolution can be determined at all points in the Compton profile as illustrated by figure 3.6. It should be noted, however, that since the spectrometer response function for the low energy system is determined at the incident photon energy, the value of $\Delta\omega_{det}$ at 60 keV is taken to represent the combined effect of resolution and geometrical broadening measured at 48.36 keV (i.e. γ is set to zero in calculating the variation of Δp with momentum). From figure 3.6 it can be seen that the width of the detector response varies linearly with momentum across the Compton profile for both spectrometer systems (i.e. from 0.61 to 0.53 a.u. and from 0.41 to 0.39 a.u. between -10.0 and 10.0 a.u. for the ^{241}Am and ^{198}Au spectrometer systems, respectively). Consequently Δp may be written as ;

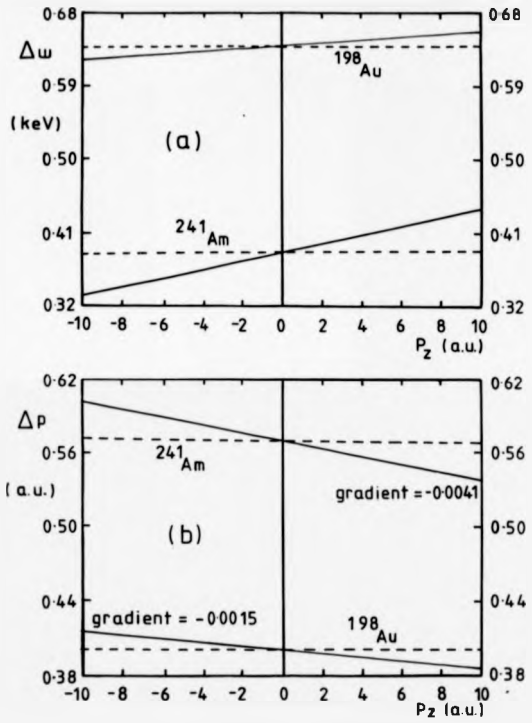

Figure 3.6 Variation in detector response (a) in energy space and (b) in momentum space across the Compton profile for both spectrometer systems. The dashed lines correspond to a constant energy/momentum space resolution function FWHM respectively.

$$\Delta p(q) = \Delta p_0 + \epsilon q \qquad (3.11)$$

where ϵ is the gradient of the appropriate Δp vs. p curve and has the value of -0.0041 for the americium system and -0.0015 for the gold system. Δp_0 is the detector response at the Compton peak position (0.4 and 0.57 a.u. respectively).

3.3.2.4. Formulation of the Variable Width Response Function.

The effect of the variable width response function may be assessed by considering the convolution of a Compton profile with a Gaussian of FWHM, $\sigma(q')$, i.e. ;

$$J(q)^{conv} = \left(\frac{2}{\pi}\right)^{\frac{1}{2}} \int \frac{1}{\sigma(q')} \exp\left(-\frac{(q-q')^2}{2\sigma^2}\right) J(q')\, dq' \qquad (3.12)$$

which corresponds to a smearing of the profile at each momentum point by a constant amount with no net increase in peak area. Substituting eq. 3.11 into this expression gives ;

$$J(q)^{conv} = \left(\frac{2}{\pi}\right)^{\frac{1}{2}} \int \frac{1}{(\Delta p_0 + \epsilon q')} \exp\left(-\frac{(q-q')^2}{2(\Delta p_0 + \epsilon q')^2}\right) J(q')\, dq' \qquad (3.13)$$

It is necessary, therefore, to express eq. 3.13 in the following form ;

$$J(q)^{conv} = \left(\frac{2}{\pi}\right)^{\frac{1}{2}} \frac{1}{\Delta p_0} \int \exp\left(-\frac{(q-q')^2}{2\Delta p_0^2}\right) J(q')\, dq' + \delta \qquad (3.14)$$

whence the effect of the variation in detector response can be described by a correction term, δ, added to the symmetric convolution of the Compton profile with a constant width Gaussian.

From figure 3.8 it is clear that $\epsilon q_{max} << \Delta p_0$ in which case terms $\sim \epsilon^2$ can be neglected in this formulation. Rearrangement of eq. 3.13 gives ;

$$J(q)^{conv} = \left(\frac{2}{\pi}\right)^{\frac{1}{2}} \int \frac{1}{(\Delta p_0 - \epsilon q')} \exp\left(-\frac{(q-q')^2}{2\Delta p_0^2}\right) \exp\left(\frac{\epsilon q'(q-q')^2}{\Delta p_0^3 + 2\epsilon q' \Delta p_0^2}\right) J(q')\, dq' \qquad (3.15)$$

Since $-1 < \dfrac{\epsilon q'(q-q')^2}{\Delta p_0^3 + 2\epsilon q' \Delta p_0^2} < 1$ for all points -10.00 a.u. $\leq p_z \leq 10.00$ a.u. then

the second exponential on the right hand side in the above equation can be expanded as a Taylor series. To first order in ϵ, eq. 3.15 becomes :

$$J(q)^{conv} = \left(\frac{2}{\pi}\right)^{\frac{1}{2}} \int \left(\frac{1}{\Delta p_0} - \frac{\epsilon q'}{\Delta p_0^2}\right) \exp\left(-\frac{(q-q')^2}{2\Delta p_0^2}\right) \left(1 + \frac{\epsilon q'(q-q')^2}{\Delta p_0^3 + 2\epsilon q' \Delta p_0^2}\right) J(q')\, dq' \quad (3.16)$$

$$= \left(\frac{2}{\pi}\right)^{\frac{1}{2}} \int \frac{1}{\Delta p_0} \exp\left(-\frac{(q-q')^2}{2\Delta p_0^2}\right) +$$

$$\frac{1}{\Delta p_0} \exp\left\{-\frac{(q-q')^2}{2\Delta p_0^2}\right\} \left\{\frac{(q-q')^2}{\Delta p_0^3} - 1\right\} \frac{\epsilon q'}{\Delta p_0} J(q')\, dq' \quad (3.17)$$

$$= \left(\frac{2}{\pi}\right)^{\frac{1}{2}} \int J(q')\, G(q-q') + G(q-q') \left\{\frac{(q-q')^2}{\Delta p_0^3} - 1\right\} \frac{\epsilon q'}{\Delta p_0} J(q')\, dq' \quad (3.18)$$

where $G(q - q')$ is a Gaussian. Since this expression is in the form of eq. 3.14, the correction term, δ, may be represented by a convolution of two functions, each of which depends on Δp_0, i.e. :

$$\delta = \frac{\epsilon}{\Delta p_0} \left(\frac{2}{\pi}\right)^{\frac{1}{2}} G(q) \left\{\frac{(q)^2}{\Delta p_0^2} - 1\right\} * q\, J(q) \quad (3.19)$$

Figure 3.7 shows the variation of (a) the product $G(q)\left\{\frac{q^2}{\Delta p_0^2} - 1\right\}$ and (b) the product $qJ(q)$ with momentum for a theoretical [110] Compton profile of chromium (see Rath, Wang, Tawil and Callaway, 1973) for the high energy system. Curves (a) and (b) are symmetrical and anti-symmetrical functions of q respectively and both have zero net area which must necessarily be the case in order to preserve the profile area when the correction is made.

The convolution of the functions illustrated by figures 3.7(a) and 3.7(b) weighted with the appropriate coefficient, $\frac{\epsilon}{\Delta p_0}\left(\frac{2}{\pi}\right)^{\frac{1}{2}}$, are shown in figure 3.7 for (c) the ^{198}Au system and (d) the ^{241}Am system. It can be seen from this figure that the correction is an anti-symmetric function and effectively shifts electron density from negative to positive momentum, thus *reducing* the symmetry of the resultant profile. Although this effect is an

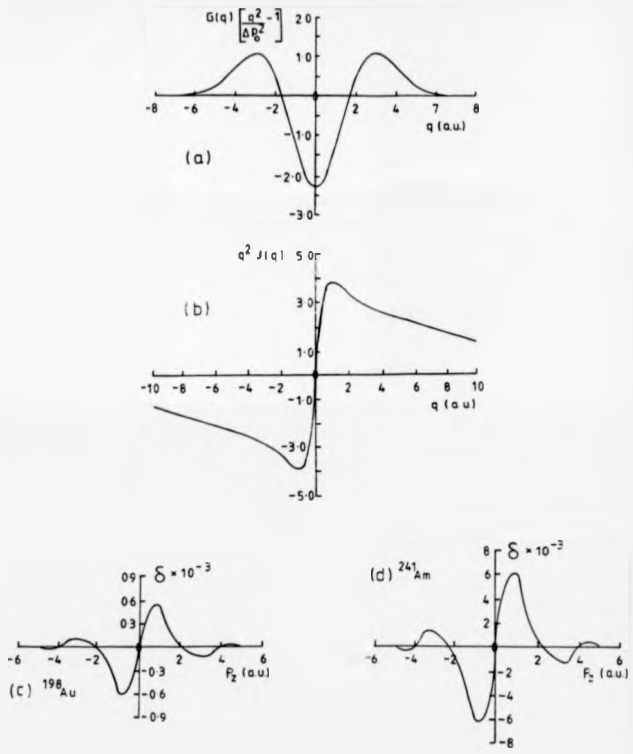

Figure 3.7 The functions (a) $G(q)\left\{\frac{q^2}{\Delta p_0^2}-1\right\}$ and (b) $qJ(q)$ for a theoretical [110] Compton profile of chromium (see Rath et al, 1973) for the high energy spectrometer system. When convoluted these functions describe the effect of a variable width response function on the Compton profile illustrated by (c) for the ^{198}Au and (d) ^{241}Am spectrometer systems.

order of magnitude higher for the low energy spectrometer (~ 0.2 %J(0) c.f. ~ 0.02 %J(0) for the high energy system), it is apparent that neither correction is significant within experimental error (~ 0.5 %J(0)) and hence may be neglected in the data processing within the current levels of experimental accuracy. This null result is important in that it eliminates the variation of the resolution function FWHM across the Compton profile as a significant cause of profile asymmetry for both spectrometer systems.

3.4. Recent Developments in the Data Processing

The most significant change to the data processing made during this period of research was the re-ordering of the corrections for detector efficiency and deconvolution of the response function tail from observed spectra, necessitated by the higher degree of accuracy to which Compton experiments can currently be performed. Additionally the efficiency correction previously applied to the response function before deconvolution was removed. Thus the overall strategy was changed from ;

$$M(\omega) = \eta^{-1}(\omega) \int J(\omega) \left[R^{-1}(\omega - \omega') \eta^{-1}(\omega - \omega') \right] d\omega' \qquad (3.20)$$

where the efficiency correction is first applied to the resolution function and then again to the data after deconvolution to ;

$$M(\omega) = \int \left[J(\omega') \eta^{-1}(\omega') \right] R^{-1}(\omega - \omega') d\omega' \qquad (3.21)$$

where the efficiency correction is applied only to the data after deconvolution. In this form the data processing is sequentially correct and yields profiles of high inherent symmetry.

The effect of this change is illustrated by figure 3.8 which shows the difference between the observed [100] directional Compton profile of chromium processed in the order outlined in section 3.2 and that described by eq. 3.20 for both spectrometer systems. For the low energy system it can be seen that the re-ordering has no significant effect on the processed profile since the detector is ~ 100% efficient over the region of the Compton peak. For the high energy system, however, the re-ordering shifts electron density from the low to the high momentum side of the profile and reduces the asymmetry by

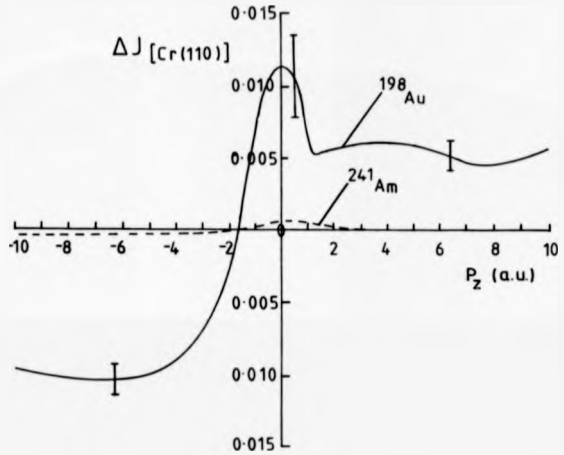

Figure 3.8 The difference between the [110] Compton profile of chromium processed with the efficiency correction applied after and before deconvolution respectively for both spectrometer systems.

approximately 0.3 %J(0) which results in a final lineshape symmetrical to within ~ 0.5 %J(0) at all values of p_x, as illustrated by the dashed curve in figure 3.5(a). This observation suggests that the relatively poor profile symmetry observed in previous measurements can be attributed to the assumption of the wrong processing order.

CHAPTER 4

ALUMINIUM

4.1. Introduction

The objectives of this study are twofold. The first is to deduce accurate directional Compton profiles of aluminium since apart from of a measurement made with an X-ray source, which was severely limited by statistics (see Cooper, Pattison, Williams and Pandey, 1974), previous experiments were concerned only with polycrystalline samples. The second objective is to compare both directional difference and total profiles measured at the two incident energies 412 keV and 60 keV in common use for Compton scattering studies. This is done in the hope of establishing consistency between the two sets of anisotropies and also to indicate the extent to which the individual profiles measured with the lower energy system can be interpreted. Furthermore, since aluminium is accepted as a good free electron metal, this study will provide a stringent test of the ^{198}Au spectrometer data processing if it is to resolve the small differences anticipated between the directional Compton profiles.

4.2. Previous Research

The most recent measurements of the Compton profile of aluminium were published more than one decade ago (see Cooper, Pattison and Schneider, 1976, and Manninen, Paakkari and Kajantie, 1974). These earlier measurements were made on spectrometers utilizing 100 Ci ^{198}Au (E_γ = 411.90 keV, half-life = 2.7 days) and 300 mCi ^{241}Am (E_γ = 59.54 keV, half-life = 458 years) gamma ray sources and were quoted to an accuracy of 0.5 %J(0) at the Compton peak. Good agreement between the absolute profiles was observed at q = 0 although a difference of 4% was apparent at 2.0 a.u. This was possibly

due to different profile normalisation over the range quoted by the different experimental groups. The interim period has seen the implementation of advances made in the data processing as described in chapters 1 and 3; in particular the development of a better understanding of the Compton cross-section (see Ribberfors, 1975 a, b) and the multiple scattering contribution to the measured profile (see Tanner and Epstein, 1976 and Pitkanen, Laundy, Holt and Cooper, 1986). In addition stronger high energy sources now make it possible to produce profiles of greater statistical accuracy and reliability.

Since the tight binding calculation of Tawil (1975) was published, which predicts a difference of 1.5 %J(0) between the directional profiles of aluminium at the origin, other calculations have appeared. An all electron Hartree-Fock calculation (see Causa, Dovesi, Pisani and Roetti, 1981) and an APW calculation (see Kubo, Wakoh and Yamashita, 1976) predict profile anisotropies of 1% and 0.3 %J(0) respectively. A calculation based on the local density approximation (Sacchetti, 1984, private communication) predicts no significant anisotropy. Measurement of the directional profiles, therefore, has been made to resolve the disagreement between these theories and to identify the most appropriate model of the electron momentum distribution of aluminium. Furthermore, comparison between theoretical and experimental absolute Compton profiles measured on the more reliable gold isotope spectrometer should pinpoint the limitations of each band calculation.

Measurement of the single crystal 2-D momentum density of aluminium by the positron annihilation technique (see West, 1980) has been performed by Mader, Berko, Krakauer and Bansil, 1976. The results of this experiment showed the cross-section of the Fermi surface measured in the [001],[100] plane to be almost circular and were in good agreement with the results of an OPW calculation performed by the same authors. This indicates that aluminium is a good free-electron metal and provides an independent experimental basis for assessing the results of the present study.

4.3. Experimental Systems

The 60 keV and 412 keV Compton spectrometers used in this work are described by Holt, 1978, and Rollason, 1984, and are schematically illustrated in figure 4.1 (a) and (b) respectively. The experimental details are very similar to those reported by Rollason, Holt and Cooper (1983b) in a study of vanadium (412 keV) and Cooper, Rollason and Tuxworth (1982) in a study of compositional variations in alloys (60 keV) and hence only a brief outline will be presented here.

The ^{198}Au isotope emitting the 411.80 keV radiation is installed in a spectrometer at the Rutherford-Appleton Laboratory. This source is initially activated to 120 curies and produces usable intensity for about four half-lives (~ 10 days) before it has to be replaced. The scattering angle of the instrument is fixed at 167°, which implies a Compton peak energy of 158.93 keV, and was chosen so that the detector resolution function could be measured at the peak position with a weak ^{182}Ta source (E_γ = 159.00 keV). The cross-section of the beam at the sample position is about 250 mm^2 and the detector - sample distance is 46.2 cm.

The 5 Ci ^{241}Am spectrometer is located at the University of Warwick and has a scattering angle of 170.5°, i.e. a Compton peak energy of 48.36 keV. The cross-section of the beam is roughly 530 mm^2 at the sample position, although the detector only sees an area of 250 mm^2 due to the collimation, and is positioned 19.5 cm from the sample.

Both experimental systems detect the scattered photons with solid state intrinsic germanium detectors and the scattered spectra are recorded on 4096 multichannel analysers. They also incorporate high scattering angles in order to maximise the energy transfer between photon and electron (eq. 1.7) although the ideal configuration of 180° back scattering geometry is not achievable due to shielding requirements and the finite size of the source and detector.

Drifts in amplifier gain and ADC conversion arising principally from environmental temperature variation are minimised by air conditioning for both spectrometer systems.

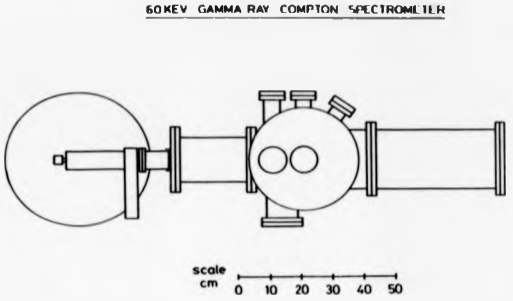

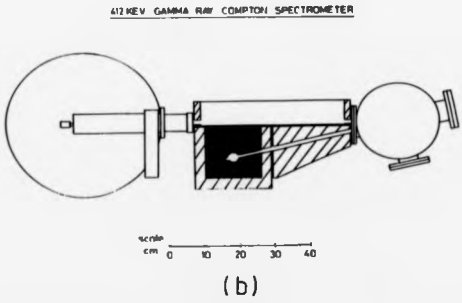

Figure 4.1 Schematic representation of (a) the ^{241}Am spectrometer (60 keV) located at the University of Warwick and (b) the ^{198}Au spectrometer (412 keV) located at the Rutherford-Appleton Laboratory.

The degree of electronic drift before and after sample exposure for the ^{241}Am isotope experiment is assessed by continual monitoring of the width of the elastic line (E_γ =59.54 keV). In the case of the ^{198}Au study the amount of drift is indicated by the positions and widths of ^{57}Co decay lines occurring at energies several keV below the Compton peak (E_{γ_1} = 121.94 keV, E_{γ_2} = 136.31 keV) produced by a ~ 10 μCi ($T_{\frac{1}{2}}$ = 290 days) source taped to the detector head. In neither case was the long term line width after each measurement significantly greater than its value when measured on a short exposure.

Since commercially available sources are limited to relatively low strengths the annular geometry of the low energy source is necessary in order to obtain a high scattered intensity. This construction, however, hinders the measurement of absolute directional profiles since the scattering vector is not uniquely defined but lies along the generator of a cone of semi-angle ~ 5.1° with the sample at the apex. Subsequent measurements made on this system, therefore, are averaged over all crystal directions on the surface of the cone and the true directional profiles cannot be obtained. Additionally, as indicated in chapter 3 (see also Holt, DuBard, Cooper, Paakkari and Manninen, 1979), the low energy spectrometer is more susceptible to energy dependent approximations made in the data processing than the ^{198}Au system. These absolute profiles, therefore, are less reliable than those acquired with the gold isotope spectrometer.

The ^{198}Au isotope offers better resolution (0.40 a.u. compared to 0.57 a.u. of momentum at the Compton peak) than ^{241}Am although the accuracy of measurements is more limited by statistical uncertainty in the raw data (the short half-life of the source typically prevents more than 10^7 counts to be recorded under the Compton line). Conversely the long half-life of the americium isotope allows long exposure times only limited by instrumental electronic drift and typically up to 10^8 counts under the Compton line can be reasonably obtained. The accuracy of measurements made using the ^{241}Am spectrometer, however, is limited by systematic errors associated with the low energy transfer, which jeopardise the impulse approximation (see section 1.5), and uncertainties in the spectrometer response function which determine the momentum resolution (see section

3.3.2.1). In particular it has proved difficult to recover the inherent symmetry of the Compton line $|J(+p_z') = J(-p_z')|$ for measurements made on this system which limits the extent to which individual profiles can be interpreted. Fortunately the directional difference profiles are insensitive to these systematic errors which facilitates comparison with the theoretical anisotropies convoluted with the appropriate resolution FWHM. The data acquired with the 412 keV source usually show adequate profile symmetry to encourage the interpretation of individual profiles as illustrated by recent measurements of iron (see Rollason, Holt and Cooper, 1983a), copper (see Bauer and Schneider, 1983b) and nickel (see Rollason, Schneider, Laundy, Holt and Cooper, 1987).

4.4. Experimental Details

Aluminium discs 450 mm^2 area by 2 mm thick were cut from cylindrical single crystal bars of different orientations ([111], [110] and [100]). These samples were significantly larger than the beam size at the sample position for both spectrometers. Although this made them easy to position in the beam path and maximised the count rate, it significantly increased the multiple scattering contribution to the spectrum, particularly from the penumbra region (see Williams, 1977).

Individual spectra were accumulated over a period of 70 - 200 hours depending on source activity for the gold system and for 100 - 300 hours for the americium system where the emitted flux is effectively constant. The resultant recorded intensity under the Compton peak for the high energy system was about 25×10^6 which was significantly less than the corresponding intensity for the americium system where the total number of counts under the peak was approximately 6×10^6. The gold system measurements, however, had characteristically the better signal to noise ratio of 800 : 1 compared with 36 : 1 for the ^{241}Am system at the Compton peak (i.e. 0.5% and 3% respectively).

In total three separate gold sources were used for this investigation over a period of two months and the [111] and [100] orientations were measured twice to check reproducibility.

The spectral distributions of multiple photon scattering were obtained from Monte Carlo simulations developed from the work of Felsteiner, Pattison and Cooper (1974). The resultant multiple profiles each contained approximately 2000 photons from an input of 10^6, multiply and singly "scattered" over all angles. Figure 4.2(a) shows the multiple profile of aluminium for the high energy system. The dashed curve represents a cubic spline fit to the Monte Carlo output (solid line) and is used to correct Compton data in order to avoid introducing random statistical fluctuations to the single profile. The form of this profile corresponds to a value of α of 1.082 (i.e. $\sim$ 8% of the total scattering) and is very similar to that observed for the low energy system (not shown) for which α was calculated to be 1.091 ($\sim$ 9% of the total distribution). This difference is expected since the mean free path of 412 keV radiation in aluminium is greater than that of 80 keV (i.e. 4.12 cm compared with 1.54 cm) and hence the probability of multiple scattering is lower in the former. Figure 4.2(b) shows the variation in the profile peak height [J(0)] measured on the low energy system for 1, 2, 5 and 10 mm thick aluminium [111] samples. Extrapolation of this curve to zero thickness yields a value of 3.78 $\pm$ 0.02 electrons per a.u. which is in good agreement with the peak height after application of the Monte Carlo correction (3.80 $\pm$ 0.02). Although this indicates the validity of the simulation result it does not provide evidence for the reliability of the low energy measurements since the data plotted in this figure is subject to the same systematic errors present in the directional measurements. Crystals of different thicknesses were not measured on the high energy system in view of the limited usable intensity emitted by each gold source.

The effect of the multiple scattering correction is to increase the peak height of the Compton profile by 6.8% and 6.3% for the ^{241}Am and ^{198}Au systems respectively and to lower the tails, where this effect dominates, to the free atom value. This is illustrated by figure 4.3 which shows the difference between the experimental and free atom profiles as a function of momentum for all three orientations and both spectrometer systems. The difference in resolution between the two experimental systems is apparent from the intersection of each curve with the ordinate axis ($\sim$ 1.0 for the higher energy and $\sim$ 0.7 for the

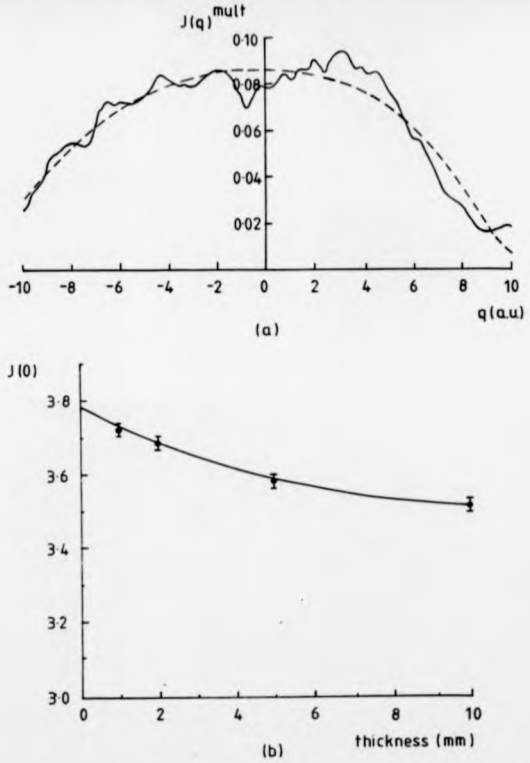

Figure 4.2 (a) multiple profile of aluminium for the high energy spectrometer system ($\alpha = 8.2^{\circ}$). The solid curve is the Monte Carlo simulation output and the dashed curve a cubic spline fit to this data. (b) The variation of J(0) with sample thickness for profiles measured on the low energy system. Extrapolation to zero thickness predicts a peak height of 3.78 ± 0.02 electrons per a.u. for the single Compton profile.

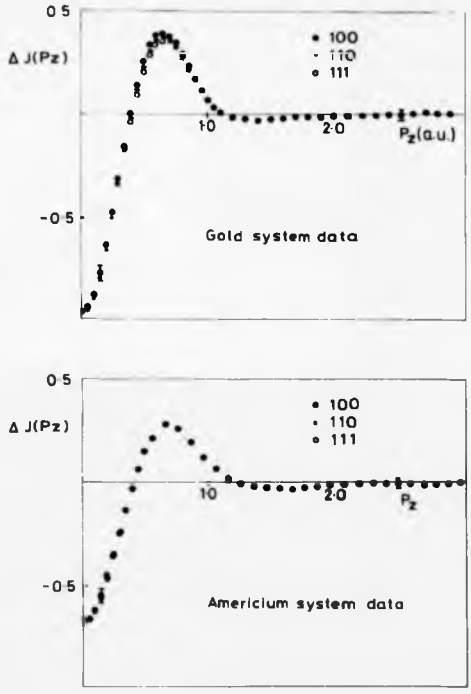

Figure 4.3 Experiment - free atom difference profiles for the three principle directional Compton profiles of aluminium measured on both spectrometer systems. Good agreement is necessarily observed between experiment and free atom at high values of momentum.

americium system).

The variation of detector efficiency with energy for the ^{198}Au system was corrected for by the Monte Carlo simulation of the scattering and absorption processes in the germanium detector crystal described in section 3.3.1. No correction for efficiency is necessary for the low energy system since the detector is virtually 100% efficient over the Compton peak region (see figure 3.2).

4.5. Results and Discussion

4.5.1. The Band Structure Calculations

The experimental results have been compared with four calculations as indicated in section 4.2. The APW method used by Kubo et al (1976) to calculate Compton profiles provides a good description of the band structure and the density of states and accurately reproduces the Fermi surface. The calculation of momentum density was carried out over 273 reciprocal lattice vectors with a cubic mesh of 505 k-points in the irreducible volume equivalent to 1/48 of the Brillouin zone. It does not, however, include terms describing the effects of electron exchange and correlation in the lattice potential.

The self-consistent field exact exchange Hartree-Fock calculation made by Causa et al (1981) uses a LCAO method to obtain the electronic wavefunction with each atomic orbital consisting of a linear combination of four Gaussian basis functions fitting each Slater-type orbital. The exclusion of electron-electron shielding effects by this method tends to overestimate the individual one electron potentials although this is cancelled to some extent by the absence of a correlation term in the lattice potential. As a consequence of this cancellation this calculation is found to reproduce accurately the Fermi surface.

The calculation made by Tawil (1975) generates the electronic charge distribution from a set of Cartesian-Gaussian primitive wavefunctions obtained from a self-consistent modified tight binding model. The value of the Fermi energy deduced from this model, however, produced a different connectivity with the Fermi surface at the W symmetry

points of the Wigner-Seitz cell to that observed experimentally (see Cracknell and Wong, 1973) and consequently was not used to determine the directional profiles. Instead Tawil chose a value of E_f to reproduce the required connectivity which increased the number of band electrons to 3.1. When a compensatory rescaling factor is introduced (i.e. 0.97), however, the consequential distortion of the Compton lineshape near the Fermi surface is so significant that the 111 directional profile cannot be used for meaningful comparison with experiment. Although the 110 and 100 directions for this calculation are presented here it must be emphasised that their reliability is also suspect.

The fourth theory currently available is that of Sacchetti (1984, private communication) which employs the charge density of Moruzzi, Williams and Janak (1978) to calculate the Compton profile within the slowly varying density approximation (i.e. a modification of the local density approximation) and includes a correlation term in the one-electron potential. There is no indication how well this theory describes the Fermi surface.

Theories which calculate the momentum wavefunctions by Fourier transforming the solutions to the Kohn-Sham equations (i.e. those based on the local density approximation such as that of Sacchetti) do not yield the true momentum density because correlation effects are not properly treated (see Chapter 6). They may be corrected by adding the Lam-Platzman term (eq. 2.33) to the Compton profile as outlined in section 2.7. The input for $J^{h}_{[\rho(r)]}(q)$ in eq. 2.33, which represents the Compton profile of the homogeneous interacting electron gas with the (local) charge density, $\rho(r)$, is calculated from an analytic expression for the 3D momentum density, given in section 6.3.1.1. $\rho(r)$ is taken from the tabulated density functional muffin-tin charge densities by Moruzzi et al (1978). This calculation is relatively simple for the regions of constant charge density occupied by the conduction electrons but becomes more complicated in the core region. The effect of the correction is to smear out the Compton profile obtained from the Kohn-Sham "pseudo-wavefunctions" i.e. it promotes electrons to higher momentum states as described in chapter 6.

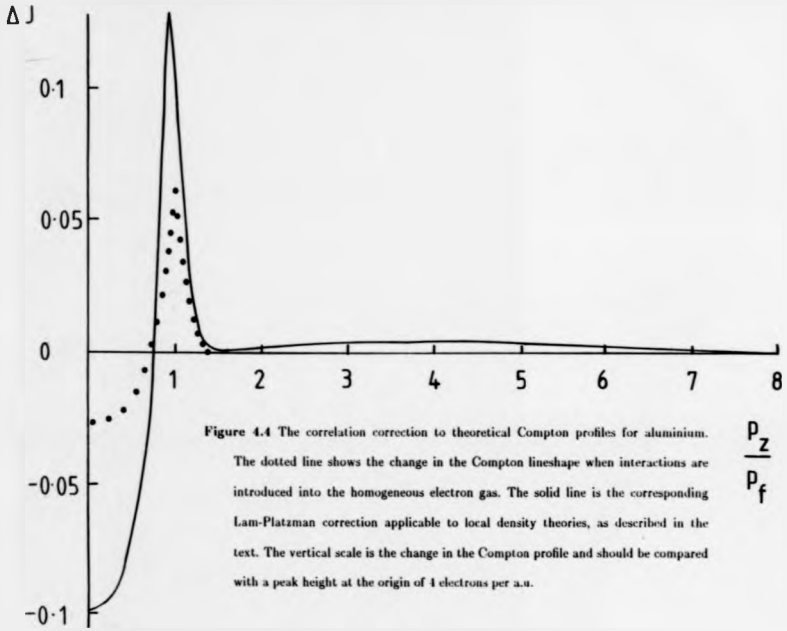

Figure 4.4 The correlation correction to theoretical Compton profiles for aluminium. The dotted line shows the change in the Compton lineshape when interactions are introduced into the homogeneous electron gas. The solid line is the corresponding Lam-Platzman correction applicable to local density theories, as described in the text. The vertical scale is the change in the Compton profile and should be compared with a peak height at the origin of 4 electrons per a.u.

Figure 4.4 shows the Lam-Platzman correction for aluminium along with the interacting - free electron gas difference profile, $J^{int}(p_z) - J^{free}(p_z)$, from which the former was derived. Both shift electron density from low to high momentum. Comparison of the two lineshapes shown in this figure indicates that although both have a similar shape, the Lam-Platzman correction has a significantly larger effect on the total profile. Its contribution to the total energy of the system may be deduced from the second moment of the profile through the application of the virial theorem (see section 2.2). It apparently increases the electronic kinetic energy by approximately 30 eV per atom (compared to a cohesive energy of 7.28 eV for aluminium). Whilest this value is of the correct order of magnitude little significance can be placed on it because the calculation is very prone to small errors in the Lam-Platzman correction at high momentum. Indeed, a shift of only 0.025 %J(0) in the baseline of $\Delta J^{LDA}_{|\rho(r)|}(q)$ changes the kinetic energy by 30 eV per atom.

4.5.2. Difference Profiles

Both sets of experimental directional difference profiles are shown in figure 4.5, together with the variation predicted by the APW calculation. It is immediately obvious that both experiment and theory display a very small anisotropy, the differences amounting to $\sim \pm 1/4$ %J(0) at low momenta. The americium spectrometer is much more successful in measuring these effects because of the superior statistical accuracy of its data ($\sigma \sim \pm 1/10$ %J(0) c.f. $\pm 3/10$ %J(0) for the ^{198}Au system). Systematic errors which may plague the individual profiles are isotropic and therefore of no consequence in the directional difference. On the other hand the anisotropy is comparable to the standard deviation of the higher energy data where the oscillations are not so well established. The magnitude of these oscillations implies a relatively spherical Fermi surface such as that illustrated by figure 4.6, which is calculated for a free electron gas, and is characteristic of a good free electron metal. It can be seen from this figure, which assumes three electrons per primative cell, that the free electron Fermi sphere of aluminium extends to the third Brillouin zone although only part of this structure is shown (see Mackintosh, 1963). The iso-

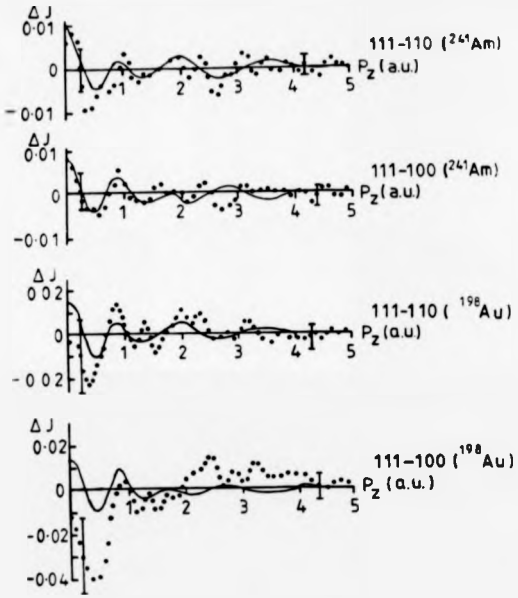

Figure 4.5 Experimental anisotropies for data acquired on the americium and gold spectrometer systems. The solid line shows the corresponding APW theory difference profiles which have been convoluted with a Gaussian of 0.57 a.u. and 0.40 a.u. FWHM for comparison with measurements made with the ^{241}Am and ^{198}Au isotopes respectively. The full ordinate scales displayed are approximately $\frac{1}{200}$ J(0) for the gold system data and $\frac{1}{400}$ J(0) for the more sensitive americium system data.

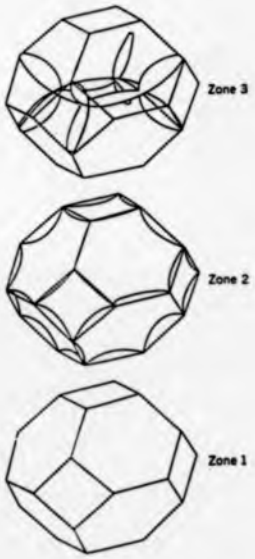

Figure 4.6 Reduced zone representation of the free electron Fermi sphere of aluminium with 3 valence electrons per primitive cell. The second Brillouin zone is almost full with electrons. The complex structure of the third zone is only shown in part (after Kittel, 1976).

tropic nature of the momentum distribution of a free electron gas is indicated by the sphericity of the contours in the second and third zones respectively.

The small scale of the experimental anisotropy is in good agreement with the results of the 2-D ACAR experiment of Mader et al (1976) and can be used to differentiate between the available theories. Referring to figure 4.7, the Tawil theory clearly overestimates the magnitude of the measured difference for the 110 - 100 anisotropy by roughly a factor of four whereas the slowly varying density calculation of Sacchetti predicts no significant profile difference which is much closer to the experimental result. The self-consistent exact exchange Hartree-Fock calculation on average overestimates the magnitude of the profile anisotropies by roughly a factor of two, although they are of the same frequency and occur in approximately in the same position as those detected experimentally. From figures 4.5 and 4.7 it is apparent that the most successful theory in predicting the observed profile anisotropies of aluminium is the APW calculation of Kubo et al, hence the inclusion of this calculation alongside experiment in figure 4.5. Not only is the scale of the anisotropy predicted correctly but, as the more precise low energy data shows, the oscillations in the data are followed closely by the APW theory.

In an attempt to interpret the observed profile anisotropies a calculation based on a simple Wigner-Seitz model was performed (see section 2.5.3) in which free electron spheres were centred on the [111] and [200] reciprocal lattice sites each weighted uniformly with the high order momentum coefficients, $|A_G(0)|^2$ (i.e. 0.0097 and 0.0030 respectively) taken from Mader et al (1976). The directional profiles were then obtained by integrating over successive planes in the direction perpendicular to the appropriate lattice vector. This essentially involved summing the squares of the chords defined by the intersection of the plane of integration with the free electron spheres at 0.01 a.u. intervals. The magnitude of the difference profiles predicted by this method below the Fermi momentum is comparable to experiment. Above p_f, however, the period with which they oscillate deviates from that observed due to the neglection of the third nearest neighbour coefficients. Consequently this calculation is too approximate to describe the anisotropic behavior above the Fermi

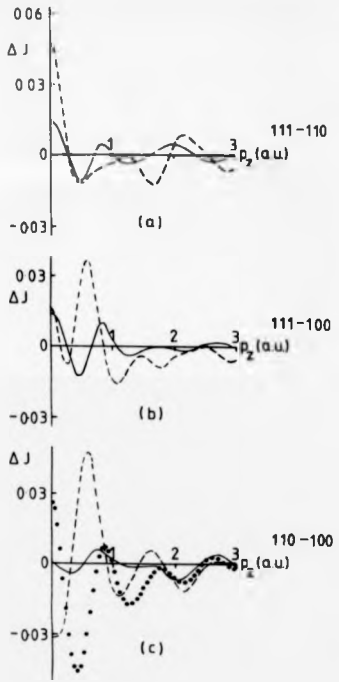

Figure 4.7 Theoretical profile anisotropies for the APW (solid lines) and Hartree-Fock (dashed lines) calculations. The tight binding model [110] - [100] anisotropy is included in (c) (dotted line). The local density based calculation does not predict any anisotropy, i.e. it corresponds to the horizontal momentum axis. All theories have been convoluted with a Gaussian of 0.40 a.u. FWHM.

momentum on this fine scale.

4.5.3. Comparison of Measurements at High and Low Energies.

Since the momentum density is a centro-symmetric function, observation of the lineshape symmetry about $p_z = 0$ is an important test of the quality of the processed data as discussed in Chapter 3. Figure 4.8 shows the profile asymmetry for the 100 profile deduced from both experiments. It can be seen that the profiles acquired from the low energy system have significantly poorer symmetry than those measured with the gold spectrometer (profiles differ by more than 2% of the peak height at ± 1 a.u. compared to a difference of only 0.25 %J(0) for those measured on the higher energy spectrometer). It should be noted, however, that this study was performed before the data processing was re-ordered as described in section 3.2. Since re-processing is not trivial, the profiles presented in this chapter are of lower inherent symmetry than that potentially obtainable by application of the re-ordered data reduction as illustrated in the experimental study of chromium described chapter 5.

As outlined in the preceding chapter various factors contribute to the poor inherent symmetry of profiles measured with the low energy system. Firstly the resolution is not measured at the Compton peak. Secondly the energy variation of the resolution function is greater (from 0.61 au to 0.53 au over the range $-10 < p_z < +10$ a.u. ; the comparable figures for the ^{198}Au system being 0.42 au to 0.39 au). In addition the validity of the impulse approximation for this system is questionable since the energy transfer corresponding to intensity recorded at the centre of the Compton peak is only $\sim$ 10 keV greater than the K-shell binding energy (E_B = 1.559 keV) and consequently these electrons do not contribute fully to the profile at high momenta. Finally there is greater beam absorption at the lower energy and a higher background due to a larger beam size. By considering the effects of scattering within the americium source the symmetry of profiles measured on the low energy system may be significantly improved as described in Chapter 3. After taking this into account, however, a residual asymmetry of $\sim$ 1.5 %J(0)

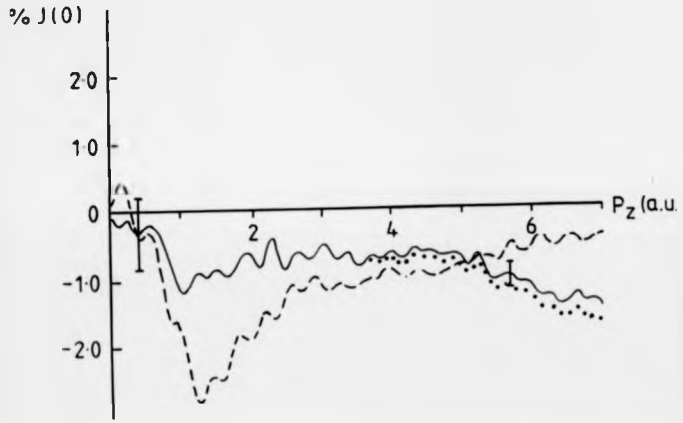

Figure 4.8 Asymmetries in the [100] Compton profiles measured on both spectrometers and expressed as a percentage of the profile peak height. The solid and dashed curves represent the profile asymmetry after correction for multiple scattering for ^{198}Au and ^{241}Am system data respectively. The ^{198}Au profile asymmetry before correction for multiple scattering is given by the dotted line. The shape and magnitude of the asymmetry is representative of all the directional profiles.

at ~ 1.3 a.u. and ~ 0.1 %J(0) at ~ 5.0 a.u. still remains which is difficult to improve upon without an accurate knowledge of the spectrometer response function (see section 3.3.2.1). As discussed in section 4.3 the lower energy system predicts anisotropies with a higher statistical accuracy than the gold system and eventually it is hoped that these experiments may be used to determine absolute profiles if more sophisticated data reduction procedures can be devised. For the moment only the higher energy data are used for comparison of individual experimental and theoretical profiles. Fortunately the differences between the measured and calculated Compton profiles are larger (~ ± 1 %J(0)) than the statistical errors of the former (~ ± 3/10 %J(0)) and whereas the high energy data are not precise enough to pinpoint the anisotropies in the momentum density they can be used with confidence to establish the difference between experiment and theory for individual profiles. In this way the two experimental systems complement each other.

4.5.4. The Individual Profiles

The ^{198}Au experimental profiles normalised to the free atom value of 6.145 electrons between 0 and 7 a.u. were found to agree within 0.2 %J(0) with the free atom curve in the high momentum limit. This, together with acceptable centrosymmetry of the profiles, indicates that the systematic corrections had been properly applied. The profiles are listed in table 4.1. Figure 4.9 shows the differences $J(p_z)^{theory} - J(p_z)^{exp}$ for all three orientations measured on the gold spectrometer for three of the theories discussed in the previous sections. The conduction electron profiles for the local density, APW and Hartree-Fock calculations are quoted by their authors out to 1.1 a.u., 2.45 a.u. and 3.5 a.u. of momentum and have areas of 2.46, 2.94 and 3.06 electrons respectively. Thus over the quoted range the local density and APW theories underestimate the conduction electron contribution to the total profile whereas the Hartree-Fock calculation predicts too great a contribution from these electrons. From the data shown it is clear that the local density and APW calculations significantly overestimate the magnitude of the low momentum contribution to the Compton profile between 0 and 1 a.u. If, however, the Lam-Platzman

Table 4.1 Experimental ^{198}Au and theoretical Compton profiles of aluminium along [111], [110] and [100]. All theories are convoluted with a Gaussian of FWHM 0.40 a.u. corresponding to the experimental detector resolution half-width. The free atom values are taken from Biggs, Mendelsohn and Mann, 1975.

p_z au	[100]			[110]			[111]					
	Exp	Band Theories APW	HF	Exp	Band Theories APW	HF	Exp	Band Theories APW	HF	SVD Theory (isotropic)	Lam-Platzman correction	Free Atom
0.0	3.879 ± 0.020	3.919	3.869	3.874	3.918	3.834	3.866	3.932	3.873	3.917	-0.095	4.477
0.1	3.855	3.892	3.838	3.837	3.891	3.803	3.838	3.903	3.834	3.893	-0.095	4.659
0.2	3.778	3.812	3.746	3.753	3.810	3.715	3.748	3.817	3.729	3.820	-0.091	4.346
0.3	3.642	3.678	3.595	3.623	3.675	3.581	3.607	3.675	3.577	3.694	-0.085	3.896
0.4	3.454	3.488	3.391	3.435	3.484	3.402	3.413	3.478	3.387	3.510	-0.073	3.391
0.5	3.216	3.240	3.137	3.191	3.239	3.171	3.174	3.228	3.154	3.266	-0.055	2.908
0.6	2.924	2.938	2.844	2.902	2.940	2.886	2.892	2.932	2.870	2.966	-0.029	2.495
0.7	2.590	2.600	2.529	2.577	2.605	2.563	2.578	2.603	2.550	2.627	0.004	2.174
0.8	2.265	2.260	2.226	2.250	2.266	2.241	2.263	2.269	2.231	2.282	0.037	1.910
0.9	1.978	1.961	1.964	1.966	1.965	1.962	1.978	1.969	1.954	1.979	0.060	1.774
1.0	1.751	1.734	1.763	1.745	1.736	1.751	1.751	1.737	1.744	1.752	0.065	1.657
1.2	1.503	1.487	1.521	1.496	1.487	1.507	1.491	1.484	1.504	1.504	0.036	1.499
1.4	1.367	1.360	1.384	1.358	1.359	1.381	1.363	1.357	1.375	1.372	0.009	1.377
1.6	1.247	1.244	1.270	1.246	1.242	1.273	1.240	1.243	1.259	1.257	0.002	1.260
1.8	1.135	1.128	1.160	1.127	1.126	1.159	1.130	1.128	1.148	1.139	0.001	1.143
2.0	1.018	1.018	1.052	1.010	1.012	1.042	1.021	1.016	1.045	1.023	0.001	1.028
2.5	0.745	0.765	0.804	0.781	0.767	0.802	0.780	0.766	0.802	0.765	0.003	0.771
3.0	0.577		0.611	0.580		0.611	0.581		0.604	0.583	0.003	0.571
3.5	0.435		0.444	0.444		0.444	0.440		0.452	0.420	0.004	0.425
4.0	0.334		0.340	0.343		0.340	0.340		0.342	0.321	0.004	0.323
5.0	0.214 ± 0.01		0.201	0.213		0.201	0.217		0.201	0.191	0.004	0.199
6.0	0.139		0.130	0.141		0.130	0.143		0.130	0.130	0.003	0.133
7.0	0.085 ± 0.005		0.090	0.090		0.090	0.093		0.090	0.090	0.001	0.091

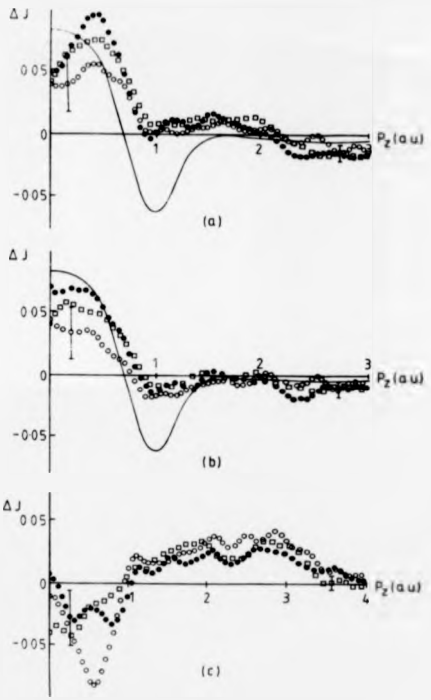

Figure 4.9 The difference between theoretical and experimental directional profiles (i.e. $J(p_z)^{theory} - J(p_z)^{expt}$) for (a) local density (b) APW and (c) Hartree-Fock calculations for the [111] ● ● ●, [110] □ □ □ and [100] ○ ○ ○ directional profiles measured with the high energy spectrometer. The solid lines in (a) and (b) show the Lam-Platzman correction. All theories have been convoluted with a Gaussian of 0.40 a.u. FWHM before comparison with experiment.

correction is taken into account it can be seen in figure 4.9 (a) and (b) that substantially better agreement between theory and experiment is achieved. This correction can be directly applied to the local density based theory shown in this figure since the charge density used for its calculation is identical to that used in Sacchetti's band calculation. Although the Lam-Platzman correction is not strictly applicable to theories other than those based on local density models, it would greatly improve the agreement between the APW theory and experiment as is clear from figure 4.9. The converse is true, however, for the all electron self-consistent Hartree-Fock calculation. As anticipated this indicates that the effect of the electron-electron interaction is overestimated in this model and consequently the conduction electron profile is smeared out to too great a degree. This is in contrast to the situation for beryllium where both Hartree-Fock and local density pseudopotential calculations predict profiles which overestimate the experimental result by ~ 3% at the origin after the correlation correction has been made (see Bauer and Schneider, 1983a).

The profiles derived from the tight-binding model of Tawil are in poor agreement with experiment, differing by roughly 2.5 %J(0) at the origin (compared with about 1% for the APW theory and 1.3% for the Hartree-Fock calculation) and they are not reproduced in figure 4.9. This suggests that the tight-binding model is relatively poor for the purposes of predicting Compton profiles for this good free electron metal although quantitative assessment is difficult due to the unreliability of this particular calculation. The reverse has been found to be true for the transition elements where the atomic nature of the d-wavefunctions are generally better described by the LCAO approach (see Rollason, Holt and Cooper, 1983 a, b and Bauer and Schneider, 1983b).

4.5.5. Reciprocal Form Factors

The significance of presenting Compton data in B-function form is that the majority of systematic errors associated with obtaining a Compton profile are slowly varying functions of momentum and are therefore compressed into a small region around the origin of

position space on transformation (see section 2.6). Additionally the long range behavior of the reciprocal form factor is characteristic only of the conduction electrons since the flat, extended core contribution in momentum space transforms to a localised, narrow distribution in position space. The values of B(s) at high s, however, are suppressed by the experimental resolution which appears as a Gaussian damping function with σ = 7.3 Å corresponding to the resolution FWHM of 0.4 a.u. The data at intermediate values of s, therefore, potentially contain the most information and are technically simple to interpret.

The successive values of the reciprocal form factor at lattice translation vectors, **R**, correspond to a series of terms describing the 3D Fourier transform of the Fermi surface with all filled bands giving zero contribution (see section 2.6). Although the high order components of B(**R**) cannot be readily obtained from Compton scattering studies, the difference between theoretical and experimental B-functions at low **R** is indicative of the accuracy of the predicted occupation function (i.e. $n_{\mathbf{k}}$ (**k**) in eq. 2.29).

The reciprocal form factor for the [110] direction (i.e. the nearest neighbour direction in an f.c.c. lattice), obtained by Fourier transforming the Compton profile, for the calculated and measured data is shown in figure 4.10. From eq. 2.29 it may readily be deduced that the the value of B(s) at s = 0 is equal to the atomic number of the scatterer. For aluminium B(0) is found to be 12.96 (not shown in figure 4.10) which indicates that transformation of the Compton profile to real space has been performed correctly. Unfortunately the data at the first lattice translation vector (i.e. $\sqrt{2}a$ = 5.6 Å for the [110] direction) is too damped to enable any meaningful interpretation. It is apparent, however that the overlap of the wavefunction is greatest at ~ 2.8 Å (indicated by the arrow) which corresponds to approximately that of the nearest neighbour distance. The differences between the experimental and calculated B-functions at this point are given in table 4.2 after addition of the transform of the Lam-Platzman correction (open circles) to the theoretical data.

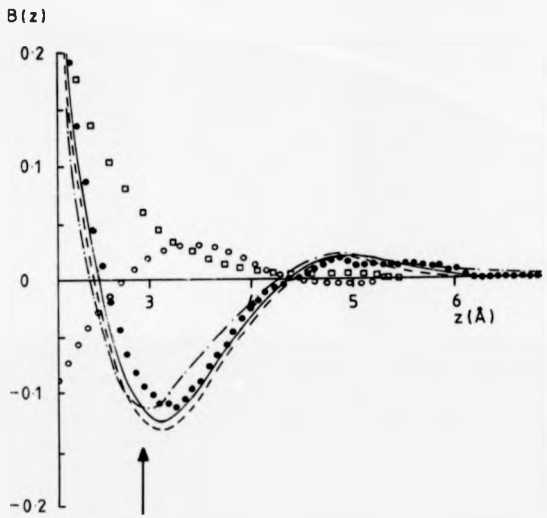

Figure 4.10 Reciprocal form factor for the [110], nearest neighbour, direction of aluminium [• • • experiment, — · — Hartree-Fock (see Causa et al, 1981), dashed line SVD (see Sacchetti, 1984), solid line APW (see Kubo et al, 1976) and □ □ □ free atom (see Biggs et al, 1975)]. The open circles denote the isotropic Fourier transform of the Lam-Platzman correction. The experimental error at intermediate values of z are of the order of the radius of the dots. This B-function is very similar in both shape and magnitude to that of the other two principle directions which indicates the free electron like behavior of the conduction electrons in aluminium. The arrow corresponds to a lattice translation of $\frac{a}{\sqrt{2}}$.

	Experiment	APW	SVD	H-F
B(R)	-0.072 ± 0.010	-0.079	-0.089	-0.079
ΔB(R)	0.000	0.007	0.017	0.007

Table 4.2 The difference between experimental and theoretical B functions at the lattice translation corresponding to the position of greatest overlap of the wavefunction.

When this correction is taken into account at no point in the entire spatial distribution does either theory deviate from the experimental B-function by more than than two standard deviations of the experimental error which indicates that each is relatively successful in calculating the occupation function. This provides further evidence of the free-electron like behaviour of the conduction electrons in aluminium although in this case effectively prevents resolution between the different band calculations.

CHAPTER 5

CHROMIUM

5.1. Introduction

The main objective of this study is to extend a series of measurements on the 3d transition metal elements and in so doing establish the most appropriate band calculation employed to describe the behavior of the 3d electrons.

The structure of chromium at room temperature is b.c.c. (the so called α phase) with a lattice constant of 5.3 a.u. although a transition to f.c.c. does occur at 1840 °C (the β phase). Chromium exists in an anti-ferromagnetic state below its Neel temperature (311.5 K) and it is for this state that current band calculations have been applied. This experimental study was performed at room temperature (i.e. ~ 15 K below T_N) although the observed profiles are independent of magnetic effects in the absence of circularly polarised radiation and an applied **B** field (see section 1.4.1).

The physical and chemical properties of transition metal elements and compounds are determined, to a large extent, by the population of the d orbital energy levels. In the solid the crystal field splits the 3d states into two non-degenerate symmetry groups, t_{2g} and e_g, the occupancy of which is determined by the strength of the ligand interaction (see Coulson, 1961). This is in contrast to good free electron metals, such as aluminium, where the s band conduction electrons occupy plane wave states.

For octahedral coordination such as that observed in chromium, the e_g and t_{2g} splittings can be described in terms of a higher energy doubly degenerate orbital set that point at the electron repelling ligands and a lower energy triply degenerate set that point between and avoid the ligands, respectively. Accurate determination of the occupancy of

these states is central to the deduction of the momentum distribution in subsequent band calculations and it is to this end that an extensive study of the 3d transition series has been made over the past decade.

In chromium the orbital population of the e_g and t_{2g} states has been observed through both X-ray charge density measurements (see Diana and Mazzone, 1972 and Ohba, Saito and Wakoh, 1982) and neutron spin density measurements (see Stassis, Kline and Sinha, 1973 and Moon, Koehler and Trego, 1986) to be ~ 28% and 72% respectively. These occupancies describe an aspherical radial charge density relative to the free atom which must be taken into consideration in subsequent band calculations.

Recent research has been concerned with measuring the directional Compton profiles of iron (see Rollason, Holt and Cooper, 1983a), vanadium (see Rollason et al, 1983b), nickel (see Rollason, Schneider, Laundy, Holt and Cooper 1987) and copper (see Bauer and Schneider, 1984). The results of these measurements, all of which were made on elements possessing cubic symmetry, have been compared with a variety of band calculations, notably APW, LCAO and LDA models. Apart from scandium and manganese, which are difficult to obtain in pure crystalline form, the remaining 3d transition metal elements, i.e. titanium, cobalt and zinc, are hexagonal in structure and therefore difficult to model for the purposes of band calculations. Consequently this study will complete all practical investigations of the 3d series by the Compton scattering technique.

5.2. Previous Research

5.2.1. Experimental Studies

The earliest experimental measurement of the directional Compton profiles of chromium was by Weiss (1973) who used Ag K_α X-rays (E = 22.17 keV) incident on a [100] single crystal. A second directional measurement was then made by rotating the crystal about the [110] direction to present the [111] face to the incident radiation. Consequently this study employed two different scattering geometries. The resultant data were obtained by adding together many measurements for each orientation to record a total

intensity of $\sim 10^5$ counts in the region of the Compton peak and were normalised to the free atom value of 9.7 between 0 and 5 a.u. The data reduction consisted essentially of subtracting a straight line background from the observed spectra followed by transformation from energy to momentum space via eq. 1.21. No correction for the energy dependence of the Compton cross-section, sample absorption or multiple scattering was applied to the data which subsequently shows a large experimental error at the Compton peak ($\sim$ 2.5 %J(0)). The difference between the directional profiles (i.e. [111] - [100]) was $\sim$ 7 %J(0) at the origin which suggested a build up in momentum density around the origin along the [111] direction - the direction of nearest neighbours in the b.c.c. lattice. Good agreement between both profiles and the free atom value was observed in the high momentum limit. The crudity of the processing of these measurements coupled with the low energy transfer associated with the X-radiation ($<$ 2 keV for $Ag_{k_{\alpha_1}}$ radiation) limits the extent to which these experimental profiles can be interpreted.

In 1974 Ohara, Fukamachi, Hosoya and Takeda used ^{241}Am γ-radiation (60 keV) incident on a spherical single crystal sample oriented appropriately to measure the [111], [110] and [100] directional profiles of chromium. A total of 75,000 counts were recorded in the Compton peak channel (width $\sim$ 30 eV) for each measurement. The resultant densities were normalised to the free atom value between 0 and 5 a.u. Since no correction for relativistic effects, absorption or multiple scattering were applied in the data processing only the profile anisotropies were interpreted. They were, however, almost an order of magnitude more accurate than the Weiss data and indicated a difference of $\sim$ 4 %J(0) at the Compton peak between the [111] and [100] measurements (compared with $\sim$ 7 %J(0) for the earlier measurement). The results were found to be in good qualitative agreement with a LCAO calculation performed by Rath, Wang, Tawil and Callaway (1973) although the experimental anisotropies were consistently less than the theory over the entire momentum range published (i.e. 0 to 5.0 a.u.).

The only other Compton profile measurement of chromium was performed by Paakkari, Manninen and Berggren (1975) who used 60 keV γ-radiation incident on a

polycrystalline sample. Although all the directional properties were lost in such a measurement the subsequent data were corrected for multiple scattering, sample absorption and the energy dependence of the Compton cross-section and were consequently accurate to within 1 %J(0) at the Compton peak. The isotropic experimental profile was compared with the results of a renormalised free atom model (RFA) in which Bloch functions for the 4s band electrons were obtained by simply truncating the corresponding free atom wavefunction at the Wigner-Seitz sphere and renormalising it to one to preserve charge neutrality. The best agreement with the experimental data from such a model was observed for a $3d^4 4s^2$ configuration with equal weighting given to the t_{2g} and e_g orbital populations (i.e. corresponding to a spherical charge distribution). Additionally the data compared well with a spherical average of the directional Compton profiles derived from the LCAO calculation of Rath et al.

5.2.2. Theoretical Studies

In the LCAO calculation by Rath et al (1973) the wavefunctions for all except the 3d states were constructed from a linear combination of Gaussian-type orbitals (GTO's) - see Wachters, 1970. For the 3d functions, 5 separate GTO's were used to account for the t_{2g} and e_g degeneracies due to the presence of the crystal field. The total electron wavefunction was then evaluated at 140 points over $1/48^{th}$ of the Brillouin zone - the primitive volume element of a cubic mesh. The sum of the contributions to the Compton profile from individual electron bands was subsequently deduced by summing over 3000 reciprocal lattice points (i.e. out to $\sim$ 3500 a.u.) and was found to converge quickly for the band states (i.e. 4s and 3d). For the core states, however, where small exponents of the wavefunction are encountered, the convergence was much slower and consequently the contributions from the 2s and 2p electrons were incomplete. No contribution from the 1s electrons was included with the result that the published directional profiles are deficient in area by $\sim$ 2.08 electrons to 7 a.u. The majority of this missing density, however, can be included by adding a 1s Hartree-Fock free atom distribution to the published data. No

attempt to include the effects of electron exchange and correlation was made in this calculation.

A second available band calculation is by Wakoh, Kubo and Yamashita, 1976, who used the APW method to calculate the momentum distribution of the conduction electrons. This calculation uses a modified X_α potential, such as that described by eq. 2.3.1 (see Wakoh and Yamashita, 1973), and was determined to reproduce the observed Fermi surface behaviour in an applied B field, i.e. the de Haas-van Alphen effect (see Kahn and Frederikse, 1959, for a complete description). The energy values were calculated at 55 points in the irreducible Brillouin zone from 50 angular momentum dependent APW's with a maximum orbital value of L = 6 for the volume outside the Fermi surface. Within this surface values of L up to 4 were included and the momentum distribution was determined from Bloch functions for 87 reciprocal lattice vectors (i.e. up to the 8^{th} nearest neighbours in k-space). $J(p_z)$ was then derived by summation over each occupied **k**, obtained by linear interpolation of each cubic mesh. The t_{2g} states were found to be below the Fermi level and were occupied with a weighted population of 72%. Unlike the LCAO model this calculation includes the effects of electron exchange although it takes no account of correlation (see section 6.1.1). It does, however, reproduce well the Fermi topology and accurately predicts the antiferromagnetic energy gap.

Although the APW calculation completely describes the three dimensional momentum density out to ~ 100 a.u., the resultant Compton profiles are on average deficient by 0.16 electrons. This discrepancy arises because $J(p_z)$ is deduced by integrating $n(\mathbf{p})$ over all values of p_x and p_y (i.e. between p_x and ∞ - see eq. 2.8) and hence the contribution to the Compton profile is restricted to values of momentum less than 100 a.u. in this formulism. This has been consistently observed in other transition metal studies by Rollason et al (1983 a, b) which have revealed deficiencies in the number of conduction electrons present in the APW Compton profiles of vanadium and iron.

In the case of chromium, both calculations predict a build up in momentum density at the origin in the [111] direction and agree well in the period with which the profile

anisotropies oscillate. They differ, however, by up to ~ 6 %J(0) in the amplitude of these oscillations with the LCAO model consistently predicting the greater anisotropy.

At the moment the predictions of the band calculations remain unresolved in the absence of accurate experimental data. It is the intention of this study to highlight the relative merits and limitations of each calculation by comparing the absolute profiles, anisotropies and B-functions with those measured on the high energy spectrometer.

In addition to Compton data, information about the electron momentum density can be gleaned from positron annihilation studies. Such a study of chromium has been made by Shiotani, Okada, Sekizawa, Wakoh and Kubo (1977) who reported the angular correlation functions of the three major crystallographic directions, i.e. [111], [101] and [001]. These results revealed a concentration of momentum density along the [111] direction which was confirmed by the results of an APW calculation by the same authors. In general this study was limited by poor statistics and it is hoped that substantially better agreement between experiment and theory will be achieved here.

5.3. Experimental Details

The [111], [110] and [100] directional Compton profiles of chromium were measured on the gold and americium spectrometer systems described in section 4.3. The single crystals, purchased from Metals Research, Cambridge, were approximately cylindrical with the dimensions given in table 5.1.

The ratio of the sample area to that of the incident beam at the target position for the high and low energy spectrometers is typically ~ 0.33 and 0.16 respectively, which represents a significant loss in intensity of scattered radiation (i.e. ~ 70% and 85%). To ensure that the maximum count rate was obtained, therefore, photographs of the incident beam were taken and the samples positioned accordingly.

Individual spectra were accumulated over a period of 50 to 150 hours depending on source activity for the gold system measurements and for ~ 320 hours for those made on the americium spectrometer. This enabled an intensity of ~ 32×10^6 and 28×10^6 counts

to be recorded under the respective Compton peaks. No electronic drift was observed during either experiment. The background contribution at the centre of the Compton line was ~ 1% for the high energy system, allowing for source decay, and ~ 4% for the ^{241}Am system. These values are greater than those observed for the aluminium study due to the smaller diameter of the samples used in this study (i.e. ~ 10 mm compared with ~ 20 mm).

Sample orientation	Average diameter (mm)	Thickness (mm)	Area (mm^2)
111	11.76	2.2	108 ± 2
110	9.63	2.0	72 ± 1
100	9.31	2.0	68 ± 1

Table 5.1 Geometrical parameters of the single crystal chromium samples.

The spectral distributions of multiple scattering were obtained from two Monte Carlo simulations per experimental system necessitated by the different sample thicknesses. A cubic spline fit to each multiple profile was then made to reduce the amount of noise introduced to $J(p_z)$ when the correction was applied. The multiple profiles for the gold spectrometer system were obtained from an input of 4.1 million photons (compared with 1 million used in the aluminium study) with each distribution containing ~ 10^4 counts over the range -7 a.u. < p_z < 7 a.u. The two distributions were clearly separable and corresponded to values of α of 1.176 (t=2.2mm) and 1.154 (t=2.0mm). This is as expected since the ratio of multiple to single scattering is directly proportional to sample thickness provided each scattering event occurs within one mean free path of the incident radiation in the target material (i.e. ~ 13 mm for 412 keV

radiation in chromium). The less accurate multiple profiles for the low energy spectrometer were calculated from an input of $\sim 10^8$ photons since the processed data is only useful for describing profile anisotropies as discussed in sections 3.2 and 4.4. The corresponding values of α, which were used to scale the individual profiles before the directional differences were taken, were found to be independent of sample thickness, i.e. $\alpha = 1.13 \pm 0.01$ in both simulations. This is due to the shorter mean free path of 60 keV radiation in chromium ($\sim$ 1.3 mm) relative to the target thickness.

The efficiency correction made to the measured lineshape was the same as that applied to the aluminium data and is illustrated in figure 3.2. The ^{198}Au experimental profiles were normalised to the free atom value of 10.70 between 0 and 7.0 a.u. and were found to reduce to within 0.03 %J(0) of the free atom curve in the high momentum limit as illustrated by figure 5.1. The [111] and [100] directional profiles are omitted from this figure for the sake of clarity although their shape and amplitude is typical of that observed for the [110] free atom - experiment data.

5.4. Results and Discussion

5.4.1. Profile Symmetry

The directional profiles were obtained by the application of the modified data processing described in section 3.2 and are of excellent centrosymmetry as illustrated by the dashed curve in figure 3.5(a). The remaining asymmetry of the [110] directional profile, which again is characteristic of all the profiles measured, is effectively zero within experimental error over the entire momentum range plotted and represents a significant step forward in the extent to which observed data can be reduced (prior to this measurement experimental profiles have been at least 0.5 %J(0) asymmetric at some point in the distribution). This enables data from both sides of the profile to be interpreted in contrast to previous transition metal measurements (see Rollason et al 1983 a, b and 1987) in which only data from the high momentum side of the profile, or at best a left/right average to describe the anisotropies, has been presented. The high degree of symmetry observed in

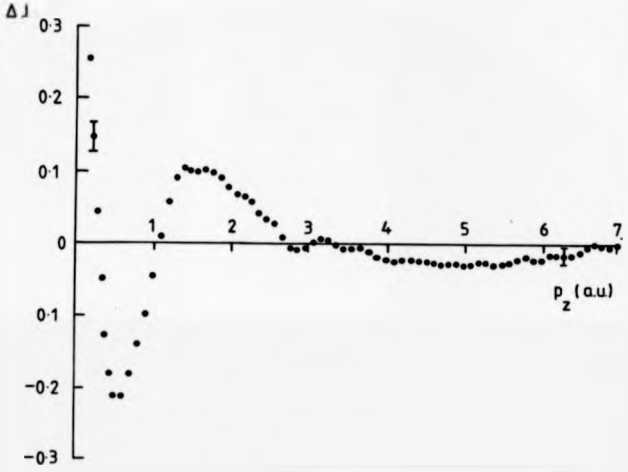

Figure 5.1 Free atom - experiment for the [110] Compton profile of chromium measured on the high energy spectrometer. The form of this curve is characteristic of all three directional measurements.

the ^{198}Au experimental profiles and their reduction to the free atom limit at high momenta indicates that the data processing has been applied successfully.

The profiles measured on the low energy spectrometer were also normalised to the free atom value between 0 and 7.0 a.u. and were found to be of low inherent symmetry (typically ~ 2 %J(0) at 1.5 a.u.). This may be attributed potentially to the breakdown of the impulse approximation assumed in the data processing (see section 1.5) which complicates the normalisation of these profiles. Additionally the chromium K binding energy (E_B = 5.99 keV) prevents these electrons contributing to the total profile for momentum values greater than ~ 8.6 a.u. in which case the high momentum tail lies below the free atom limit. In view of these limitations only the profile anisotropies measured on the low energy system will be presented here.

In order to include the total electron momentum density in the theoretical profiles a Hartree-Fock free atom core and 1s distribution were added to the APW and LCAO Compton profiles respectively. The electron deficiency in the former, however, accounts for ~ 5% of the total band electron density which impairs comparison with the individual experimental profiles.

The ^{198}Au, APW and LCAO directional Compton profiles are listed in table 5.2. The theoretical data have been convoluted with a Gaussian of FWHW 0.4 a.u. corresponding to the width of the resolution function for this system. Also tabulated are the Hartree-Fock free atom profile taken from Biggs et al (1975) and the Lam-Platzman correction for chromium calculated via eq 2.33.

5.4.2. Difference Profiles

The experimental difference profiles derived from measurements made on both spectrometer systems are shown in figure 5.2. The profile anisotropies predicted by the APW (solid lines) and the LCAO (dashed lines) band calculations are included in this diagram and have been convoluted with a Gaussian of appropriate width. It is clear from this figure that the datasets obtained from the different spectrometers are in excellent mutual

Table 8.2 Experimental ^{198}Au and theoretical Compton profiles of chromium along [111], [110] and [100]. Both theories and the Lam-Platzman correction are convoluted with a Gaussian of FWHM 0.40 a.u. corresponding to the experimental detector resolution half-width. The free atom values are taken from Biggs, Mendelsohn and Mann, 1975.

P_z au	[100]			[110]			[111]				
	Exp	Band Theories APW	LCAO	Exp	Band Theories APW	LCAO	Exp	Band Theories APW	LCAO	Lam-Platzman correction	Free Atom
0.0	5.017 ± 0.019	5.102	5.107	5.162	5.254	5.258	5.256	5.401	5.462	-0.073	5.789
0.1	5.008	5.085	5.092	5.147	5.232	5.237	5.240	5.358	5.418	-0.073	5.685
0.2	4.971	5.036	5.046	5.077	5.167	5.173	5.157	5.237	5.295	-0.072	5.413
0.3	4.900	4.959	4.972	4.967	5.058	5.068	5.020	5.084	5.111	-0.069	5.084
0.4	4.795	4.854	4.870	4.821	4.908	4.925	4.852	4.866	4.896	-0.066	4.725
0.5	4.666	4.719	4.741	4.653	4.723	4.753	4.656	4.662	4.677	-0.060	4.445
0.6	4.497	4.554	4.587	4.466	4.514	4.561	4.436	4.461	4.469	-0.052	4.224
0.7	4.308	4.359	4.410	4.254	4.291	4.358	4.223	4.258	4.275	-0.041	4.043
0.8	4.108	4.140	4.212	4.093	4.063	4.148	4.016	4.048	4.087	-0.025	3.878
0.9	3.887	3.905	3.995	3.806	3.832	3.931	3.811	3.825	3.892	-0.007	3.713
1.0	3.648	3.657	3.762	3.584	3.597	3.705	3.587	3.584	3.676	0.012	3.542
1.2	3.166	3.149	3.267	3.127	3.117	3.233	3.120	3.073	3.186	0.033	3.177
1.4	2.739	2.683	2.797	2.701	2.653	2.766	2.700	2.622	2.734	0.026	2.805
1.6	2.357	2.281	2.380	2.318	2.254	2.359	2.349	2.277	2.383	0.013	2.449
1.8	2.020	1.931	2.017	2.013	1.932	2.022	2.027	1.955	2.059	0.008	2.126
2.0	1.769	1.664	1.742	1.782	1.678	1.748	1.765	1.675	1.764	0.008	1.844
2.5	1.307	1.238	1.308	1.290	1.220	1.283	1.280	1.206	1.260	0.009	1.315
3.0	0.990	0.986	0.959	0.992	0.986	0.969	0.994	0.984	0.985	0.010	0.990
3.5	0.795	0.800	0.790	0.798	0.808	0.785	0.795	0.808	0.782	0.010	0.788
4.0	0.687	0.657	0.649	0.682	0.658	0.647	0.678	0.658	0.653	0.009	0.656
5.0	0.520 ± 0.005	0.485	0.480	0.528	0.485	0.481	0.515	0.485	0.481	0.003	0.485
6.0	0.396	0.369	0.364	0.406	0.369	0.364	0.392	0.369	0.364	0.001	0.369
7.0	0.299			0.300			0.283			0.001	0.282
10.0	0.155 ± 0.032			0.157			0.153			0.000	0.130

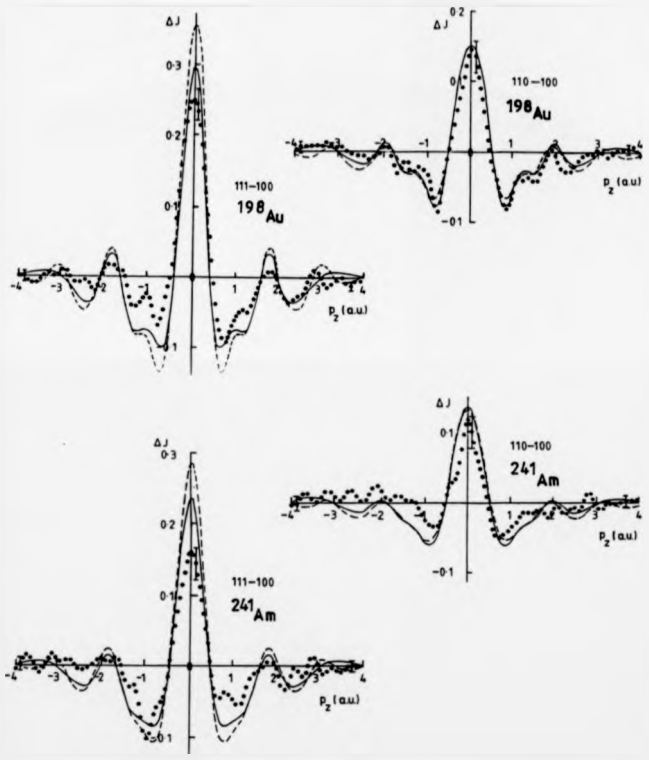

Figure 5.2 The profile anisotropies measured on the ^{198}Au (upper part of figure) and ^{241}Am (lower part of figure) spectrometer systems. The dashed and solid lines correspond to the differences predicted by APW (see Wakoh et al. 1976) and LCAO (see Rath et al. 1973) band calculations respectively which have been convoluted with the appropriate width Gaussian.

agreement and are of comparable statistical accuracy at the Compton peak [$\sigma \sim 0.4\%$ J(0)]. The difference in the net area between high and low momentum sides of the anisotropies for the low energy system, particularly for the [111] - [110] difference, indicates the ambiguity in the profile normalisation. Even so these datasets reveal the fine structure present in the gold system measurements (e.g. at $\pm \sim 1.1$ a.u.).

The APW and LCAO band calculations are in excellent agreement with both sets of experimental [110] - [100] difference profiles. From the curves on the left of figure 5.2 it appears that both theories predict a build up in momentum density along the [111] nearest neighbour direction (i.e. the direction of greatest overlap between secondary Fermi distributions - see section 2.5.3). Although this is observed experimentally, the magnitude of the [111] - [100] anisotropy measured on both spectrometer systems deviates significantly from that predicted by $\sim 2\sigma$ for the APW calculation and by more than 5σ for the LCAO model. This suggests that the effects of exchange and correlation are greatest for the nearest neighbour direction and that the contribution to the [111] directional Compton profile by the former (omitted in the LCAO formalism) is the more significant of the two. On the basis of the data presented in figure 5.2, therefore, the effects of exchange may be estimated to decrease the [111] profile peak height by ~ 0.05 electrons per a.u. at the origin (i.e. the difference between the LCAO and APW calculations), resulting in a shift in density to $\sim \pm 1$ a.u. Since neither calculation includes correlation effects their contribution to the total Compton profile cannot be fully assessed although the experimental evidence suggests that they account for ~ 0.03 electrons per a.u. at the origin (i.e. the difference between the APW and measured [111] - [100] anisotropy).

Apart from the above discrepancies both calculations are in good mutual agreement and accurately reproduce the frequency with which the experimental anisotropies oscillate. Since the directional properties depend on the occupancy of the t_{2g} and a_g orbitals, this indicates that both theories assume the correct population of these states. Consequently the occupancies observed by Diana and Mazzone (i.e. 72% and 28% respectively) are

confirmed by this study.

The results of the LCAO and APW band calculations applied to vanadium are entirely consistent with those presented here (see Wakoh et al, 1976 and Laurent, Wang and Callaway, 1976). In these studies the LCAO method predicts an anisotropy greater typically by ~ 0.02 electrons per a.u. than does the APW calculation, which again excludes the effects of electron correlation.

5.4.2.1. Fermi Geometry

The origin of the oscillations in the anisotropy of chromium can be understood qualitatively by considering its Fermi geometry, which is illustrated in figure 5.3. In this diagram the first Brillouin zone is represented by a dodecahedron. Each Fermi surface is given by a superposition of the contributions from individual bands and is repeated throughout reciprocal space. Complex Fermi geometries are characteristic of the 3d transition metal series and arise essentially as a consequence of the interaction between the d and the less localised 4s electrons (see Cracknell and Wong, 1973).

Part (a) of figure 5.3 is taken from Wakoh et al (1976) and shows schematically the occupancy of the 3rd band which is characterised by hole pockets at the reciprocal lattice symmetry points N and octahedral holes at the points H. Part (b) (taken from Cracknell and Wong, 1973) identifies the composite contribution from the 4th and 5th bands which consists of a large closed region of electrons around the origin, Γ, with "knobs" at its corners, commonly referred to as an "electron jack", and small inter-connecting electron pockets, or "lenses", at the points H respectively. Although the 1st and 2nd band electrons (not shown) almost completely fill the first Brillouin zone, their contribution to the Compton profile is approximately isotropic. Consequently the Fermi distribution of the higher order bands determines the anisotropic structure in the momentum density.

At the origin it is clear that the plane perpendicular to the [111] direction contains only electron jacks at the Γ points of the surrounding zones. For the corresponding planes normal to the [110] and [100] directions, however, both holes from the 3rd band and

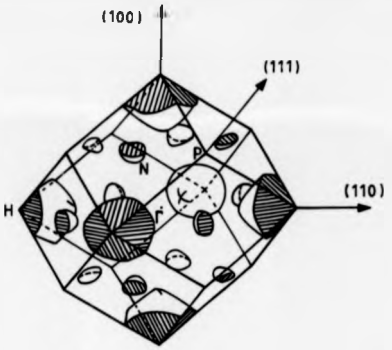

Figure 5.2 (a) Schematic illustration of the closed hole pockets at the symmetry points denoted by N and H in the 3rd band of chromium (taken from Wakoh et al. 1976) and (b) the electron jacks at the origin, Γ, and lenses at H present in the 4th and 5th bands respectively (taken from Cracknell and Wong, 1973). In each case the first Brillouin zone is denoted by a dodecahedron.

electron jacks from the 4th are present at the origin. Since the contribution from the electron lenses in the 3rd band for the antiferromagnetic state of chromium is small (see Wakoh et al, 1976), the individual contributions to the Compton profile in the latter two cases tend to cancel each other out. Consequently at the Γ point the [111] Compton profile should exhibit the greatest momentum density as is confirmed experimentally. This attempt to understand the anisotropic momentum density assumes a free electron density of states below the Fermi level of each band since it makes no reference to the band occupation numbers. Wakoh et al (1976) observed that the t_{2g} orbitals, which account for the majority of the d electron population, lie below this level and are therefore completely filled which justifies this assumption for such a qualitative interpretation.

5.4.2.2. Comparison of the Anisotropies with Previous Measurements

Both experimental datasets are in much better agreement with the LCAO calculation than those reported by Ohara et al, 1974. In that case the theory was found to overestimate experiment by on average ~ 0.2 electrons per a.u. compared with ~ 0.05 electrons per a.u. observed here. A difference that large cannot be attributed to the effects of multiple scattering.

The [111] - [110] anisotropy obtained from the X-ray measurement of Weiss (1973) is in poor agreement with the current experimental data. The magnitude of the early anisotropies are up to 4 times greater than that shown in figure 5.2 (i.e. at ~ 1 a.u.) and oscillate with a period typically ~ 0.2 a.u. slower than the present result. The extent of these discrepancies is undoubtedly due to the poor quality of X-ray measurements and illustrate the sensitivity of Compton data to the small quantitative energy dependent corrections performed in modern day studies. The measured and calculated anisotropies for the directional angular correlations of chromium reported by Shiotani et al (1977) are in reasonable qualitative agreement with the results presented here. The ratios of the [111] to [101] to [001] experimental peak measurements in the positron annihilation study were found to be ~ 1 : 0.98 : 0.95 which compare favourably with the corresponding figures deduced

from the present study (i.e. 1 : 0.98 : 0.96). Although good agreement between the anisotropies measured by Shiotani and co-workers with those derived from an APW calculation was observed for values of momenta below ~ 1 a.u., the theory did not reproduce experiment at high p (i.e. in complete contrast to the Compton results). This could possibly be due to the insensitivity of the positron to the core electron distribution.

5.4.3. The Individual Profiles

Figure 5.4 shows the difference $J(p_z)^{theory} - J(p_z)^{exp}$ for all three directional profiles measured on the gold system spectrometer for (a) the APW and (b) the LCAO calculations, respectively. Both sets of difference curves are plotted for negative and positive values of momentum. This is the first time that measured Compton data have been compared with theory over both sides of the absolute Compton profile.

By inspection of figure 5.4(a) it may be deduced qualitatively that the necessarily symmetric deficiency in electron density derived from the APW model occurs between ~ ± (1 and 3) a.u. The difference between theory and experiment for this calculation is not shown above $| p_z | = 4$ a.u. which represents the upper limit of the published data. The corresponding curves for the LCAO calculation are presented over the same momentum range in the bottom half of the figure. This is because the LCAO model predicts a lower high momentum tail than that calculated for free atom which is probably due to the normalisation problem associated with the incomplete 2p and 2s contribution to the total profile. The area resulting from this discrepancy (i.e. for $| p_z | > 4$ a.u. in the difference curves) is ~ −0.06 electrons per a.u. for each side of the lineshape which accounts for the net positive area in figure 5.4(b). With this observation the APW profiles are the more reliable of the two band calculations.

It is clear that both calculations significantly overestimate the magnitude of the low momentum contribution to the total profile between ~ −1 and 1 a.u. For the APW model this trend is similar to the corresponding difference observed for aluminium in the previous chapter. The greatest difference is observed for the [111] directional profile (solid

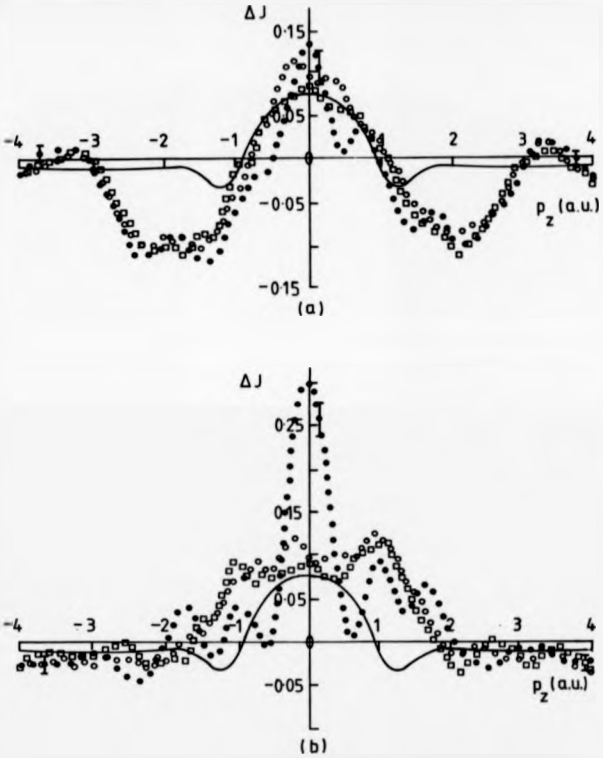

Figure 5.4 Theory - experiment for (a) the APW calculation of Wakoh et al, 1976, and (b) the LCAO calculation of Rath et al, 1973, for measurements made on the high energy system. Data for the [111] (● ● ●), [110] (○ ○ ○) and [100] (□ □ □) directional profiles are shown in each case. The theoretical data has been convoluted with a Gaussian of FWHM 0.4 a.u. corresponding to the width of the experimental resolution function. The solid line represents the Lam-Platzman correction for chromium and should be subtracted from the difference profiles.

dots) for both band calculations. This is consistent with the evidence provided by considering the profile anisotropies in the previous section and confirms that the effects of exchange and correlation are most significant for the nearest neighbour direction. Since the [110] and [100] curves for both sets of difference profiles have roughly the same value at the origin (i.e. $\sim$ 0.1 electrons per a.u.) it may be deduced that the effect of exchange in these crystal directions is small.

5.4.3.1. The Correlation Correction

The Lam-Platzman correction for chromium is represented by the solid line in figure 5.4(a) and should be subtracted from the difference data. Although the agreement between experiment and theory is substantially improved by application of this correction to the LCAO data in figure 5.4(b), the residual difference is greater than that achieved for the APW model. This indicates that the core charge density used to calculate the APW Compton profiles is a better approximation to that employed in the formulation of the Lam-Platzman correction (see Morussi et al, 1978). In any event application of this correction to the results of non-local density band calculations can only describe qualitatively the effects of exchange and correlation.

To investigate the validity of the Lam-Platzman correction further, figure 5.5 shows the [111] theory - experiment difference for both calculations after application of $\Delta J^{LDA}(p_z)$. The bottom part of the figure shows the set of [110],[001] planes in the f.c.c. reciprocal lattice (i.e. those normal to the [111] reciprocal lattice vector). For simplicity the Fermi surface of chromium has been represented by free electron spheres located at reciprocal lattice points in the repeated zone scheme. Although this is a rather crude approximation to the Fermi surface illustrated in figure 5.3, the detailed shape of the conduction electron momentum distribution is not important since the Compton profile is smeared with the broad (0.4 a.u.) resolution function. The plane spacing normal to the [111] direction of the reciprocal lattice, indicated by the dashed vertical lines, was calculated from the lattice parameter to be 0.97 a.u. To interpret the effects of the localised

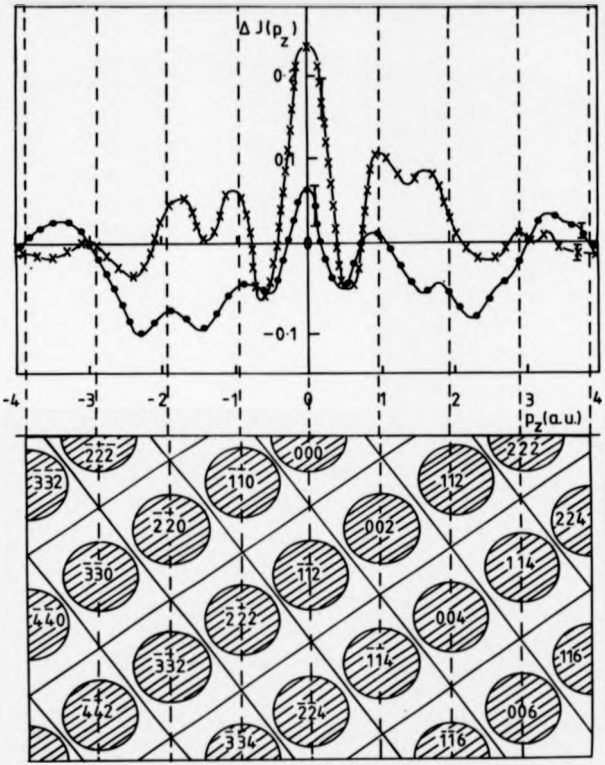

Figure 5.5 Upper part : The difference between the LCAO (× × ×)and APW (● ● ●) band calculations and experiment after application of the Lam-Platzman correction. The lower part of the figure represents the [110]-[001] plane of the first Brillouin zone with the Fermi surface of chromium described as free electron spheres in the repeated zone scheme.

secondary Fermi surfaces on the conduction electron Compton profile it is necessary to integrate the momentum density in the planes indicated. It is clearly visible that the extrema of the difference between experiment and theory coincide with the extrema of the cross-sectional area of the Fermi spheres for the momentum range shown. The symmetry of the difference confirms this observation.

The form of figure 5.5 suggests that the Coulomb correlation transfers electrons from the "occupied" Fermi spheres to the "unoccupied" interstitial regions of reciprocal space and that its inclusion in each respective theory would reduce the amplitude of the observed oscillations. Since these oscillations persist after the Lam-Platzman correction has been applied they must be attributed to non-local effects (i.e. those outside the local density approximation within which the correction was calculated - see section 6.2.1). Since the [110] and [100] difference curves do not exhibit the large scale oscillations present in the nearest neighbour data (see figure 5.4), the effects of exchange and correlation in the corresponding theoretical profiles are much less significant. Consequently their exclusion from the APW and LCAO band calculations is relatively unimportant.

From figure 5.4 it is clear that the APW calculation is in better overall agreement with experiment than the LCAO tight-binding model. This is primarily the result of the underestimation of the directional Compton profiles at high p_z (i.e. relative to the free atom) by the latter calculation which is manifest as an amplification of the peak height. When APW and LCAO calculations were compared with experiment for measurements made on iron (see Rollason et al, 1983a), however, the tight binding model was found to be better suited in describing the 3d states. The success of the APW calculation for chromium and aluminium suggests that the incorporation of an angular momentum dependence of the band electron states is extremely effective for describing both free-electron like and transition metals. The LCAO model, on the other hand, has only proved successful in describing tightly-bound, atomic-like states.

5.4.4. Reciprocal Form Factors

The reciprocal form factors obtained for the principal orientations of chromium are shown in figure 5.6. As found in other transition metal studies (e.g. vanadium and iron - see Rollason et al. 1983 a, b) the oscillatory features of the theoretical B-functions are characteristically more pronounced than their experimental counterparts. In general the LCAO B-functions are in reasonably good agreement with those calculated from the APW model which indicates that the electron deficiency in the latter does not influence the form of the reciprocal form factor over the spatial range shown.

As with the difference profiles presented in the previous section, the most interesting direction of the B-function is that of nearest neighbours. From part (a) of figure 5.6 it can be seen that both theories predict a large overlap of the wavefunction at $\frac{\sqrt{3}a}{2}$ (= 2.4) Å which corresponds to a translation of a lattice vector in the [111] direction - i.e. where B(r) represents the first Fourier coefficient of the Fermi shape function as described in section 2.6. This feature, however, is only visible as a slight flattening of the experimental data. This is consistent with the experimental B-functions of nickel and copper (see Rollason et al, 1987). Since B(r) involves the overlap of integrals over planes in position space (i.e. defined by eq. 2.16), the smaller peak in both theories at ~ 3.3 Å corresponds to the projection of the [110] lattice translation onto the [111] direction (i.e. occurring at $\frac{2a}{\sqrt{3}}$). This is the second [110] plane encountered along this direction - the first occurs at $\frac{a}{\sqrt{3}}$ (= 1.7 Å) and is too close to the origin to be distinguished from the [111] overlap itself. Again the experimental data shows only a slight indication of this peak. At the lattice translation vector, a, in the [111] direction (= 4.8 Å), the autocorrelation of the theoretical wavefunctions assume a minimum although the relatively poor statistics of the experimental result at this point prevents resolution of this.

After adding the transform of the Lam-Platzman correction (open circles), the APW calculation accurately reproduces the observed [111] B-function between ~ 2 and 3.5 Å

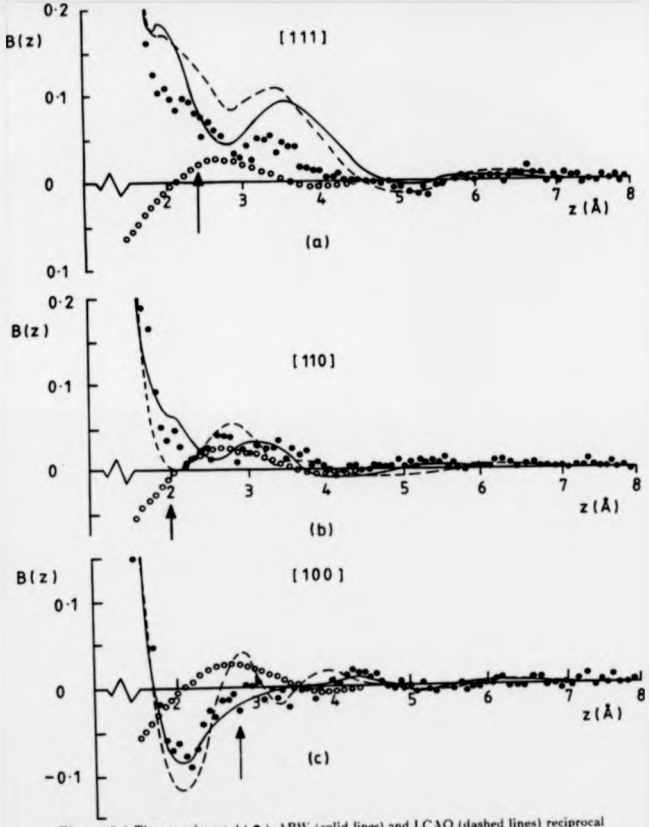

Figure 5.6 The experimental (●), APW (solid lines) and LCAO (dashed lines) reciprocal form factors for (a) the [111], (b) the [110] and (c) the [100] orientations of chromium. The open circles represent the Fourier transform of the Lam-Platzman correction which should be added to the theoretical B-functions. The arrows correspond to lattice translations of $\frac{\sqrt{3}a_0}{2}$, $\frac{a_0}{\sqrt{2}}$ and a_0 respectively.

which indicates that the occupation function derived from this model is more representative of experiment than that calculated by the LCAO method. In the latter case there is a residual difference of ~ 0.1 between theory and experiment up to ~ 4 Å. The difference between the two calculations for this directional B-function could be attributed to the exclusion of exchange effects in the LCAO model.

Good agreement in the magnitude of experiment and theory is observed for the |110| and |100| reciprocal form factors after application of the Lam-Platzman correction. The position of the greatest wavefunction overlap in the |110| B-function (i.e. $\frac{a}{\sqrt{2}} = 2.0$ Å) is indicated by the arrow and appears as a small peak in the APW calculation. The corresponding LCAO B-function at this point, however, predicts a minimum. Since the experimental data lies between these extremes, i.e. at 2.0 Å, no resolution between the two calculations can be made. In the |100| autocorrelation both theories reproduce the negative dip at ~ 2 Å evident in the experimental data although the peak in the LCAO calculation at the first lattice translation vector (2.8 Å) is completely missing from both the measured and APW B-function.

In conclusion it appears that any large scale features in the B-function may be attributed to the effects of exchange and correlation which, for chromium, are most significant in the |111| directional measurement. Further interpretation, however, is difficult due to the limitations imposed by the experimental resolution with many features apparent in the theoretical data either completely missing or only barely distinguishable in the experiment. Only for data of considerably higher statistical accuracy [$\sigma < 0.1\ \%J(0)$] would the B-functions become a valuable tool to interpret Compton data and at present provide little more than a qualitative description of the autocorrelation of the wavefunction.

5.5. Summary

The experimental Compton profiles presented in this chapter are the first to be observed with effectively no asymmetry within experimental error after application of the

data reduction procedure. This facilitates a comparison between theory and experiment over both sides of the profile and so maximises the amount of information that may be extracted from this study.

Good agreement is observed between the experimental profile anisotropies of chromium and those derived from APW and LCAO band calculations. The observed build up in momentum density along the [111] direction is consistent with a qualitative interpretation of the Fermi surface. The difference between theory and experiment, however, reveals that both band calculations overestimate the low momentum contribution to the absolute Compton profiles. For the [110] and [100] differences, this discrepancy is significantly reduced by the application of the Lam-Platzman correction to the theoretical data. Conversely the presence of the high momentum oscillations in the [111] difference data, which remain evident after ΔJ^{LDA} has been applied, may be attributed to the breakdown of the local density approximation assumed in formulating the correction term.

Of the two calculations available, the results of the APW model are in better overall agreement with experiment although this could be due to a problem with the normalisation in the LCAO formulation. Coupled with the results for aluminium, presented in the preceding chapter, the APW method has been found to provide a reliable description of both good free electron and transition metal elements.

CHAPTER 6

EXCHANGE AND CORRELATION EFFECTS IN MOMENTUM DENSITY STUDIES

6.1. Introduction

This chapter is concerned with the treatment of exchange and correlation effects in metals. It describes for the first time a method of calculating their effect on the Compton profile which can be followed for all electron density distributions. The subsequent modification of the results of local density based band calculations to take account of exchange and correlation effects significantly improves the agreement between experiment and theory. This development, therefore, facilitates a critical assessment of theoretical Compton profiles and reduces the residual discrepancy between measured and modelled momentum densities that has been consistently observed in previous studies.

The complexity of a particular band model depends on the nature of the conduction electrons under investigation. For good free electron metals, such as aluminium, the valence electrons are well described by plane waves whereas, in general, atomic wavefunctions are more representative of the conduction electron distribution in transition metals. Whichever basis is adopted the solution is obtained within the independent particle approximation (IPA) which assumes that $\Psi(\mathbf{r})$ can be expressed as a superposition of orthogonal one-electron wavefunctions.

The basic model of the conduction electrons in a metal is that of a free electron gas and it is characterised by an isotropic momentum distribution. Deviations from free electron behaviour arise from two principal sources - firstly the Coulomb interactions between

the conduction electrons and secondly their interaction with the ion cores. In general, therefore, the motion of electrons in condensed systems is highly correlated. As a result the concept of an interacting electron gas has to be introduced. This is achieved by the inclusion of an extra term in the one-electron potential to account primarily for the effects of exchange and correlation - i.e. a modification of the Hartree formulism (see Ziman, 1964). To some extent this term is contrived since it describes all effects not included in the IPA and may consequently be "tailored to fit" depending on the study in hand. Nonetheless the concepts of exchange and correlation are physical and affect the one electron wavefunctions derived from a given band calculation.

6.1.1. Exchange and Correlation

The spin-dependent interactions between the electrons in a given system can be separated into two catagories (see Gunnarson and Lundqvist, 1976). The exchange interaction is that included in the Hartree-Fock method (see Fock, 1930 a, b) and arises as a consequence of the Pauli exclusion principle. Correlation, on the other hand, is a collective term used to describe the spin-dependent interactions not included in this formulation (such as the interaction between electrons of anti-parallel spin). The following sections describe qualitatively the effects of exchange and correlation on the properties of an interacting electron gas.

6.1.1.1. The Exchange Interaction

For a uniform charge density, n_0, exchange can be understood by considering the anti-symmetry of the wavefunction and its effect on the spatial electron distribution. Since the Pauli exclusion principle forbids two electrons of parallel spin to sit on the same site, the charge density relative to an electron at the origin of the gas is given by the product of n_0 and the pair correlation function, g(r) (which describes the distribution in the frame of reference of the electron at r = 0 - see Lundqvist and March, 1983). Consequently the probability of finding another electron with respect to the electron at $r=0$ varies from ½ at r=0, to unity as r tends to infinity (at which point the charge density

becomes independent of the electron at the origin and reverts to its mean value, n_0). Each electron, therefore, effectively carries around itself a positive cloud - i.e. an "exchange-hole". Lundqvist and March show that the potential energy per electron of the exchange hole is given by the following expression ;

$$E_x = -\frac{e^2}{2}\int \frac{n_0\,|g(r) - 1|}{r}\,dr \qquad (6.1)$$

where $n_0.g(r) - 1|$ corresponds to the hole density. Assuming a homogeneous, or Fermi, distribution (i.e. the lowest available energy states of the gas are occupied) this expression reduces to ;

$$E_x = -\frac{3e^2}{4}\left(\frac{3n_0}{\pi}\right)^{1/3} \qquad (6.2)$$

whence exchange effects can be described as a unique function of the charge density. The significance of this result will become clear in section 6.2.

6.1.1.2. The Exchange-Correlation Hole

When correlation effects are introduced to the system (i.e. those beyond the Hartree-Fock approximation), electrons of antiparallel spin around the origin of the pair correlation function repel one another, thus further reducing the total energy of the distribution. Correlation between electrons, therefore, arises predominantly as a consequence of the interaction between electrons of opposite spin with its extent being determined by the long range Coulomb potential.

The effects of exchange and correlation are usually described collectively in terms of the interaction between individual "exchange-correlation holes". The exchange-correlation hole may be regarded as a depression in the electron distribution caused by the motion of a given electron through the gas. Together the hole and electron constitute a "quasi-particle" and it is their motion that is independent, rather than that of individual electrons. Each quasi-particle necessarily carries with it a charge of e and interacts with its neighbours via a screened Coulomb potential. The contribution of this interaction to

the total energy of an electron gas may be treated as a perturbation on the Hamiltonian which forms the basis for the inclusion of exchange and correlation effects in band structure calculations. The following sections describe how these effects on the momentum distribution can be identified from a knowledge of the electron charge density.

6.2. Density Functional Theory

Density functional theory (DFT) is an exact ground state formulation for the treatment of an inhomogeneous, interacting electron system of electrons. The development of DFT stems from the observation of Hohenberg and Kohn (1964) that the ground state properties of an electron gas, which are assumed non-degenerate, are system-independent functionals of the electron density. Hohenberg and Kohn also observed that the total ground state energy functional, $E_{|\rho(r)|}$, corresponds to a minimum for the true electron density and hence a variational approach can be adopted in the formulism (i.e. in the spirit of the self-consistent Hartree method). Writing $E_{|\rho(r)|}$ as a sum of the kinetic, $E^{K.E.}_{|\rho(r)|}$, and Hartree energies, $E^{H}_{|\rho(r)|}$ (i.e. that due to the electrostatic interaction between the conduction electrons and the conduction electrons and the core), plus whatever is left gives ;

$$E_{|\rho(r)|} = E^{K.E.}_{|\rho(r)|} + E^{H}_{|\rho(r)|} + E^{XC}_{|\rho(r)|} \tag{6.3}$$

where $E^{XC}_{|\rho(r)|}$ is, by definition, the exchange and correlation energy of an interacting electronic system of density $\rho(r)$. Minimisation of $E_{|\rho(r)|}$ with respect to the charge density leads to the self-consistent one-electron Kohn-Sham equations (see Kohn and Sham, 1965) i.e. ;

$$\left(-\nabla^2 + V^{H}_{|\rho(r)|}(r) + V^{XC}_{|\rho(r)|}(r)\right)\psi_i(r) = \epsilon_i\psi_i(r) \tag{6.4}$$

subject to

$$\rho(r) = \sum_{i=1}^{N} |\psi_i(r)|^2 \qquad (6.5) \qquad \text{and} \qquad \int \rho(r)d^3r = N \tag{6.6}$$

where

$$V^{H}_{|\rho(r)|} = V(r) + \frac{1}{2}\int \frac{\rho(r')}{|r - r'|}dr' \tag{6.7}$$

$V(r)$ is the predescribed external lattice potential [i.e. not a functional of $\rho(r)$], the integral in eq. 6.7 is the classical Hartree potential and $V^{XC}_{\rho(r)}$ is the exchange and correlation potential. The constraints given by equations 6.5 and 6.6 ensure the orthogonalisation of the one-electron functions and conserve the number of particles. The effective potential corresponding to a total energy $E_{\rho(r)}$, therefore, may be written as :

$$V^{eff}_{\rho(r)} = V^{N}_{\rho(r)} + V^{XC}_{\rho(r)} \qquad (6.8)$$

and is determined simultaneously with the one-electron functions $\{\psi_i(r)\}$ by iteration of the Kohn-Sham equations. From the minimisation procedure $V^{XC}_{\rho(r)}(r)$ corresponds to the functional derivative of the exchange energy i.e. ;

$$V^{XC}_{\rho(r)} = \frac{\delta E^{XC}_{\rho(r)}}{\delta \rho(r)} \qquad (6.9)$$

Consequently the exchange-correlation term in eqns. 6.4 can be fully described from a knowledge of the total exchange-correlation energy. The determination of this energy is the subject of the following section.

6.2.1. The Local Density Approximation

The solutions to the Kohn-Sham equations are exact in that they yield the true ground state charge density and total energy of the electron distribution. The residual problem with DFT, however, is that the total exchange and correlation energy is not explicitly known and must therefore be approximated. This model dependent quantity is the only approximation made in the Kohn-Sham formulism and its applicability is central to the development of DFT.

Approximations to $E^{XC}_{\rho(r)}$ are usually made within the local density approximation (LDA) such that ;

$$E^{XC}_{\rho(r)} = \int \epsilon^{h}_{\rho} \rho(r) dr \qquad (6.10)$$

where ϵ^{h}_{ρ} is the contribution of exchange and correlation to the total energy per particle in a homogeneous, interacting electron gas of constant density ρ_o.

The LDA assumes $E^{XC}_{[\rho(r)]}$ consists of a sum of the individual contributions, ϵ^h_{ρ}, over the spatial extent of the inhomogeneous gas and determines each one by treating the distribution as if it were locally uniform. To calculate these contributions it is convenient to parameterise the electron density such that ;

$$\rho_o = \frac{3}{4\pi r_s^3} \qquad (6.11)$$

where r_s is the mean electron radius (i.e. the Wigner radius) and uniquely determines the properties of the homogeneous electron gas. An analytic fit to the exchange and correlation energy, observing that $\epsilon^h_{\rho_o}$ assumes its maximum value in the low density limit, has been made by Gunnarson and Lundqvist (1976). This fit is determined uniquely by r_s, which is consistent with the development of DFT, and has been applied successfully to a variety of electron distributions (see Lundqvist and March, 1983).

Within the LDA the solutions to the Kohn-Sham equations would be exact if applied to a uniform electron gas assuming that $\epsilon^h_{\rho_o}$ can be deduced. In practice, therefore, the applicability of the LDA to real systems appears to be confined to distributions where the electron density is relatively slowly varying (i.e. those in which the range of $V^{XC}_{[\rho(r)]}$ is small compared to r_s). The local approximation, however, has been found to accurately represent electron distributions where $\rho(r)$ varies rapidly (such as over the region of an atomic core). This can be explained with the observation of Lundqvist and March (1983) who identified the contribution of exchange to the total energy of an electronic system to be, in general, dominant over that of correlation. Since the same authors also showed that the range of the exchange-correlation hole calculated via the LDA is similar to its true value, therefore, the exchange-correlation energy is relatively insensitive to variations in charge density.

The most important feature of the local density approximation in DFT with regard to momentum density studies is that the effects of exchange and correlation on the Compton profile may be described by a correction term which may be simply added to the

results of a given band calculation provided the local potential is known.

6.2.2. The Lam-Platzman Correction

The solutions to the Kohn-Sham equations do not yield the true one-electron wavefunctions because the minimisation procedure in the Hohenberg-Kohn formulation only formally defines the ground state properties of an electronic distribution. An understanding of how these "pseudo-wavefunctions" yield the true electron density may be gleaned from the fact that there exist an infinite number of basis function sets that correspond to a particular $\rho(r)$. If deduction of an accurate charge density, therefore, is the object of the study, any one of these basis sets will produce the desired result. The procedure for the deduction of the ground state momentum density from the Kohn-Sham solutions, however, is not so straight forward. For non-interacting or interacting electron distributions in the Hartree or Hartree-Fock approximations, respectively, it can be shown that (see Lundqvist and March, 1983) ;

$$N(p) = \sum_{i=1}^{N} | <p | \chi_i(p)> |^2 \qquad (6.12)$$

where $\chi_i(p)$ are the Fourier transforms of the real space one-electron wavefunctions. By application of Feynman's theorem, Lam and Platzman (1974) showed that for the transformed solutions to the Kohn-Sham equations, $\chi_i'(p)$, eq. 6.12 becomes modified by the addition of an extra term i.e. ;

$$N^{DFT}_{|\rho(r)|}(p) = \sum_{i=1}^{N} | <p | \chi_i'(p)> |^2 + \frac{\delta E^{XC}_{|\rho(r)|}}{\delta \epsilon_p} \qquad (6.13)$$

where the correction term is given by the derivative of the total exchange-correlation energy with respect to the individual electron energies arising from correlations between the states $| \chi_i'(p) >$. In the LDA (i.e. eq. 6.10) this term becomes ;

$$\frac{\delta E^{LDA}_{|\rho(r)|}}{\delta \epsilon_p} = \int \frac{\delta \epsilon^h_p}{\delta \epsilon_p} \rho(r)\, dr$$

for which Lam and Platzman proposed the following ansatz ;

$$\frac{\delta E^{LDA}_{|\rho(r)|}}{\delta q_p} = \int_{\text{unit cell}} \left[N^h_{|\rho(r)|}(p) - N^f_{|\rho(r)|}(p) \right] \rho(r)\, dr \qquad (6.14)$$

where the bracketed term represents the difference between the homogeneous, interacting and free electron gas momentum densities, defined by the local potential $\rho(r)$. Both $N^h_{|\rho(r)|}$ and $N^f_{|\rho(r)|}$ are necessarily normalised to one electron. For a one dimensional momentum distribution (i.e. the Compton profile) eq. 6.14 reduces to ;

$$\Delta J^{LDA}_{|\rho(r)|}(q) = \int_{\text{unit cell}} \rho(r) \left[J^h_{|\rho(r)|}(q) - J^f_{|\rho(r)|}(q) \right] d^3r \qquad (6.15)$$

This is the Lam-Platzman correction term which describes the effect of exchange and correlation on the Compton profile. Furthermore, since it is modelled within the LDA, it is necessarily isotropic. For Compton profiles calculated from the set $\{\chi_i'(p)\}$, this correction describes the adjustment necessary for the physical interpretation of the momentum distribution within the LDA, provided the charge density employed is common to both terms in eq. 6.13.

The results of the Lam-Platzman correction when applied to band calculations of several transition metal elements and its effect on the agreement between theory and experiment are described in the following sections. In addition the details of the calculation are outlined and the results are compared with an existing attempt to include the effects of exchange and correlation in theoretical Compton profiles.

6.3. Calculation of the Lam-Platzman Correction

As outlined in chapter 2, the effect of exchange and correlation on the momentum density is to promote electrons from states within the Fermi sphere to states of higher momentum and so distort the parabolic dependence of $J(p_z)$ on p_z which is characteristic of a free electron gas. The difference between the correlated and free electron profiles is the basis of the exchange and correlation correction applied to theoretical data as described by eq. 6.15. Within the bounds of the LDA the accuracy of the Lam-Platzman

correction is uniquely determined by this difference. Its influence on the form of $\Delta J^{LDA}_{|\nabla\rho|}$ is described below.

6.3.1. Analysis of the Momentum Density

Accurate determination of the momentum space occupation numbers corresponding to the quasi-particle properties of a homogeneous, interacting electron gas requires the evaluation of the electron self-energy as a function of wavevector (see Lundqvist,1968). From this the single particle spectral weight function, commonly used to describe the plasmon spectra of an electron gas (see Lundqvist, 1967 a, b), can be obtained and integrated with respect to energy to yield N(k). This calculation is greatly simplified by the assumption of the random phase approximation (RPA), in which each Fourier component of the effective potential can be treated independently - see Lundqvist, 1968. It is difficult to identify the extent to which two existing calculations of the momentum density of a homogeneous interacting electron gas agree since only graphical data is available in each case (see Daniel and Vosko, 1960, and Lundqvist, 1968). Comparison is further hindered by the different units, and hence different parameters, employed to characterise the electron gas in each calculation. Taking these difficulties into account the two calculations appear to differ by up to ~ 3.5 % at the extremes of N(p) (i.e. at p/p_f = 0 and ~ 1.4) although good agreement is observed at $p \simeq p_f$. Bauer and Schneider (1983a), however, have pointed out that the Lundqvist occupation numbers are the more reliable of the two since those of Daniel and Vosko are calculated only to first order in the Hamiltonian. Consequently only the results at $p \simeq p_f$ in the latter calculation are used in the momentum density model presented here.

6.3.1.1. Momentum Density Model

An analytic fit to the results of Lundqvist (1968) has been made in preference to interpolating graphical data. The advantage of this method over that of interpolated data is that the conduction electron contribution to $\Delta J^{LDA}_{|\nabla\rho|}$ can be calculated directly for any value of r_s. Assuming that the electrons occupy a Fermi distribution, Daniel and Vosko

found that for values of $p/p_f = 1$ the momentum density can be represented by :

$$\lim_{p_f \to p} N^+(1) = 1.7\alpha_{r_s} \quad \text{and} \quad \lim_{p_f \to p} N^-(1) = 1 - 1.7\alpha_{r_s} \tag{6.16}$$

where, in a.u. :

$$\alpha_{r_s} = \frac{1}{\pi^2 k_f} \tag{6.17}$$

and

$$k_f = \left(\frac{9\pi}{4}\right)^{1/3} \frac{1}{r_s} \tag{6.18}$$

The first analytic fit to $J^h_{|\mathbf{q}(\sigma)|} - J^f_{|\mathbf{q}(\sigma)|}$ was made by Rennert (1981) who also observed the boundary conditions imposed by eqns. 6.16. Figure 6.1(a) illustrates the results of this model for r_s values of 2,4 and 6 which are inadequate for two reasons. Firstly, and most significantly, this fit assumes erroneously that $N(0) = 1$ for all charge densities, not merely in the high density limit, and secondly that the upper bound of the distribution is fixed at $p/p_f = 1.476$. The former of these limitations introduces errors of the order of 0.5 %N(0) at $p = 0$ and p_f to the momentum density compared to that obtained by Lundqvist and subsequently the Rennert fit has been modified according to the following equations ;

$$N(p) = 1 - a_{p_s} p^2 - \delta(1 - p) \qquad \text{for } p < p_f$$

$$= \frac{a_{p_s}(b_{p_s} - p)^2}{(b_{p_s} - 1)^2} \qquad \text{for } p > p_f \tag{6.19}$$

where

$$a_{p_s} = 1.7\alpha_{r_s} = \frac{1.7}{\pi^2 k_f} \tag{6.20}$$

b_{p_s} is the upper bound of the distribution, determined by the following normalisation condition ;

$$\int N(p)\, d^3p = \frac{4\pi}{3} p_f^3 \tag{6.21}$$

δ corresponds to N(0) (i.e. the deviation of the momentum density from unity) for non-zero values of r_s and is obtained from the Lundqvist data. Together a_{p_s}, b_{p_s} and δ

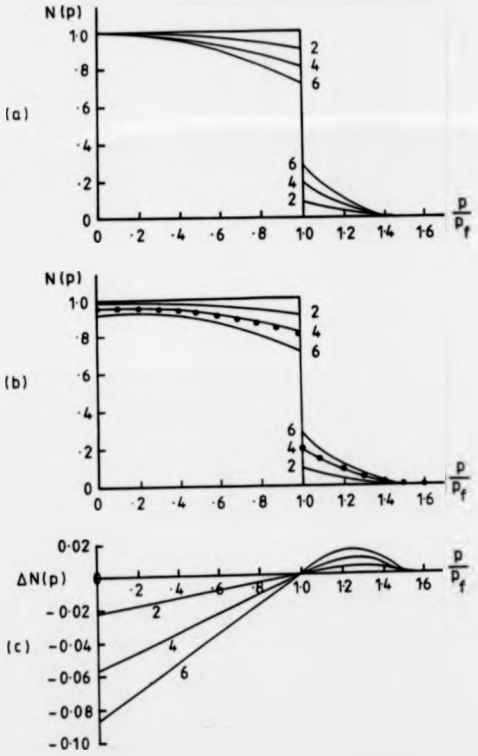

Figure 8.1 The momentum density in units of p/p_f calculated for $r_s = 2$, 4 and 6 from (a) the Rennert analytic fit (see Rennert et al. 1981) and (b) the modified fit described in the text. (c) shows the difference (b) - (a). The dots in (b) correspond to $N(p)$ for $r_s = 4$ and are derived from the full self-energy calculation of Lundqvist (1968).

completely characterise the momentum distribution with the former two being functionals of the charge density. The values of a_{r_s}, b_{r_s}, δ and p_f ($=k_f$ in a.u.) for the first six integral values of r_s expressed as a ratio to the first Bohr orbit (i.e. 0.53 a.u.) are presented in table 6.1. The corresponding momentum densities for r_s = 2, 4 and 6 are plotted in figure 6.1(b). The dots represent the Lundqvist data for r_s = 4 and are in good agreement with the modelled distribution. Figure 6.1(c) shows the difference between the momentum densities derived from the present model and those calculated by Rennert for r_s values of 2,4, and 6. From this data it is apparent that the Rennert fit overestimates N(p) by up to 9% at the origin (i.e. for r_s = 6) which is clearly unrepresentative of the Lundqvist occupation numbers.

The input data for the Lam-Platzman correction was obtained by subtracting the free electron Compton profile from that derived from eqns. 6.19 (i.e. according to eq. 2.8). Since both the interacting and free electron Compton profiles were normalised to unity the resulting difference data had zero area in all calculations.

6.3.1.2. Input Parameters

The input parameters required to calculate the Lam-Platzman correction for a real metal are ;

(a) N_{ins}, the number of interstitial electrons per atom

(b) R_{MT}, the radius of the muffin-tin potential

(c) a_0, the lattice parameter,

all of which are taken from the tabulated data of Moruzzi, Janak and Williams (1978). For cubic structures the volume occupied by the conduction electrons per unit cell, V_{ins}, is deduced from a_0. The conduction electron density is then given by ;

$$\rho_0 = \frac{N_{ins}}{V_{ins}} \quad \text{with} \quad k_f = (3\pi^2\rho_0) \tag{6.22}$$

r_s is obtained by rearranging eq. 6.11.

r_s	r_s (a.u.)	p_f (a.u.)	w_0	A	b_p (p/p_f)
1.0	0.53	1.9192	0.0280	0.0110	1.5128
2.0	1.06	0.9596	0.0560	0.0220	1.5128
3.0	1.59	0.6397	0.0839	0.0390	1.5194
4.0	2.12	0.4798	0.1119	0.0560	1.5227
5.0	2.65	0.3838	0.1399	0.0720	1.5240
6.0	3.18	0.3199	0.1679	0.0864	1.5240

Table 6.1 Characteristic parameters of the momentum density for varying amounts of correlation. r_s, calculated analytically with the delta approximation. The point at which the distribution intersects the p_z axis, b_p, is dependent on the degree of correlation and is predominantly greater than that calculated by Rennert (1981) which is fixed at 1.4760.

To calculate the contribution to $\Delta J^{LDA}_{|\rho(r)|}$ from the core electrons the local charge density within the muffin-tin sphere (assumed spherically symmetric) is required. Again this is taken from Moruzzi et al and is illustrated in figure 6.2 for six metal elements. Since both core and conduction electron densities are deduced from the DFT calculation of Moruzzi et al, the total integrated charge distribution is necessarily equal to the atomic number of the respective element.

6.3.1.3. The Lam-Platzman Algorithm

The algorithm for calculating the Lam-Platzman correction is shown in figure 6.3 and was executed on an IBM 370 mainframe computer. From this figure it can be seen that the core and conduction electron contributions to $\Delta J^{LDA}_{|\rho(r)|}$ are calculated independently of one another and then superimposed to form a composite correction.

To simplify the calculation over the muffin-tin region, the contribution to the correction from each point δr in the core charge density is obtained by interpolating between r_s^{max} and 0 (i.e. the free electron limit). Hence the input $J^h_{|\rho(r)|}(q) - J^f_{|\rho(r)|}(q)$ appropriate to the core electron distribution has to be calculated for the radial point of least density (i.e. at which the effects of exchange and correlation are the most significant). The determination of r_s^{max}, therefore, forms the basis of the core contribution to $\Delta J^{LDA}_{|\rho(r)|}$.

The conduction electron contribution to the Lam-Platzman correction is somewhat simpler to calculate since the interstitial charge density is assumed constant. Consequently the input for the difference profile does not vary with r and can be deduced for the exact conduction electron charge density, ρ_0.

For each calculation of the Lam-Platzman term, therefore, two input files for $J^h_{|\rho(r)|} - J^f_{|\rho(r)|}$ are required, along with the input parameters described in section 6.3.1.2 and the local charge density. The area of the total correction is necessarily zero and is checked to ensure that the calculation has been performed correctly.

In total two programs are used to calculate $\Delta J^{LDA}_{|\rho(r)|}$, each greater than 500 lines in length. The first prepares the input files, $J^h_{|\rho(r)|} - J^f_{|\rho(r)|}$, for the core and conduction

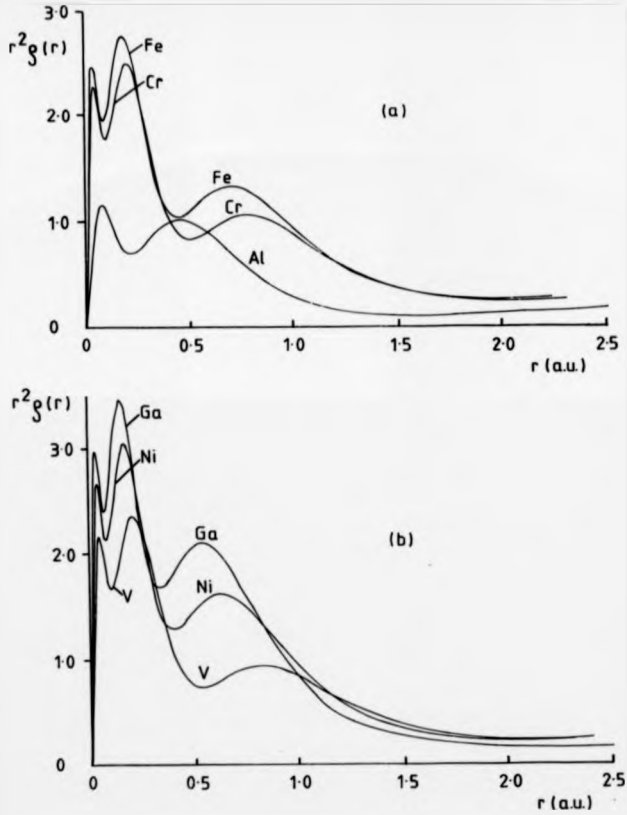

Figure 6.2 The (local) radial charge densities of (a) Ga, Ni and V and (b) Al, Cr and Fe as tabulated by Moruzzi et al (1978).

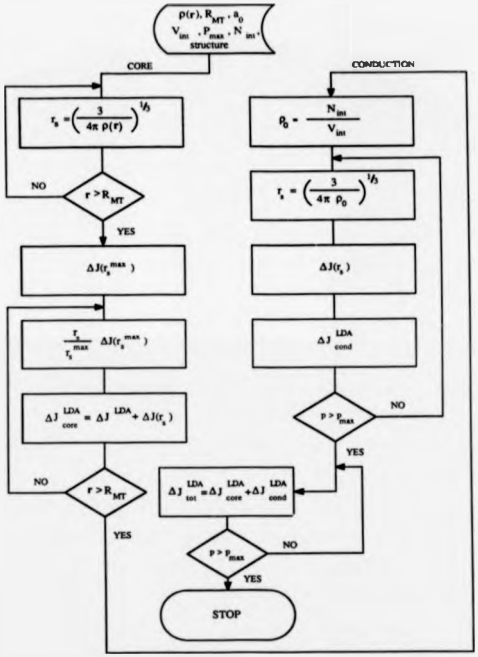

Figure 6.3 The algorithm for calculating the Lam-Platzman correction. The symbols are defined in the text.

electron regions and the second performs the integration defined by eq. 6.15. The results of this calculation for three transition metal elements are presented in the following sections.

6.4. Results and Discussion

6.4.1. Form of Correction

The input parameters for the Lam-Platzman correction of Al, V, Cr, Fe, Ni and Ni_3Ga are given in table 6.2. The results of the calculations based on these data are listed in table 6.3. The form of the correction in each case consists of a negative region in the vicinity of the origin, a sharp peak at approximately the Fermi momentum of the conduction electron gas and a high momentum tail. It can be seen from figure 4.4, which compares the input profile difference with the Lam-Platzman correction for aluminium, that the shape of $\Delta J^{LDA}_{|p(r)|}$ is similar to $J^{h}_{|p(r)|} - J^{f}_{|p(r)|}$ but is of greater magnitude at all points of the distribution. This is because the input difference is normalised to one electron and becomes magnified when integrated over the unit cell. The high momentum tail is exclusively a feature of the core electron distribution and arises as a consequence of the large Fermi momentum associated with the charge density at low r.

Since the Lam-Platzman correction is the sum of the core and conduction electron contributions, it is difficult to identify a general trend in the above features by reference to a specific input parameter. It is apparent, however, that the magnitude of $\Delta J^{LDA}_{|p(r)|}$ at the origin is inversely proportional to the average charge density of the core. For metals such as aluminium and gallium, therefore, where the core charge density at high r is relatively low (see figure 6.2), the resultant correction exhibits a large dip at the origin which is consistent with the assumption of high exchange and correlation effects with low electron densities.

The conduction electron contribution to $\Delta J^{LDA}_{|p(r)|}$ varies typically from $\sim$ 25 % at the origin to $\sim$ 40 % at $p \approx p_f$. This is because a unique Fermi momentum is associated with the conduction electron gas (of assumed constant charge density) which gives rise to a

Subject	Z	Structure	a_0 (a.u.)	r_s (a.u.)	p_f (a.u.)	Interstitial Electrons per atom	Muffin Tin Radius (a.u.)
Aluminium	13	f.c.c.	7.60	2.11	0.9063	0.716	2.687
Vanadium	23	b.c.c.	5.54	1.80	1.0640	1.106	1.959
Chromium	24	b.c.c.	5.30	1.71	1.1214	1.134	1.874
Iron	26	b.c.c.	5.15	1.71	1.1227	1.044	1.821
Nickel	28	f.c.c.	6.55	1.83	1.0511	0.715	2.316
Gallium	31	f.c.c.	7.83	2.28	0.8434	0.631	2.768
Ni_3Ga	115	f.c.c.	7.19	2.02	0.9480	0.694	2.542

Table 6.2 Input parameters for the Lam-Platzman correction for the elements and compound shown.

p_z (a.u.)	Al	V	Cr	Fe	Ni	Ga	Ni_3Ga
0.0	-0.098	-0.084	-0.074	-0.070	-0.075	-0.128	-0.098
0.1	-0.098	-0.084	-0.074	-0.070	-0.075	-0.127	-0.097
0.2	-0.096	-0.083	-0.073	-0.069	-0.074	-0.125	-0.096
0.3	-0.091	-0.081	-0.071	-0.068	-0.072	-0.119	-0.092
0.4	-0.083	-0.077	-0.069	-0.065	-0.069	-0.110	-0.088
0.5	-0.069	-0.071	-0.064	-0.061	-0.065	-0.093	-0.079
0.6	-0.047	-0.062	-0.058	-0.056	-0.057	-0.065	-0.066
0.7	-0.013	-0.048	-0.048	-0.047	-0.046	-0.023	-0.045
0.8	0.038	-0.029	-0.034	-0.035	-0.0 31	0.039	-0.016
0.9	0.110	-0.001	-0.015	-0.017	-0.0 09	0.086	0.026
1.0	0.111	0.037	0.012	0.006	0.020	0.067	0.042
1.1	0.080	0.067	0.046	0.047	0.043	0.032	0.040
1.2	0.025	0.048	0.053	0.046	0.037	0.017	0.030
1.3	0.006	0.030	0.038	0.034	0.024	0.010	0.019
1.4	0.002	0.018	0.024	0.022	0.015	0.006	0.013
1.5	0.001	0.011	0.015	0.014	0.009	0.003	0.008
1.6	0.000	0.009	0.010	0.009	0.006	0.002	0.006
1.8	0.001	0.008	0.008	0.008	0.005	0.001	0.004
2.0	0.001	0.009	0.007	0.006	0.005	0.002	0.004
2.5	0.003	0.011	0.009	0.007	0.005	0.003	0.005
3.0	0.004	0.012	0.010	0.008	0.006	0.004	0.006
3.5	0.004	0.011	0.010	0.009	0.007	0.008	0.008
4.0	0.004	0.007	0.009	0.008	0.008	0.007	0.008
5.0	0.004	0.002	0.003	0.006	0.007	0.008	0.008
6.0	0.003	0.001	0.001	0.002	0.004	0.007	0.005
7.0	0.001	0.001	0.001	0.001	0.001	0.004	0.002
10.0	0.000	0.001	0.001	0.001	0.001	0.001	0.001

Table 6.3 The unconvoluted Lam-Platzman correction for aluminium, vanadium, chromium, iron, nickel and gallium. Ni_3Ga is the subject of a current investigation, hence its inclusion in this table.

strong positive peak at $p = p_f$. The core charge density, on the other hand, varies over the muffin-tin region with successive points in r space corresponding to different values of Fermi momenta. The latter contribution to the composite correction, therefore, is a broad, positive peak in the vicinity of p_f. In essence the high and low momentum features of the Lam-Platzman correction are dominated by the core charge density whereas the intermediate form of $\Delta J^{LDA}_{|\rho(r)|}$ is determined to a greater extent by the distribution of the conduction electrons.

6.4.2. Comparison with Previous Calculations

The application of the Lam-Platzman correction to the results of DFT calculations (i.e. by the addition of $\Delta J^{LDA}_{|\rho(r)|}$ to the theoretical Compton profile) always results in a shift of electron density from low to high momenta. The extent of this shift reflects the degree to which the core and conduction electrons are correlated. In addition to the results presented here, this has also been observed in a study of copper by Bauer and Schneider (1983b) and in a study of nickel by Rollason et al (1987) which used a program written by Bauer to calculate $\Delta J^{LDA}_{|\rho(r)|}$.

These earlier calculations of the Lam-Platzman term are less accurate than the results presented here. This is because the authors calculated the correction term from a *single* input for $J^{h}_{|\rho(r)|} - J^{f}_{|\rho(r)|}$ corresponding to the Lundqvist occupation numbers for $r_s = 2$. Subsequent interpolation of this data for $2 < r_s < 0$ over both the core and conduction electron regions introduces discrepancies to the calculation. Consequently a difference of $\sim$ 0.3 %J(0) at the origin and $\sim$ 0.2 %J(0) at $p \sim 1$ a.u. for the nickel correction is observed between the present Lam-Platzman correction and that derived by Rollason et al. At the other points in $\Delta J^{LDA}_{|\rho(r)|}$, however, good agreement is observed between the two calculations.

The earlier calculation is further limited to charge densities characterised by values of r_s less than 2. Bauer's program, for example, could not be used to calculate the Lam-Platzman corrections of aluminium, gallium or Ni_3Ga presented in table 6.3 without extra-

polation of the input data over both core and conduction electron regions. In general, therefore, the current work extends that of Bauer and co workers to enable $\Delta J^{LDA}_{|\vec{u}(\vec{r})|}$ to be calculated for all metallic solids.

6.4.3. Corrected Datasets

Figure 6.4 shows the difference between theory and experiment for the nearest neighbour directional Compton profiles of (a) iron (see Rollason et al, 1993,a), (b) vanadium (see Rollason et al, 1993,b) and nickel (see Rollason et al, 1987). The appropriate Lam-Platzman correction convoluted with a Gaussian of FWHM 0.4 a.u. and with a change of sign is denoted in each case by the solid line. The data are presented in this way for ease of comparison and should be subtracted from the difference curves. As with aluminium (see figure 4.9), the correction has not been directly applied since the potential employed in its construction is not identical to that used in either band calculation. Despite the recurrent problem of a deficiency in electron density, application of $\Delta J^{LDA}_{|\vec{u}(\vec{r})|}$ to the APW calculation for iron (see Wakoh and Kubo, 1977) and vanadium (see Wakoh et al, 1976) results in improved agreement between theory and experiment. This is consistent with the observations made for aluminium and chromium described in chapters 4 and 5, respectively.

Although application of the correction to the LCAO calculation for iron (see Rath et al, 1973) for some unknown reason reduces the agreement between theory and experiment, a significant improvement is observed for the LCAO profiles of vanadium (see Laurent, Wang and Callaway, 1978) and nickel (see Wang and Callaway, 1975). It may be concluded, therefore, that the LCAO and APW band calculations consistently underestimate the degree of exchange and correlation present in metals. Although this discrepancy may be partially resolved for momentum values in the first Brillouin zone (i.e. $0 < p_z < 1$ a.u.) by application of the Lam-Platzman correction, the difference datasets of Cr, Fe, Ni and V still exhibit residual oscillations at high momenta after $\Delta J^{LDA}_{|\vec{u}(\vec{r})|}$ has been added to the theoretical Compton profiles. These oscillations cannot be attributed to the assumption of

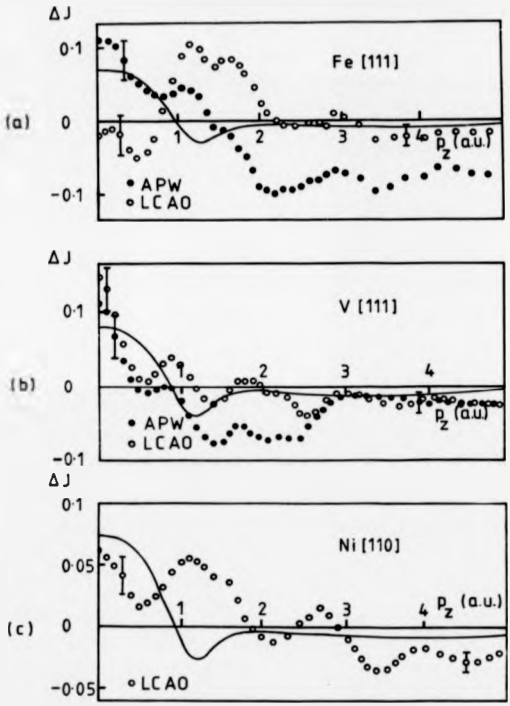

Figure 6.4 Theory - experiment for the nearest neighbour Compton profiles of (a) iron (see Rollason et al. 1983, a), (b) vanadium (see Rollason et al. 1983, b) and nickel (see Rollason et al. 1987). In each case the solid and open circles dots correspond to the results of APW and LCAO calculations, respectively. The solid line represents the Lam-Platzman correction convoluted with a Gaussian of FWHM 0.4 a.u. and should be subtracted from the difference data.

the wrong lattice potential in the respective band calculations since any change in $V^{ion}(r)$ would only influence $U_k(r)$ in the Bloch representation given by eq. 2.24. This would merely redistribute the electrons between the occupied Fermi spheres rather than transfer electron density to the interstitial region as would be required to observe complete agreement between theory and experiment. A method of describing the high momentum behaviour of the exchange and correlation correction is discussed below.

6.4.4. Directional Considerations

The failure of the LDA to describe the high momentum oscillations present in the transition metal difference profiles is a consequence of the assumption of a homogeneous electron distribution at each point in the charge density (see Eisenberger, Lam, Platzman and Schmidt, 1972). Since the lattice potential effectively promotes electrons from the main Fermi surface to those of higher order outside the first Brillouin zone (see section 2.5.3), the effects of exchange and correlation must be represented in the input to the Lam-Platzman correction for all secondary Fermi distributions in addition to that localised at the origin of momentum space. By introducing the effects of inhomogeneities in the conduction electron profile, therefore, $\Delta J^{LDA}_{n(r)}$ becomes dependent on the reciprocal plane spacing normal to the direction of interest and has to be calculated independently for each directional profile. In band calculations this is far from trivial since the lattice effects have to be incorporated, in some way, in the exchange-correlation potential. It is possible, however, to investigate the effects of band structure on the conduction electron contribution to the correction in a qualitative way.

Figure 6.5(a) shows the inhomogeneous electron gas profile (solid line) taking the secondary Fermi distributions into account for $r_s = 2$ along a general reciprocal lattice vector [hkl] (the Compton profiles corresponding to the homogeneous, free electron gas at each reciprocal lattice point are denoted by the dashed lines). The separation between consecutive maxima, d, is given by :

$$d = \frac{a_0}{(h^2 + k^2 + l^2)^{\frac{1}{2}}} \qquad (6.23)$$

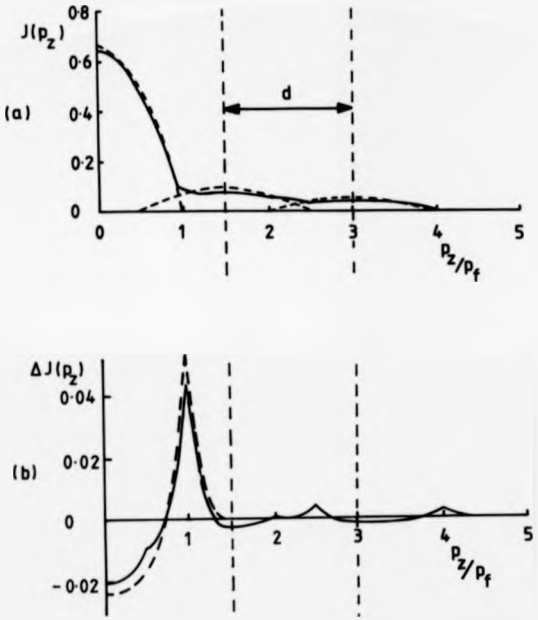

Figure 8.5 (a) Free (dashed lines) and interacting (solid lines) electron gas Compton profiles calculated for $r_s = 2$ and (b) the exchange and correlation correction obtained from the difference between the curves given in (a). The secondary Fermi surfaces are indicated by the vertical dashed lines.

where a_0^* is the reciprocal lattice parameter $\left(= \frac{2\pi}{a_0}\right)$. The weighting of each secondary distribution is given by the square of the appropriate Fourier coefficient, $a_G(k)$, as defined by eq. 2.25 which describes the extent to which the lattice potential smears out the momentum density. The data shown in figure 6.5(a) assumes Fourier coefficients of 0.85, 0.10 and 0.05 for the first three Fermi surfaces. Since the integral of $J(p_z)$ over the whole of momentum space is conserved, the Compton profile corresponding to the main Fermi distribution is reduced in magnitude with density being transferred to the higher order states.

For the case of aluminium, where the higher order surfaces account for ~ 10 % of the total conduction electron density (see Mader et al, 1976), the shift in density to the higher order states corresponds to a decrease in $\Delta J^{LDA}_{|n|>1}$ of ~ 0.002 a.u. per electron at the origin [i.e. ~ 0.05 %J(0)]. Since this is an order of magnitude less than experimental error, then the inclusion of band structure effects does not significantly alter the agreement between theory and experiment in the first Brillouin zone. This observation is true for all the theoretical profiles presented here.

When multiplied by the charge density and integrated over all r, in the spirit of the Lam-Platzman correction, the exchange-correlation correction for the conduction electron gas consists of a superposition of identical functions, each displaced from its neighbour by d a.u. and weighted according to its Fourier coefficient. The characteristic form of the resultant anisotropic correction calculated from an input given by the difference between the solid and dashed curves in figure 6.5(a) is illustrated in figure 6.5(b). This correction has been calculated for a b.c.c. lattice with the lattice parameter of chromium and should be added to an (isotropic) core contribution before application to the results of DFT. When this superposition is made the first negative peak in the composite lineshape will be typically 4 times larger than that shown in figure 6.5(b) since the latter contribution dominates at low momenta (see section 6.4.1). Furthermore, since the core electrons only contribute to the correction in the first Brillouin zone (i.e. the momentum density of the core

is independent of lattice effects), the resultant correction will be most significant in the vicinity of the origin. This is observed in the transition metal difference profiles given in figures 5.5 and 6.4.

The form of $\Delta J_{|\alpha\rangle|}^{INHOM}$ shown in figure 6.5(b) is characteristic of the contribution of exchange and correlation to the Compton profile. Strictly speaking, however, it does not represent the Lam-Platzman correction for a conduction electron gas characterised by $r_s = 2$ since it does not satisfy eq. 6.14. It must be emphasised, therefore, that although the treatment of exchange and correlation effects in this way yields a more representative theoretical Compton profile, it only provides a qualitative description of the high order oscillations in the theory - experiment difference data in the absence of an accurate model for N(p).

CHAPTER 7

THE MAGNETIC COMPTON PROFILES OF IRON AND NICKEL

7.1. Introduction

The study of momentum density in chapters 1 to 5 involved measurement of the inelastic scattering cross-section of unpolarised photons by electrons. It was outlined in section 1.4.1, however, that in the differential cross-section there is a term which depends on the coupling between circularly polarised radiation and unpaired electrons (eq. 1.30) so that the total double differential cross-section for right-hand polarised radiation can be written as ;

$$\frac{d^2\sigma}{d\omega d\Omega} = \left(\frac{e^2}{m_0c^2}\right)^2 \left(\frac{\omega_2}{\omega_1}\right) \left[(1 + \cos^2\theta)J(p_z) \pm \frac{4\hbar\omega_1}{m_0c^2}\cos\theta(\cos\theta - 1)\, J_{mag}(p_z)\right] \quad (7.1)$$

for electrons with spin aligned parallel (+) and antiparallel (-) to the photon beam. Consequently the modified cross-section enables the inelastically scattered intensity from electrons with aligned, unpaired spins, such as those present in ferromagnets, to be isolated from the total cross-section. This is achieved by subtracting out the much larger non-magnetic scattering contribution in a difference experiment from which the spin-dependent, or magnetic, Compton profile, $J_{mag}(p_z)$, may be obtained. $J_{mag}(p_z)$ is defined in terms of the momentum densities for electrons aligned parallel (spin-up) and antiparallel (spin-down) to the sample magnetic field such that ;

$$J_{mag}(p_z) = \int_{p_x}\int_{p_y}\sum_i \left[n_i(p) - n_i(p)\right] dp_x dp_y \quad (7.2)$$

where $n_i(\mathbf{p})$ is the momentum density of the i^{th} occupied band. $J_{mag}(p_z)$, therefore, may be extracted from the difference spectrum via the following equation :

$$\Delta\frac{d^2\sigma}{d\omega d\Omega} = \left[\frac{d^2\sigma}{d\omega d\Omega}\right]_{up} - \left[\frac{d^2\sigma}{d\omega d\Omega}\right]_{down}$$

$$= \left[\frac{e^2}{m_0c^2}\right]^2 2P_c\sigma.(k_i\cos\theta - k_f)\, J_{mag}(p_z) \qquad (7.3)$$

where the degree of circular polarisation, P_c, is +1 for left-handed polarised photons and -1 for right-hand polarised photons. σ is the electron spin vector. It is apparent from eq. 7.1 that the ratio of the magnetic to the non-magnetic cross-sections is proportional to the incident photon energy and has a strong dependence on scattering angle, as illustrated by figure 1.4 (a). To accurately determine the magnetic Compton profile, therefore, the source of circularly polarised radiation should be of high energy and intensity and should be oriented at -180° to the detector (for which $\frac{d\sigma_s}{d\sigma_m}$ assumes its maximum value).

7.1.1. Origin of the Magnetic Compton Profile

The spherically averaged magnetic Compton profiles of (a) iron and (b) nickel are described by the solid lines in figure 7.1. These profiles were calculated by the APW (see Wakoh and Kubo, 1977) and OPW (see Rennert, Carl and Hergert, 1983) methods respectively and represent the only theoretical spin-dependent momentum densities currently available. Both exhibit more structure than the total profile because of the major cancellation of the spin-paired contributions. The individual s, s + p and s/p hybrid magnetic profiles are indicated by the dashed, dotted and dash/dotted lines in this figure, respectively. The origin of these individual contributions, which superimpose to produce a characteristic "volcano" structure, can be understood by considering the mechanism of the ferromagnetic interaction.

Ferromagnetic behaviour arises as a consequence of the exchange interaction between

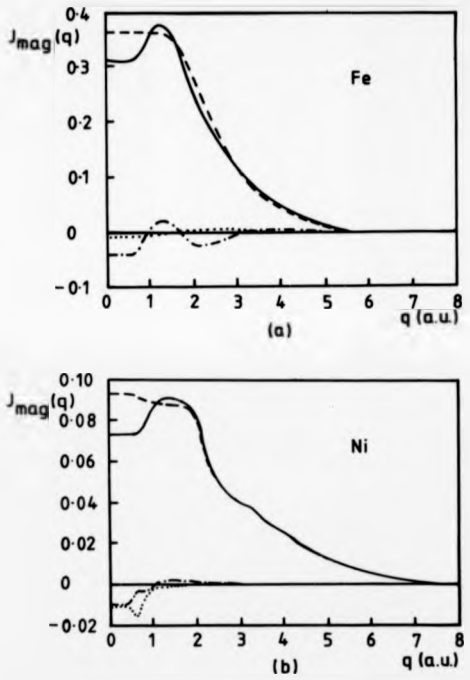

Figure 7.1 The partial contributions to the magnetic Compton profiles of (a) iron (see Wakoh and Kubo, 1977) and (b) nickel (see Rennert et al. 1983) from the 3d (dashed lines), core (dotted lines) and s/p hybrid electrons (dot/dashed lines). In both cases the total distribution is indicated by the solid curve.

electron spins on neighbouring atoms (see section 6.1.1.1) for temperatures below the Curie point which splits the spin up and spin down hybrid states according to the degree of overlap between the individual electron wavefunctions. If the exchange field is sufficiently strong to lift one spin sub-band above the Fermi energy (conventionally described as the spin up band) then the electron distribution will exhibit a net magnetic moment per atom due to the incomplete occupancy of states within that band. Since the majority of the conduction electrons in transition metal elements populate the d orbitals then their contribution to the magnetic Compton profile is the most significant. The negative polarisation associated with the s/p hybrid magnetic momentum distribution around the origin arises because the d band "pushes" the s and p electron energy states outside the occupied region (see Wakoh and Yamashita, 1966). As a result their contribution to the total polarisation is determined by the number of electrons above the Fermi energy in the minority, or least occupied, band (i.e. spin up) rather than their population below E_f as is the case for the d band electrons. In real space this negative polarisation is manifest as a negative magnetisation density in the interstitial regions.

In general the contribution of orbital electron motion to the net magnetisation of a ferromagnet is described by the spectroscopic splitting factor, g ($\sim$ 2.0023 for a free electron). For the 3d transition metal elements, however, g lies close to the free electron value (i.e. g $\sim$ 2.1 for iron and $\sim$ 2.2 for nickel) whence the core contribution to $J_{mag}(q)$ is "quenched" (see Blakemore, 1974). Evidence that the effect of orbital electronic motion is more significant in nickel (i.e. where quenching is reduced) than it is in iron is given by the larger area of the core contribution to the magnetic Compton profile in figure 7.1(b) (dotted line). In this case the dip at the origin is less characteristic of the negative spin polarisation contribution to the total magnetisation. The extent of $J_{mag}(q)$ for a given ferromagnet is determined largely by the strength of the exchange field between the neighbouring unpaired d electrons.

The contribution of the spin polarised electrons to the total Compton profile is $\sim$ 8% for iron and $\sim$ 2% for nickel. The magnetic Compton profile, therefore, accounts for

significantly more momentum density than do anisotropic effects in non-magnetic studies (typically ~ 1 %J(0) in magnitude) and should be easier to detect. Up until the present time practical spin dependent studies have been limited in the absence of a suitable high intensity radiation source. The advent of the Daresbury synchrotron radiation source (SRS), however, now facilitates magnetic Compton profile measurements for the first time using circularly polarised radiation.

7.2. Circularly Polarised Synchrotron Radiation.

Synchrotron radiation is produced by accelerating electrons (and positrons) in a circular orbit defined by a series of dipole bending magnets located suitably around a current storage ring (see Koch, 1983, for a complete technical review). To obtain high photon energies the motion of the electrons must be relativistic (i.e. with energies of ~ 2 GeV) in which case the angular distribution of the emitted intensity is distorted into a narrow cone in the direction tangential to the electron orbital plane. Consequently the emitted spectrum is strongly Doppler shifted and extends typically from the microwave region ($\lambda \sim 10^{-6}$ m) to the hard X-ray region ($\lambda \sim 10^{-10}$ m) depending on the machine dimensions and the harmonics of the electron revolution frequency.

The radiation emitted by an electron in the plane of its orbit is 100 % linearly polarised with the electric vector, $E_{||}$, parallel to the orbital plane. Above and below this plane, however, there exists a component of the polarisation with the E vector perpendicular to the photon wavevector. In general $E_{\perp}$ is out of phase with that parallel to the orbital plane. When viewed away from the orbital axis, therefore, synchrotron radiation is characterised by both components of the polarisation. Complete circular polarisation is only observed between two interfering photons if their electric vectors are of equal magnitude (i.e. $|E_{||}| = |E_{\perp}|$)and they are in quadrature (90° out of phase). In general, therefore, synchrotron radiation is elliptically polarised with the degree of circular polarisation dependent on the azimuthal angle, ψ, and the wavelength of the emitted photon, λ, i.e. ;

$$P_c = \frac{2(I_{\perp}I_{||})^{\frac{1}{2}}}{I_{||} + I_{\perp}} \qquad (7.4)$$

where $I_{\parallel}$ and $I_{\perp}$ are the respective intensities parallel and perpendicular to the orbital plane (for the explicit dependence of P_n on ψ and λ see eq. 7 of Koch). Consequently as the scattering angle is varied the degree of linear polarisation reduces from 100 % (for $\psi = 0$) to 0 when the conditions for complete circular polarisation are met (determined primarily by the electron energy). The hand of the elliptic polarisation depends on the direction of curvature of the electron beam, which is defined by the dipole bending magnets, and on the position of the observer with respect to the orbital plane.

In addition to the radiation produced by electrons with circular trajectories in bending magnets, it is possible to enhance the brightness of the emitted intensity at higher photon energies by incorporating other magnetic structures in the synchrotron design. The most common of these devices is the so called wiggler magnet which may be inserted into a straight section of the storage ring. Essentially a wiggler forces the electron beam to execute a trajectory with a smaller local radius of curvature than in the dipole bending magnets by using a larger local magnetic field. The 3 pole superconducting wiggler magnet incorporated in the Daresbury SRS, where the present study was conducted, is illustrated schematically in figure 7.2(a). The subsequent horizontal "wiggle" in the electron trajectory is achieved by poling the central magnet in the opposite direction to those up and downstream of the circulating electron beam. Since the individual poles are all of the same length but with the outer pair having half the number of turns of the centre magnet, the total field applied to the electrons is zero whence no net deflection of the beam is observed. The total intensity emitted tangentially to the direction of motion comes from two sources. The centre dipole produces radiation of higher intensity due to its larger field (5T) compared with the end poles whose contribution is substantially reduced - see Holland (1986) for the relative intensity distribution.

The spectra of synchrotron radiation generated by a 2 GeV electron beam passing through (i) a dipole bending magnet (B=1.2 T) and (ii) the wiggler installed at the Daresbury SRS are shown in figure 7.2(b). The critical wavelengths of these spectra (i.e. those corresponding to a maximum in the distribution) are 3.88 Å (3.2 keV) and 0.93 Å (13.3

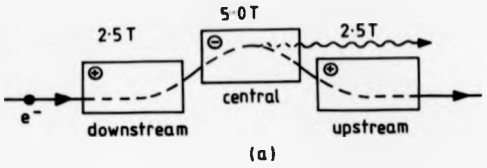

(a)

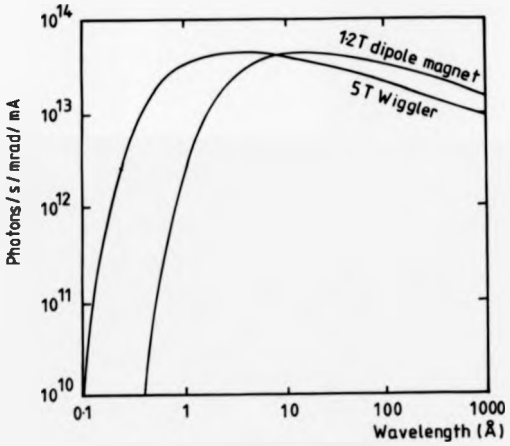

(b)

Figure 7.2 (a) Schematic illustration of the 3 pole, 5 T (λ_c — 0.93 Å) wiggler magnet as viewed from above installed in the SRS at Daresbury and (b) the intensity per mrad per second produced by this magnet compared with that obtained from a 1.2 T (λ_c = 3.88 Å) dipole bending magnet (see Holland, 1986).

keV) respectively whence the effect of the wiggler is to shift the entire emitted spectrum by ~ 3 Å. This represents a substantial gain in brightness in the hard X-ray region ($\lambda < 1$ Å).

Figure 7.3(a) shows I_+ and I_- at emitted photon wavelengths between 0.1 Å and 0.5 Å for the Daresbury wiggler magnet (see Holt and Cooper, 1983). The variation in the degree of circular polarisation, P_c, and linear polarisation, P_l, with azimuthal angle corresponding to these curves at 0.1 Å (solid lines) and 0.2 Å (dashed lines) is shown in figure 7.3(b). The cut off in the 0.1 Å curve in the latter represents the limit of useful intensity. From these figures it is clear that an appreciable degree of circular polarisation (e.g. $P_c > 0.6$) can only be obtained at the expense of a dramatic decrease in the intensity of the beam as the angle of view moves out of the orbital plane. Subsequent experiments, therefore, are performed optimally as far off the beam axis as possible without too great a loss in measured intensity.

7.3. Previous Research

The first measurement of the magnetic Compton profile of iron was made one decade ago using nuclear orientation in cooled ^{57}Co to achieve an appreciable degree of circular polarisation (see Sakai and Ono, 1977). The circularly polarised intensity of the 122 keV radiation emitted by this source, however, is only 10 mCi due to the upper intensity limit imposed by self-heating effects in the isotope material which effectively prevented cooling below ~ 50 mK. In this experiment only ~ 4×10^4 counts were accumulated in the difference profile in a measurement time of ~ 140 hours from a 1 cm thick iron sample and a scattering angle of 138°. A dip at the origin of approximately three times that predicted by the APW calculation in figure 7.1(a) (i.e. ~ 50 % of the magnetic profile peak height - see Wakoh and Kubo, 1977) was apparent in the data although the statistical accuracy of the difference spectrum was not sufficient to establish its significance.

A more recent experiment by a method similar to that described above has been performed by Sakai, Terashima and Sekizawa (1984) in which nuclear orientation in the iso-

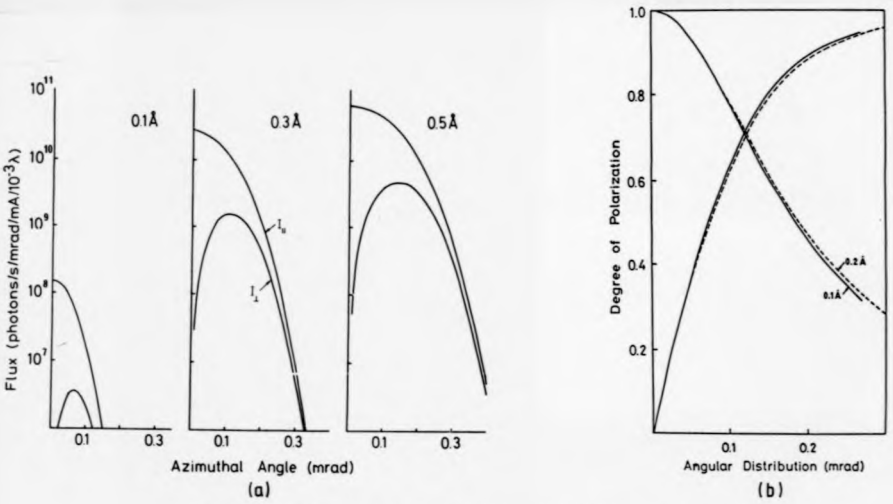

Figure 7.3 (a) The intensities of the beam polarised parallel ($I_{\parallel}$) and perpendicular ($I_{\perp}$) to the orbital plane as a function of the azimuthal angle at wavelengths between 0.1 Å and 0.5 Å for the Daresbury SRS wiggler magnet. (b) The corresponding variation in the degree of circularly polarised radiation, P_c, with azimuthal angle for 0.1 Å and 0.2 Å incident wavelengths (see Holt and Cooper, 1983).

tope ^{191}Ir provided the circularly polarised radiation (129 keV). Since the ^{191}Ir nuclei can be aligned sufficiently at 100 mK to produce a higher degree of circular polarisation than the ^{57}Co isotope employed in the initial experiment ($P_c \sim 0.8$ compared with ~ 0.3), then the source self-heating is far less severe. As a result an emitted intensity of 40 mCi was achieved in this second study. For a scattering angle of $\sim 145^\circ$ and a 1 cm thick iron sample, an exposure time of 165 hours produced $\sim 6.4 \times 10^8$ counts in the magnetic Compton profile which represents an improvement by an order of magnitude in the statistical accuracy obtained in the cobalt experiment. Corrections for the low energy resolution function tail (see section 3.3.2.2), detector efficiency and sample absorption were made to the difference data in both studies although no account of multiple scattering was taken in either. The resolution FWHM at the Compton peak due to detector and geometrical effects in the later experiment was 1.05 a.u. Again evidence of a dip at the origin of momentum space was apparent in the experimental magnetic Compton profile which was in good agreement with the APW result within statistical error.

The nature of the APW band calculation of Wakoh and Kubo (1977) is very similar to that employed for chromium (outlined in section 5.2.2) with the exception that a spin dependent X_α potential was used (i.e. the effects of exchange on the spin distribution were described). The [111], [110] and [100] magnetic Compton profiles of iron were obtained for the band electrons by summing over the momentum space wavefunctions evaluated at 55 k-points in 1/48th of the Brillouin zone for each spin state. The individual band profiles were preserved for ease of interpretation and were compared with a spherical average of $J_\uparrow(p_z) - J_\downarrow(p_z)$ as illustrated in figure 7.1(a). This calculation was performed for a net magnetisation of 2.2 Bohr magnetons per atom.

The band calculation of Rennert et al (1983) employed Bloch functions constructed from atomic d orbitals (LCAO) and four orthogonal plane waves (OPW's) to deduce the magnetic Compton profile of nickel. The directional spin distributions were evaluated out to 70 reciprocal lattice vectors (compared with 249 used in the APW calculation) and then spherically averaged. The resultant spin-dependent Compton profile is illustrated in figure

7.1(b) and corresponds to a total magnetisation of 0.56 Bohr magnetons per atom.

The availability of circularly polarised radiation to probe the unpaired spin distribution in ferromagnets potentially offers a more practical method of measuring their magnetic Compton profile than that of nuclear orientation. In general synchrotron radiation facilitates higher beam intensities and hence considerably shorter exposure times than the rival technique (i.e. several hours compared with several hundred hours). Furthermore subsequent experiments may be performed at room temperature rather than depend on a critically cooled sub-kelvin source environment.

7.4. Experimental Method

The experimental measurements were carried out using the powder diffraction port on the wiggler beam line (W9) of the Daresbury SRS. The layout of the machine between dipole magnets 8 and 9, where the wiggler is positioned, is illustrated schematically in figure 7.4 (taken from Greaves, Bennett, Duke, Holt and Suller, 1983). The aperture of beam line W9 is 64 mrad (3.7°) and transmits ~ 70 % of the total power emitted in straight 9 (i.e. out of a total fan of 102 mrad). The powder diffraction station is positioned approximately 16 m away from the wiggler tangent points and receives a maximum flux of 220 mW $mrad^{-1}$ mA^{-1} corresponding to an electron energy of 2 GeV (compared with 41 mW $mrad^{-1}$ mA^{-1} emitted from a standard 1.2 T dipole bending magnet).

The experimental arrangement adopted is shown schematically in figure 7.5. The incident beam was collimated by a set of main slits which enabled a portion of the intensity ~ 1.5 mm (0.09 mrad) above the orbital plane to be selected by fine adjustment of the secondary slits. The remaining flux was monochromated by a vertically dispersing Si-220 double crystal arrangement to produce 33.7 keV radiation. The function of the slits in front of the sample was to absorb any unwanted "scattered" intensity. A shielded germanium solid state detector, similar to that employed in conventional Compton scattering experiments, was used to record the intensity of the beam scattered through an angle of 150 ± 2°. Such a back scattering geometry corresponds to an energy transfer of ~ 3.4 keV

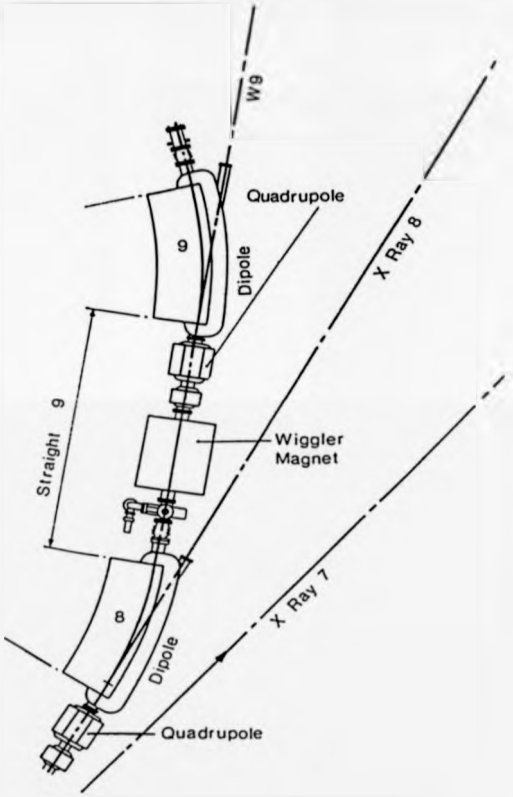

Figure 7.4 The layout of the Daresbury SRS straight 9 including the dipole magnets adjacent to the superconducting wiggler magnet.

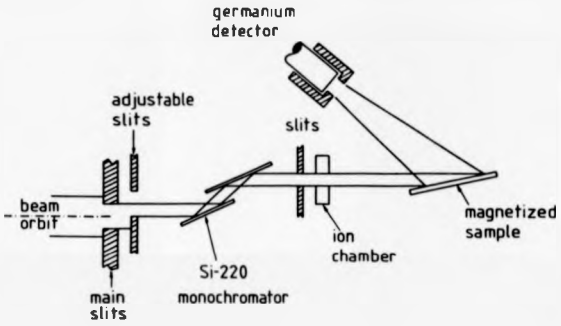

Figure 7.5 (a) A schematic representation of the experimental arrangement on the powder diffraction port of the wiggler beam line for measuring the magnetic Compton profile of iron.

whence the Compton peak can be clearly separated from the elastic line.

The magnetic field in the 40 mm × 100 mm × 5 mm iron sample was provided by a soft iron electromagnet and was reversed at 10 and 20 s intervals in an asynchronous cycle with a period of 80 s, controlled by a BBC microcomputer. The magnetisation direction within the sample was aligned as nearly parallel to the scattering vector as possible to maximise the scattered intensity (i.e. the scalar product in eq. 7.3 assumes its maximum value). For each field direction the scattered energy spectrum was recorded in separate halves of an Ortec multichannel analyser memory. A total of 1.4×10^6 counts were accumulated under the Compton line in 3.5 hours with the SRS operating at 2 GeV with an initial current of 150 mA. The beam lifetime was approximately 5 hours and the intensity throughout the experiment was continuously monitored by an ion chamber positioned immediately before the sample.

This experiment was hampered severely throughout by the confined space available in the powder diffraction work station. This made optimisation of the experimental arrangement at the beginning of each beam cycle extremely arduous and time consuming. As a result ~ 30 % of the available intensity was lost (the beam is at its most intense at the beginning of its life) which effectively limited the level of statistical accuracy that could be attained. In addition the optimisation procedure was further constrained by heating effects in the main slits. This caused the adjusting mechanism to jam and consequently reduced the extent to which the experimental conditions could be varied. In total three attempts to measure the magnetic Compton profile of iron were made for different electron beams. The recurrent failure of the synchrotron to confine the circulating electron beam to a well-defined orbit, however, prevented more than one dataset of sufficient statistical accuracy being recorded.

7.4.1. Sample Magnetisation

The field required to completely align the individual spins in a pure ferromagnetic crystal is given by the direction dependent saturation magnetic field, M_s. Table 7.1 gives

the value of M_s per cm^3 along with other spin-dependent constants for three common ferromagnets.

Ferromagnet	M_s T cm^{-3}	Bohr Magnetons (atom^{-1})	g	Curie Point (°C)
Iron	0.1714	2.219	2.10	770
Cobalt	0.1422	1.715	2.18	1115
Nickel	0.0481	0.604	2.21	354

Table 7.1 Spin-dependent constants of three common ferromagnets.

Although iron is the most difficult of these elements to completely magnetise it possesses the largest magnetic moment per atom. This indicates that the spin contribution to the total profile measured in a magnetic Compton scattering experiment is potentially the most significant for this ferromagnet whence $J_{mag}(p_z)$ can be more readily observed.

Since the iron sample prepared for this study was polycrystalline, the required saturation field was considerably higher than that given in table 7.1. This difference is a result of the difficulty in orienting individual grains, some of which may be aligned parallel to the direction least preferred spin orientation (i.e. [110] for iron) in the unmagnetised state. Practically, therefore, complete spin alignment is rarely achieved for polycrystalline ferromagnets.

For a moderate current of 0.5 A, the number of turns around the core of the horseshoe magnet used to magnetise the iron sample was calculated to be ~ 130. Since the actual number of turns used was in excess of 800, then a state close to saturation was ensured. In addition, to minimise the effects of flux leakage between the polepieces and the

sample, the areas of contact were ground and polished flat.

In its working state with a current of 0.5 A the field at the surface of the sample was measured to be ~ 0.4 T which is more than double that required to completely saturate crystalline iron. Since the value of M_s for iron is relatively high, this field is also sufficient to align the majority of the unpaired spins present in both nickel and cobalt, the former ferromagnet being the second subject of this study.

7.5. Results and Discussion

7.5.1. Iron

A typical spectrum recorded from one spin orientation in the magnetised iron sample is shown in figure 7.6(a). It can be seen that the elastically scattered line (33.7 keV) is clearly separated from the Compton line (30 keV) and is considerably narrower (FWHM ~ 600 eV). Figures 7.6(b) and (c) show the intensity difference between the two spin direction measurements for ψ = 0 and 0.09 mrad (i.e. P_e ~ 0.56) over the region of the Compton peak. At the powder diffraction station these values of azimuthal angle correspond to relative displacements of 0 and 1.5 mm above the orbital plane respectively. Since the coupling between circularly polarised radiation and unpaired electrons necessarily involves a transfer of energy from probe to target (see eq. 7.3) the elastically scattered intensity is independent of magnetic effects. Hence the disappearance of the elastic peak (and of the iron K_α and K_β fluorescent lines, not shown) indicates that systematic errors are absent from the difference spectra. In addition the relatively short counting time for each field direction (i.e. 20 s maximum) ensures that both datasets are largely unaffected by either the decay of the source or instabilities in the electron beam.

In the plane of the electron orbit the incident photons are completely linearly polarised (i.e. P_e = 0) and as a result figure 7.6(b) shows only a random scatter of points about the energy axis (i.e. ΔJ conforms to a normal distribution of mean zero). For the off-axis measurement, however, there is a residual positive peak in the difference spectrum around the position of the Compton peak energy. Compared to the total Compton scattered

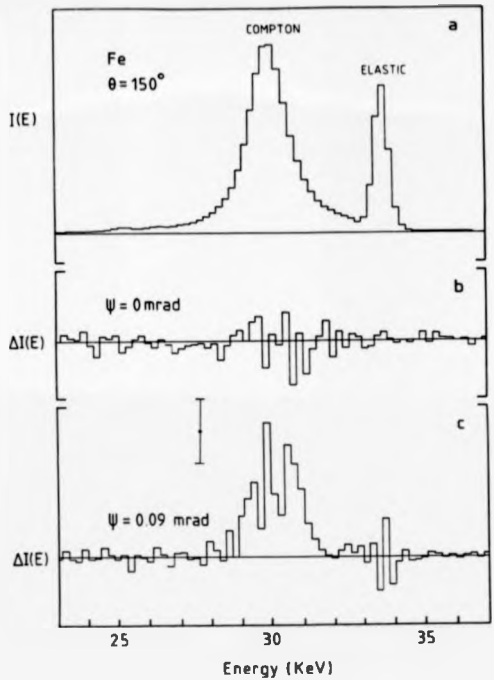

Figure 7.6 (a) the spectrum from magnetised iron for one spin orientation indicating the position of the elastic (33.7 keV) and Compton (30.0 keV) lines. The intensity difference between spin directions for measurements made in the orbital plane (ψ = 0 mrad) and 1.5 mm above the orbital plane (ψ = 0.09 mrad) are shown in parts (b) and (c) respectively. All data have been averaged in blocks of 10 channels and the intensity scale is in arbitrary units.

intensity, this difference represents a 1 % effect which is in good agreement with that expected from cross-section considerations for this incident energy (see Holt and Cooper, 1983). It has been shown that the hand of elliptical polarisation reverses as the orbital plane is crossed (see Lipps and Tolhoek, 1954). For measurements below the orbital plane, therefore, the sign of the spin-dependent difference would change according to eq. 7.3 and a peak of net negative area would be observed.

In order to improve their statistical accuracy, which is limited by the difficulties encountered in optimising the experimental conditions, the data plotted in figure 7.6 have been averaged in blocks of 10 channels (ΔE = 200 eV). The anticipated volcano structure of the magnetic profile is actually visible in the raw data when presented in this manner.

Figure 7.7 shows a left/right average of the difference data after the transformation to an electron momentum scale. Here the isotropic spin-dependent Compton profile is plotted after the correction for the energy variation of the cross-section (eq. 7.3) has been applied. The corrections for photoelectric absorption and multiple scattering, however, were not made to the experimental data in view of the poor statistical accuracy of the results.

Also included in figure 7.7 is the APW calculation of Wakoh and Kubo (1977) (indicated by the broken line) which has been convoluted with a Gaussian of FWHM 0.9 a.u. This represents the overall momentum resolution due to detector and geometrical broadening effects (see eq. 3.8). After normalisation of the experimental data to 1.05 electrons between 0 and 5.0 a.u., corresponding to the area of the theoretical magnetic profile, there is reasonable quantitative agreement between the measured spin density distribution and that calculated by the APW method. Although the dip at the origin predicted by the calculation is observed experimentally, a detailed assessment of its magnitude cannot be made due to the experimental error over the region of the difference profile [i.e. $\sim$ 35 % $J_{mag}(0)$]. The fact that the lineshape has the correct half-width coupled with its complete disappearance in the orbital plane, however, indicates that the data shown in figure 7.7 corresponds to the first successful measurement of the spin dependent Compton profile of

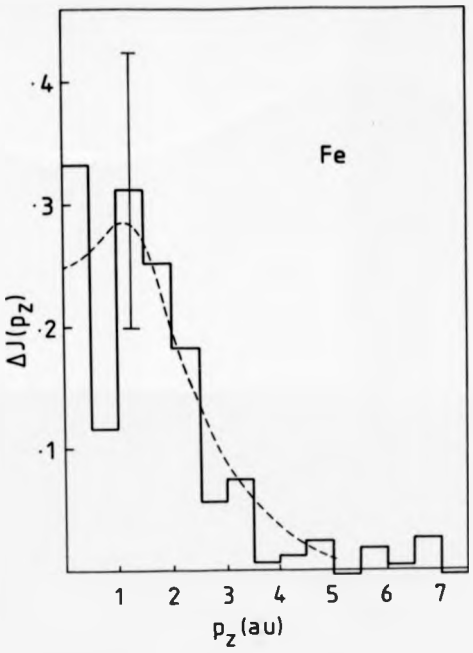

Figure 7.7 Comparison of the spin dependent Compton profile of iron obtained experimentally with the results of an APW calculation (broken line -see Wakoh and Kubo, 1977). The band calculation has been convoluted with a Gaussian of FWHM 0.9 a.u. corresponding to the experimental resolution half-width. The measured data has been averaged over both sides of the profile and normalised to 1.1 electrons between 0 and 5 a.u.

iron with circularly polarised synchrotron radiation.

7.5.1.1. Significance of Results

The magnetic Compton profile of iron measured by Sakai et al (1984) is of substantially better statistical accuracy than $J_{mag}(q)$ presented here (i.e ~ 12 % c.f. ~ 35 % at the difference peak). This is because the variation in the ratio of the magnetic to the ordinary Compton cross-section is ~ $\frac{\omega_1}{m_0c^2}$ in which case the 129 keV incident photon energy employed in the nuclear orientation experiment yields the higher statistics from a lower total number of counts in each Compton profile. In addition the current experimental arrangement is not optimum as reflected by the low count rate attained in the magnetic Compton profile which is an order a magnitude less than that predicted in a feasibility study (see Holt and Cooper, 1983).

It has recently been suggested by Kim (1984) that cancellation effects away from the beam axis significantly reduce the degree of circular polarisation that may be obtained if the point of observation affords a view of both the central and up/downstream wiggler magnets. This is not the case, however, since the intensity distribution emanating from the centre tangent point of the wiggler is displaced in energy relative to that produced up and down stream of the circulating electron beam - i.e. where the magnetic field strength is one half that at the centre [see figure 7.3(b)]. For the Daresbury wiggler magnet, therefore, cancellation effects are confined to emitted photon energies of less than ~ 20 keV and do not influence the polarisation of the radiation utilised in this experiment.

7.5.2. Nickel

This second study was performed on the topography port on the wiggler beam line adjacent to that used for powder diffraction. The work station on this port is considerably more spacious than that used for the iron measurement which reduces the problems associated with optimising the experimental arrangement. Additionally the mechanical slit adjustments are computer controlled whence the effects of collimation etc. on the recorded

intensity could be readily assessed.

The experimental arrangement employed to measure the magnetic Compton profile of nickel was very similar to that described in section 7.4 except that a germanium 333 single crystal was used to monochromate the incident beam (see Cooper, Laundy, Cardwell, Timms, Holt and Clark, 1986). The 46.4 keV incident radiation was then scattered through an angle of 151 ± 2° which subsequently produced a Compton peak at 39.8 keV.

The actual nickel sample consisted of a composition of 2 cm wide by 10 cm long layers of high purity nickel foil pressed together to form a single sheet of thickness ~ 0.4 cm. The ends of the sheet were held firmly in contact by soft iron clamps of the same contact dimensions as the magnet polepieces to minimise the effects of flux leakage. To enhance its magnetic properties, the nickel foil was annealed before the sample was constructed. This effectively produces a larger average grain size than present in the unannealed polycrystal resulting in a lower saturisation magnetisation. Since crystalline nickel is easier to saturate than iron (M_s ~ 0.5 compared with 0.17 - see table 7.1), a greater fraction of the unpaired spins are aligned by the horseshoe magnet in this study than in the first measurement. The effective number of Bohr magnetons per atom, however, is less than that for iron and consequently the magnetic contribution to the total Compton cross-section for nickel is lower by ~ 75 %.

Since the topography port is some 35 m distant from the beam orbit this measurement was made at ~ 8 mm above beam axis corresponding to an asimuthal angle of 0.24 mrad (i.e. $P_c > 0.08$). The resolution of this experiment was 0.8 a.u.

The number of counts accumulated in each spin-dependent Compton profile after an exposure time of 1 hour was ~ 2×10^4 which is considerably less than that obtained for iron. Subsequently only ~ 200 counts were recorded in the difference profile for this measurement (compared with ~ 1000 for the iron measurement) which corresponds to an error of ~ 40 % at the Compton peak energy. Even so a net positive area was detected with

the elastic line again cancelling to indicate that the data was free from systematic errors. The difference was then corrected for the energy variation of both the Compton cross-section and the sample absorption before transformation to a momentum scale via eq. 7.3. The resultant magnetic Compton profile is shown in figure 7.8. This data has been averaged in momentum blocks of width 1.5 a.u. to improve its statistical accuracy and normalised to 0.606 - i.e. the number of unpaired spins per atom present in nickel. Additionally a left/right average has been taken. This distribution represents the first observation of the magnetic Compton profile of nickel by any experimental technique.

The spin-dependent profile derived from the OPW calculation of Rennert et al (1983) is indicated by the dashed line in figure 7.8 and has been convoluted with a Gaussian of FWHM 0.8 a.u. corresponding to the width of the experimental resolution function. Again the dip in $J_{mag}(q)$ at the origin due to the negative s/p hybrid polarisation is evident in the experimental data although the statistical error of the measurement prevents quantitative assessment of the lineshape. The experimental result, however, is in good agreement with theory at all points in the distribution to within 2σ of the statistical error.

7.5.3. Comparison of the Iron and Nickel Measurements.

Apart from the magnitude of the respective distributions, perhaps the most significant difference difference between the theoretical magnetic Compton profiles of iron and nickel is that the latter extends to higher momentum ($\sim$ 7 a.u. compared with $\sim$ 5 a.u.). This prediction is confirmed by experiment in both studies as can be seen from figures 7.7 and 7.8, respectively. Although both measurements are subject to a high statistical error they are entirely consistent with the results of the available theory and encourage further research.

Since the nickel data was accumulated for a relatively short period of time (compared with the iron measurement), the significance of the result suggests that this measurement was performed much closer to optimum experimental conditions. Additionally if the difference in the number of Bohr magnetons per atom between the two ferromagnets

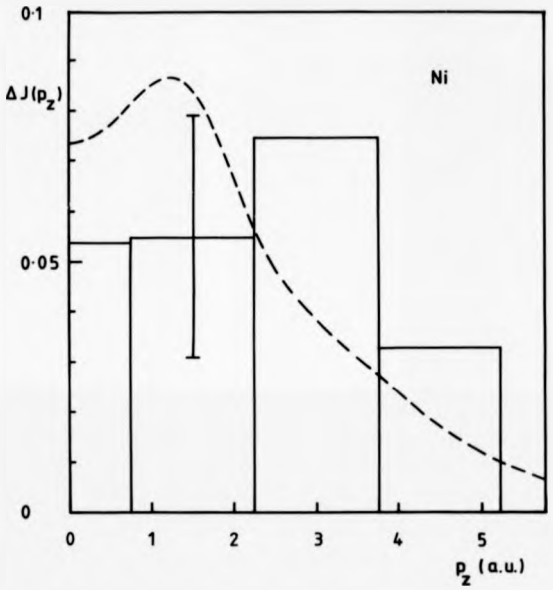

Figure 7.8 Comparison of the experimental spin dependent Compton profile of nickel with the results of an OPW calculation (broken line - see Rennert et al, 1983). The measured data has been normalised to 0.3 between 0 and 6 a.u. and averaged over both sides of the profile in 1.5 a.u. blocks of momentum to improve its statistical accuracy. The theory has been convoluted with a Gaussian of FWHM 0.8 a.u. corresponding to the half-width of the experimental resolution function.

is taken into account, the net gain in measured intensity compared to that obtained in the iron study is up by about an order of magnitude. Repetition of the iron measurement, therefore, on the topography port should enhance the statistical accuracy of the magnetic Compton profile by at least a factor of 3 in which case the experiment could establish any discrepancies between $J_{mag}(q)$ observed and that derived from the APW band calculation. A further measurement of the magnetic Compton profile of nickel with a longer exposure time would also facilitate a more meaningful interpretation of the shape of $J_{mag}(q)$ than that possible here.

7.6. Conclusions

In conclusion it can be stated that the detection of the magnetic Compton profiles of iron and nickel is by far the most exciting development in contemporary momentum density studies.

The degree of difficulty in measuring $J_{mag}(q)$ is gradually being reduced. Indeed, these results suggest that subsequent measurements on the topography port will not be limited by low count-rates (a positive result was obtained in the nickel study for a very short exposure time). With multiple scattering and geometrical broadening corrections, in particular, included in the processing of the magnetic difference data, therefore, this technique provides potentially detailed information about the spin density distribution complementary to that extracted from neutron scattering experiments (see Marshall and Lovesey, 1971).

Blume (1985) has pointed to the great wealth of information about magnetic systems embedded in the X-ray scattering cross-section. The results of this study demonstrate conclusively that magnetic effects can be observed experimentally by utilising a characteristic of synchrotron radiation hitherto unexploited in momentum density studies. The technique described here has proved by far the most practical method of measuring the magnetic Compton profile and its success represents a significant step forward in Compton spectroscopy.

SUMMARY

Over recent years Compton spectroscopy has advanced significantly with a better understanding of geometrical broadening, multiple scattering and source broadening. Accompanying this progression has been the ability to deduce Compton profiles of high statistical accuracy [$\sigma < 0.5$ %J(0)] which exhibit a high degree of symmetry as illustrated in the present work. This enables more information to be extracted from the measured data and facilitates resolution between small differences in directional measurements such as those present in good free electron metals. In addition, the limitations of low energy spectrometers have been established and are now used solely for the deduction of anisotropic data. This complements the more reliable, but usually less accurate, high energy measurements.

Apart from density functional theory, the application of band calculations to momentum density studies has seen very little activity over the past decade due primarily to the inability of experiment to resolve the small differences between the results of the various band methods. It is now possible, however, to analyse the quantitative deficiencies of band calculations, such as the occupation of high momentum states, rather than merely identifying trends in theory - experiment difference data. In particular the present study has highlighted the APW method to be a versatile theoretical tool in calculating the Compton profiles of simple, transition and ferromagnetic elements. Associated with the resurrection of density functional theory has been the problem of determining momentum densities from the solutions of the Kohn-Sham equations (i.e. within the local approximation). This appears to have been overcome with the advent and application of the Lam-Platzman correction which substantially improves the agreement between experiment and theory as illustrated in chapter 6. Consequently the convergence of theoretical densities to those observed experimentally, particularly for transition metal elements, has been accentuated over the past two years.

In previous studies theoretical Compton profiles have been found to overestimate significantly and consistently the peak height of their experimental counterparts. In this study the magnitude of this discrepancy has been reduced considerably - typically to within 2σ for the APW band theory. Again this reflects an improvement in the data reduction procedure and the ability to correct theoretical data for the effects of exchange and correlation.

The most significant and exciting advance in Compton spectroscopy during this work has been the detection of the magnetic Compton profiles of iron and nickel using synchrotron radiation. These measurements represent the first observation of spin-dependent effects by this technique and point to the beginning of a new generation of Compton scattering studies.

Future Developments

Common spectrometer systems used for Compton scattering measurements are, in general, restricted to a unique scattering geometry. Two systems under current development, however, incorporating ^{137}Cs and ^{51}Cr γ-ray sources and located at the University of Warwick and the Hahn-Meitner Institute, Berlin respectively, have been designed with a variable scattering geometry. These facilitate determination of the Compton cross-section for a range of scattering angles which will ultimately establish the validity of the data processing appropriate to each system. In addition to varying the scattering geometry, it is also desirable to incorporate a range of high energy sources in the spectrometer design. Although no such systems are at present planned, this modification would allow empirical assessment of current data processing simulations such as the multiple scattering and source broadening corrections.

With the completion of the transition metal measurements, the progression from elemental to metallic compound studies is imminent. Such an investigation concerned with the momentum distribution in an iron-nickel alloy is already underway at the University of Warwick. Compton scattering studies of other physically interesting systems, such as

phase transitions, have yet to be performed with a high degree of reliability which, as illustrated by this study, is now possible.

The greatest potential of experimental Compton scattering undoubtedly lies in the study of spin-dependent effects in ferromagnets. In succession to the results presented here another measurement of the magnetic Compton profile of iron has been performed on the topography port. This study observed an increase by an order of magnitude in the number of counts under the difference profile (see Cooper, Laundy, Cardwell, Timms, Holt and Clark, 1986). This enables a quantitative study of the lineshape to be made and hence forms the basis of a more meaningful comparison with theory than that presented in chapter 7. With continued optimisation of the available synchrotron intensity and experimental arrangement another increase by an order of magnitude in the accuracy of the measured profile is anticipated. This would facilitate the study of other ferromagnets with relatively few unpaired spins such as cobalt and gadolinium in addition to a repetition of the nickel investigation presented in section 7.5.2 but for a longer exposure time. The information potentially available from profile measurements above and below the ferromagnetic transition temperature is profound. Consequently the results of the next generation of Compton scattering experiments will provide a stringent test of the predictions of future band calculations.

REFERENCES

Barlan, A. D., Rueckner, W. and Wellenstein, H. F., 1977, Phil. Mag. **36**, 201.

Bauer, G. E. W. and Schneider, J. R., 1983, (a) Solid State Comm. B **47**, 673 (b) Z. Physik. B **54**, 17.

Bauer, G. E. W. and Schneider, J. R., 1984, Phys. Rev. Letts. **52**, 2061.

Benesch, R. and Smith, V. H. jr., 1973, Density Matrix Methods in X-Ray Scattering and Momentum Space Calculations in Wave Mechanics, the First Fifty Years, Editors Price, W. C., Chissick, S. S. and Ravenadale, T., Butterworths publ., London.

Biggs, F., Mandelsohn, L. B. and Mann, J. B., 1975, Atomic Data and Nuclear Data Tables **16**, 201.

Blakemore, J. S., 1974, Solid State Physics, Saunders publ., Philadelphia.

Bloch, F., 1928, Z. Physik. **52**, 555.

Bloch, B. J. and Mendelsohn, L. B., 1974, Phys. Rev. A **9**, 129.

Blume, M., 1985, J. Appl. Phys. **57**, 3615.

Cardwell, D. A. and Cooper, M. J., 1986, Phil. Mag. B **54**, 37.

Causa, M., Dovesi, R., Pisani, C. and Roetti, C., 1981, Phil. Mag. B **44**, 419.

Clementi, E., 1965, IBM J. Research and Development, Suppl. **9**, 2.

Compton, A. H., 1923, Phys. Rev. **21**, 201.

Cooper, M. J., 1985, Rep. Prog. Phys. **48**, 415.

Cooper, M. J., Holt, R. S. and DuBard, J. L., 1978, J. Phys. E: Sci. Instrum. **11**, 1145.

Cooper, M. J., Laundy, D., Cardwell, D. A., Timms, D., Holt, R. S. and Clark, G., 1988,

Phys. Rev. B **34**, 5984.

Cooper, M. J., Pattison, P. and Schneider, J. R., 1976, Phil. Mag. **34**, 243.

Cooper, M. J., Pattison, P., Williams, B. and Pandey, K. C., 1974, Phil. Mag. **29**, 1237.

Cooper, M. J., Rollason, A. J. and Tuxworth, R. W., 1982, J. Phys. E: Sci. Instrum. **15**, 568.

Cooper, M. J., Williams, B. G., Borland, R. E. and Cooper, J. R. A., 1970, Phil. Mag. **22**, 441.

Coulson, C. A., 1961, Valence, 2nd edition, O.U.P. publ., Oxford.

Cracknell, A. P. and Wong, K. C., 1973, The Fermi Surface, publ. Oxford University Press.

Curratt, R., DeCicco, P. D. and Kaplow, R., 1971, Phys. Rev. B **3**, 243.

Curratt, R., DeCicco, P. D. and Weiss, R J., 1971, Phys. Rev. B **4**, 4256.

Daniel, E. and Vosko, S. H., 1960, Phys. Rev. **20**, 2041.

Diana, M. and Mazzone, G., 1972, Phys. Rev. B **5**, 3832.

Eisenberger, P., Henneker, W. H. and Cade, P. E., 1972, Chem. Phys. **56**, 1207.

Eisenberger, P., Lam, L., Platzman, P. and Schmidt, P., 1972, Phys. Rev. B **6**, 3671.

Eisenberger, P. and Platzman, P. M., 1970, Phys. Rev. A **2**, 415.

Eisenberger, P. and Reed, W. A., 1972, Phys. Rev. A **5**, 2085.

Eisenberger, P. and Reed, W. A., 1974, Phys. Rev. A **9**, 3237.

Epstein, I. R., 1973, Phys. Rev. A **8**, 160.

Felsteiner, J., Pattison, P. and Cooper, M. J., 1974, Phil. Mag. **30**, 537.

Fock, V. Z., 1930, (a) Z. Physik. **61**, 126, (b) Z. Physik. **62**, 795.

Fock, V. Z., 1935, Z. Physik. **98**, 145.

Gasiorowicz, S., 1974, Quantum Physics. Wiley publ., New York.

Gottfried, K., 1966, Quantum Mechanics Vol. I: Fundamentals. Benjamin publ.

Greaves, G. N., Bennett, R., Duke, P. J., Holt, R. S. and Suller, V. P., 1983. Nucl. Inst. Meths. **208**. 139.

Gunnarson, O. and Lundqvist, B. I., 1976, Phys. Rev. B **13**, 4274.

Henderson, M. G. and Scherr, C. W., 1960, Phys. Rev. **120**, 150.

Hohenberg, P. and Kohn, W., 1964, Phys. Rev. **136**, B864.

Holland, D. M. P., 1986, Submitted to Phys. Scripta.

Holt, R. S., 1978, Ph.D. Thesis, University of Warwick, England.

Holt, R. S. and Cooper, M. J., 1980, Phil. Mag. B **41**, 117.

Holt, R. S. and Cooper, M. J., 1983, Nucl. Inst. Meths. **213**, 447.

Holt, R. S., DuBard, J. L., Cooper, M. J., Paakkari, T. and Manninen, S., 1979, Phil. Mag. B **39**, 541.

James, R. W., 1948, The Optical Properties of the Diffraction of X-Rays Vol. 2, Cornell University press.

Jauch, J. M. and Rohrlich, F., 1955, Theory of Photons and Electrons, Addison-Wesley publ., Cambridge, Massachusetts.

Kahn, A. H. and Frederikse, H. P. R., 1959, Sol. Stat. Phys. **9**, 257.

Kim, K.-J., 1984, Nucl. Inst. Meths. **222**, 11.

Kittel, C., 1976, Introduction to Solid State Physics, Wiley publ., New York.

Klein, O. and Nishina, Y., 1929, Z. Physik. **52**, 853.

Koch, E.-E., 1983, Editor, Handbook of Synchrotron Radiation Vol. 1a, North-Holland Publ. Co., Amsterdam.

Kohn, W. and Sham, L. J., 1965, Phys. Rev. A **140**, 1133.

Kramer, B., Krusius, P., Schröder, W. and Schlüke, W., 1977, Phys. Rev. Lett. **38**, 1227.

Krusius, P., 1977, J. Phys. C. **10**, 1875.

Kubo, Y., Wakoh, S. and Yamashita, J., 1976, J. Phys. Soc. Jap. 41, 830.

Lam. L. and Platzman, P., 1974, Phys. Rev. B 9, 5122.

Laurent, D. G., Wang, C. S. and Callaway, J., 1978, Phys. Rev. B 17, 455.

Lederer, C. M., Hollander, J. M. and Perlman, I., 1967, Table of Isotopes. 6th edition, Wiley publ., New York.

Lipps, F. W. and Tolhoek, H. A., 1954, Physica 20, 395.

Lock, D. G., Crisp, V. H. C. and West, R. N., 1973, J. Phys. F. 3, 561.

Lundqvist, B. I., 1967, Phys. Kondens. Materie. (a) 6, 193, (b) 6, 206.

Lundqvist, B. I., 1968, Phys. Kondens. Materie. 7, 117.

Lundqvist, S. and March, N. H. (Editors), 1983, Theory of the Inhomogeneous Electron Gas, Plenum Press, New York.

Mackintosh, A. R., 1963, Fermi Surfaces of Metals, Scientific American, July, 110.

Mader, J., Berko, S., Krakauer, H. and Bansil, A., 1976, Phys. Rev. Letts. 37, 1232.

Manninen, S., Paakkari, T. and Kajantie, K., 1974, Phil. Mag. 29,167.

Manninen, S., Cooper, M. J., Cardwell, D. A., 1986, Nucl. Instrum. Meths. A 245, 485.

Marshall, W. and Lovesey, S. W., 1971, Theory of Thermal Neutron Scattering, Oxford University Press.

Mendelsohn, L. B. and Biggs, E.A., 1973, U. S. Atomic Energy Conf. 720404 3, 1142.

Mendelsohn, L. B., Bloch, B. J. and Smith, V. H. jr., 1973, Phys. Rev. Lett. 31, 266.

Mendelsohn, L. B. and Bloch B. J., 1975, Phys. Rev. A 12, 551.

Moon, R. M., Koehler, W. C. and Trego, A. L., 1966, J. App. Phys. 37, 1036.

Moruzzi, V. L., Williams, A. R. and Janak, J. F., 1978, Calculated Electronic Properties of Metals, Pergamon publ., New York.

M'Weeny, R. and Coulson, C. A., 1949, Proc. Phys. Soc. A 62, 509.

Ohara, S., Fukamachi, T., Hosoya, S. and Takeda, T., 1974, J. Phys. Soc. Jap. 35, 337.

Ohba, S., Saito, Y. and Wakoh, S., 1982, Acta. Cryst. A **38**, 103.

Paakkari, T., Manninen, S. O. and Berggren K-F., 1975, Phys. Fennica **10**,207.

Pandey, K. C. and Lam, L., 1973, Phys. Lett. **43A**, 319.

Pattison, P. and Weyrich, W., 1979, J. Phys. Chem. Solids **40**, 213.

Pattison, P., Weyrich, W. and Williams, B. G., 1977, Sil. Stat. Com. **21**, 987.

Phillips, W. C. and Weiss, R. J., 1968, Phys. Rev. **120**, 790.

Pitkanen , T., Laundy, D., Holt, R. S. and Cooper, M. J., 1986, Nucl. Inst. Meths. A **451**, 536.

Platzman, P. M. and Tzoar, N., 1965, Phys. Rev. A **139**, 410.

Platzman, P. M. and Tzoar, N., 1970, Phys. Rev. B **2**, 3556.

Platzman, P. M. and Tzoar, N., 1985, J. Appl. Phys. **57**, 3623.

Podolsky, B. and Pauling, L., 1929, Phys. Rev. **34**, 109.

Rath, J., Wang, C. S., Tawil, R. A. and Callaway, J., 1973, Phys. Rev. B **8**, 5139.

Rennert, P., 1981, Phys. Stat. Sol. **105**, 587.

Rennert, P., Carl, G. and Hergert, W., 1983, Phys. Stat. Sol. **120**, 273.

Ribberfors, R., 1975, Phys. Rev. B **12** (a) 2067, (b) 3136.

Rollason, A. J., 1984, Ph.D. Thesis, University of Warwick, England.

Rollason, A. J., Holt, R. S. and Cooper, M. J., 1983, (a) J. Phys. F: Met. Phys. **13**, 1807 (b) Phil. Mag. B **47**, 51.

Rollason, A. J., Schneider, J., Laundy, D., Holt, R. S. and Cooper, M. J., submitted to J. Phys. F., 1987.

Sakai, N. and Ono, K., 1977, J. Phys. Soc. Jap. **42**, 770.

Sakai, N., Terashima, O. and Sekizawa, H., 1984, Nucl. Inst. Meths. **221**, 419.

Schlüter, M. and Sham, L. J., 1982, Physics Today, February.

Schülke, W., 1977, Phys. Stat. Solidi. (b) **82**, 229.

Schülke, W., 1978, Proc. Int. Conf. X-Ray and XUV Spectroscopy, Jap. J. Appl. Phys. **17**, 332.

Seitz, F., 1935, Phys. Rev. **47**, 400.

Shiotani, N., Okada, T., Sekizawa, H., Wakoh, S. and Kubo, Y., 1977, J. Phys. Soc. Jap. **43**, 1229.

Slater, J. C., 1930, Phys. Rev. **36**, 57.

Stassis, C., Kline, E. R. and Sinha, S. K., 1973, Phys. Rev. Lett. **31**, 1048.

Tanner, A. C. and Epstein, I. R., 1976, Phys. Rev. A **13**, 335.

Tawil, R. A., 1975, Phys. Rev. B **11**, 4841.

Wakoh, S. and Kubo, Y., 1977, J. Magn. Magn. Mater. **5**, 202.

Wakoh, S., Kubo, Y. and Yamashita, J., 1976, J. Phys. Soc. Jap. **40**, 1043.

Wakoh, S. and Yamashita, J., 1966, J. Phys. Soc. Jap. **21**, 1712.

Wakoh, S. and Yamashita, J., 1973, J. Phys. Soc. Jap. **35**, 1406.

Wang, C. S. and Callaway, J, 1975, Phys. Rev. B **11**, 2417.

Warren, B. E., 1969, X-Ray Diffraction, publ. Addison-Wesley, Wokingham, U.K.

Wachters, A. J. H., 1970, J. Chem. Phys. **52**, 1033.

Weiss, R. J., 1973, Phil. Mag. **27**, 1461.

Weiss, R. J., 1975, Phil. Mag. **32**, 247.

Weiss, R. J., Cooper, M. J. and Holt, R. S., 1977, Phil. Mag. **36**, 1, 193.

West, R. N., 1980, Int. Phys. Conf. Ser. **55**, 35.

Williams, B. G. (editor), 1977, Compton Scattering, McGraw Hill publ., U.K.

Ziman, J. M., 1964, Principles of the Theory of Solids, Cambridge University Press.

TITLE COMPTON SCATTERING WITH GAMMA-RAYS AND SYNCHROTRON RADIATION

AUTHOR David A. Cardwell

INSTITUTION and DATE University of Warwick 1987.